DISCLAIMER:

This document does not meet the
current format guidelines of
the Graduate School at
The University of Texas at Austin.

It has been published for
informational use only.

The Thesis Committee for Eric Cushman Bryant
Certifies that this is the approved version of the following thesis:

Hydraulic Fracture Modeling with Finite Volumes and Areas

APPROVED BY
SUPERVISING COMMITTEE:

Supervisor:

Mukul M. Sharma

John T. Foster

Hydraulic Fracture Modeling with Finite Volumes and Areas

by

Eric Cushman Bryant, B.A.; B.S.

Thesis

Presented to the Faculty of the Graduate School of

The University of Texas at Austin

in Partial Fulfillment

of the Requirements

for the Degree of

Master of Science in Engineering

The University of Texas at Austin

August 2016

Dedication

This work is dedicated to my dad George, who passed away last year.

Acknowledgements

The guidance and support of my supervisor Dr. Mukul M. Sharma is gratefully acknowledged. Parts of this work were accomplished in collaboration with co-workers. For example, the homogeneous residual stress formulation was developed by Dr. Jongsoo Hwang. Boundary (and internal continuity) conditions were developed under tutelage of Dr. Philip Cardiff, including work on finite areas. Dr. Krishnaswamy Ravi-Chandar provided me the context (in his fracture mechanics class) to describe residually stressed, poroelastic inhomogeneity with systematicity. Dr. Ripudaman Manchanda has provided excellent conceptual and code bugfixes to numerous projects, and in particular authored the implicit Carter leak-off formulation (which I like).

Generally, I would like to thank Hisanao Ouchi for being a terrific consigliere and late-night programming companion. On that note, I would like to thank those contributing to the open-sourcing of the finite volume/area sold mechanics toolset used to undertake this work. These persons include Drs. Philip Cardiff, Hrvoje Jasak, Željko Tuković, Tian Tang, and Alojz Ivanković. I thank the UT Austin Hydraulic Fracturing and Sand Control JIP for its support.

Abstract

Hydraulic Fracture Modeling with Finite Volumes and Areas

Eric Cushman Bryant, M.S.E.

The University of Texas at Austin, 2016

Supervisor: Mukul M. Sharma

In Chapter 1, a finite volume-based arbitrary fracture propagation model is used to simulate fracture growth and geomechanical stresses during hydraulic fracture treatments. Single-phase flow, poroelastic displacement, and in situ stress tensor equations are coupled within a poroelastic reservoir domain. Stress analysis is used to identify failure initiation that proceeds by failure along Finite Volume (FV) cell faces in excess of a threshold effective stress. Fracture propagation proceeds by the cohesive zone (CZ) model, to simulate propagation of non-planar fractures in heterogeneous porous media under anisotropic far-field stress.

In Chapter 2, we are concerned with stress analysis of both elastic and poroelastic solids on the same domain, using a FV-based numerical discretization. As such our main purposes are twofold: introduce a hydromechanical coupling term into the linear elastic displacement field equation, using the standard model of linearized poroelasticity; and, maintain the continuity of total traction over any multi-material interfaces (meaning an interface over which residual stresses, Biot's coefficient, Young's modulus, or Poisson's ratio vary).

In Chapter 3, we are concerned with modeling fluid flow in cracks bounded by deforming rock, and specifically, inside those initial discontinuities, softening regions and failed zones which constitute the solid interfaces of propagating hydraulic fractures. To accomplish this task the Finite Area (FA) method is an ideal candidate, given its proven facility for the discretization and solution of 2D coupled partial differential equations along the boundaries of 3D domains.

In Chapter 4, rock formations' response to a propagating, pressurized hydraulic fracture is examined. In order to initiate CZ applied traction-separation processes, an effective stress tensor is constructed by additively combining the total stress with pore pressures multiplied into a scalar factor. In effect, this scalar factor constitutes the Biot's coefficient as acts inside the CZ. Integral analysis at the cohesive tip is used to show that this factor must be equal to the Biot's coefficient in the bounding solid (for a small-strain constitutive relation). Also, effects of an initial residual stress state are accounted for.

Table of Contents

List of Tables

List of Figures

Chapter 1: Arbitrary fracture propagation in heterogeneous poroelastic formations using a finite volume-based cohesive zone model

One of the big challenges of modern fracture modeling is to develop engineering tools that allow for analysis of fracture trajectory response to poromechanical constitutive parameters. These include variations in Lamé's parameters, far-field stresses deviated with respect to the wellbore axis, and geological planes-of-weakness such as natural fractures. Fracturing models in the past have been designed to model the propagation of single, planar fractures in homogeneous porous media [1, 2]. These limitations stem from the underlying assumptions made, the numerical techniques used and the fact that these models are extended to solve the fluid flow and proppant transport problem inside the fracture. The rock matrix is represented only through boundary conditions for leak-off, elastic properties and normal far-field stress. This usually implies that the direction of fracture propagation is per-determined and specified in the model and the effect of rock heterogeneities (poroelastic layers, bedding planes, etc.) is difficult to account for.

Poroelastic mixed mode CZ models have been used to model the fracturing process, while also accounting for poroelastic effects in the solid domain. This model has been used in a variety of oil industry applications, including: combined vertical and horizontal fracture growth in quasi-brittle reservoirs [3], competing fracture growth [4], and to account for effects of plasticity [5]. Moreover numerical CZ implementations are becoming increasingly useful as efforts to reduce mesh bias mature – both in terms of propagation path and optimization of mesh refinement within the cohesive softening region [6, 7]. E.g., emergent meshing technology allows for random seeding of cell centers and construction of cell-centered continuum material meshes, after which Monte Carlo-based simulation runs are prescribed to conduct fracture trajectory analysis [8].

Yet near universally, computational CZ implementations have predicated use of the finite element (FE) method for stress analysis – often reliant on core features from licensed commercial solvers such as Abaqus. For instance, dependence on distinct element or FE methods for simulating discrete flow networks and coupled geomechanics is commonly assumed (c.f. [9]; for an extensive review article see [10]). However, a dependency on the FE method for stress analysis and fracture growth is no longer a necessity: associated with recent developments in FV computational solid mechanics, the FV discretization is now capable of stress analysis along multi-material interfaces. This method is sufficiently accurate to assess softening behaviors along those interfaces [11]. As inherently conservative, FV method-based techniques are well suited both for flow as well as for Biot's momentum balance equation for displacement within fractured porous media. FV advantages include: shared discretization of solid body mesh and similarity data structures for both displacement and flow field variables; use of a single software for solution of both equations; and, in-built co-location of boundary conditions for hydromechanical pressures and fracturing pressure leak-off along boundary cell faces [12].

This work combines FV method-based stress analysis for CZ-based fracture propagation in a poroelastic medium, for the first time. Coupling of displacement and Darcy flow equations is by fixed-strain split assumption. Heterogeneity is introduced in terms of both material toughness properties (e.g., [13]) and rock layers. FV method-based displacement values are corrected to account for discontinuity in gradient of displacement, along poroelastic material boundaries; a brief overview of this procedure is presented. A CZ model is used to calculate the cohesive tractions applied at the tips of propagating fractures, using a critical effective stress-based traction-separation law. Because of the bimaterial stress analysis – plus the initialization of spatially variable

fracture initiation criteria and toughnesses – the simulation of heterogeneities like bedding planes or natural fracture networks is naturally accommodated. Numerical solvers for field equations are modified from open source C++ library OpenFOAM solid mechanics extension [14, 15]. Mode I/II effective traction-based cohesive laws are modified from the same [16]. This open source project is further benefited by continuing contributions useful to model contact stresses during crack closure [17]. Both boundary cell non-orthogonality correction and relation of boundary gradients to applied stresses follow the scheme for orthotropic elasticity [18].

2D numerical examples are presented in order to show arbitrary, non-planar fractures in a porous medium. The effects of poroelasticity in the rock matrix are fully accounted for in the computations. This allows the fracture trajectory to be determined by the stress distribution around the tip (rather than prescribing a set orientation of the fracture) and the mechanical properties of the rock both in the vicinity of the tip and away from the tip. Variations in stress and pore pressure induced by heterogeneity are, therefore, accounted for as the fracture propagates. Both shear failure and tensile failure events in the rock matrix can be computed allowing us to track the shear events that occur as the fracture propagates. In our model, connected fractures are considered hydraulic in that fracture boundaries discharge leak-off, with pressure valued at injection pressure for fractures connected to the wellbore boundary. Connected fracture pressures are applied as a time-varying uniform boundary condition to both pressure and displacement field equations. Pressurized fractures removed by any distance from the propagating tip are not allowed. Hydraulic connectivity was assessed by examination of boundary cell face adjacency.

FIELD EQUATIONS

Biot's model of linear poroelasticity is employed where pores are assumed to be saturated by fluid. The strain tensor is constrained to be isotropic, and skeleton transformations constrained to be infinitesimal within the solid domain, with small variations of Lagrangian porosity. The linear elastic constitutive relations for the small strain tensor field and the volumetric strain scalar field are:

$$\boldsymbol{\varepsilon} = \frac{1}{2}[\nabla\mathbf{u} + (\nabla\mathbf{u})^{\mathrm{T}}], \quad (1)$$

$$\varepsilon_v = \mathrm{tr}(\boldsymbol{\varepsilon}) = \mathrm{tr}(\nabla\mathbf{u}) = \nabla \cdot \mathbf{u}. \quad (2)$$

where $\mathbf{u}$ is defined with respect to a reference configuration. The constitutive relation of poroelasticity relates the "increment of Biot's effective" ($\boldsymbol{\sigma} - \boldsymbol{\sigma}^0$), Biot's effective ($\boldsymbol{\sigma}$), and total stress ($\mathbf{S}$) tensors to the strain and hence displacement gradient tensor fields. The poroelastic constitutive relation is expressed under a TENSION POSITIVE convention [19]. The expression includes a residual effective stress tensor coupled at initialization as $\boldsymbol{\sigma}^0 = \mathbf{S}^0 + bp^0\mathbf{I}$, and which may obviously be zero-valued. The initial residual stress tensor usefully defines the far-field stress values and orientations, as well as the pore pressures in the undisturbed, in-situ state:

$$\boldsymbol{\sigma} - \boldsymbol{\sigma}^0 = 2\mu\boldsymbol{\varepsilon} + \lambda\varepsilon_v\mathbf{I}, \quad (3)$$

$$\mathbf{S} = \boldsymbol{\sigma} - bp\mathbf{I} = \mu[\nabla\mathbf{u} + (\nabla\mathbf{u})^{\mathrm{T}}] + \lambda\mathrm{tr}(\nabla\mathbf{u})\mathbf{I} + \boldsymbol{\sigma}^0 - bp\mathbf{I}. \quad (4)$$

In Eq. (4) as a function of Young's modulus E and Poisson's ratio ν, Lamé's first and second parameters are,

$$\mu = \frac{E}{2(1+\nu)}, \quad (5)$$

$$\lambda = \begin{cases} \dfrac{\nu E}{1-\nu^2} & \text{for plane stress,} \\ \dfrac{\nu E}{(1-2\nu)(1+\nu)} & \text{for plane strain and 3D.} \end{cases} \quad (6)$$

The above means that practically, the identity of λ may change for 2D simulations based upon the enforcement of compatibility conditions (e.g. plane stress compatibility). The poroelastic equation for quasi-static mechanical equilibrium can be expressed, in the absence of body forces, as:

$$\oint_S \mathbf{n} \cdot (\mathbf{S} = \boldsymbol{\sigma} - bp\mathbf{I}) \mathrm{d}S = \mathbf{0}. \quad (7)$$

Additionally, to solve Eq. (7), the currently predominant FV method-based solution methodology discretizes the implicit component of the displacement field with a dominant vector Laplacian term, labeled "Implicit,"

$$\overbrace{\int_V \nabla \cdot (bp\mathbf{I}) \mathrm{d}V}^{\text{Pore Pressure Coupling}} = \overbrace{\int_V \nabla \cdot \boldsymbol{\sigma}^0 \mathrm{d}V + \oint_S \mathbf{n} \cdot (2\mu + \lambda) \nabla \mathbf{u} \mathrm{d}S}^{\text{Implicit Component}} + \overbrace{\oint_S \mathbf{n} \cdot [\mu(\nabla \mathbf{u})^{\mathrm{T}} + \lambda \mathrm{tr}(\nabla \mathbf{u})\mathbf{I} - (\mu + \lambda)\nabla \mathbf{u}] \mathrm{d}S}^{\text{Explicit Component}}. \quad (8)$$

The accuracy of Eq. (8)'s solution is driven by the displacement field's explicit component, which not only lumps non-linear terms but also terms related to the numerical correction applied at bi-material interfaces. To arrive at the quasi-static $p - \mathbf{u}$ coupling of linearized poroelasticity, small variations in fluid mass density are assumed.

Here to solve the pore fluid flow equations, horizontal Darcy flow without gravity effects is assumed (for summary see [21]),

$$\overbrace{\int_V b\frac{\partial(\nabla\cdot\mathbf{u})}{\partial t}\mathrm{d}V}^{\text{Displacement Coupling}} + \int_V \frac{1}{M}\frac{\partial p}{\partial t}\mathrm{d}V = \overbrace{\oint_S \mathbf{n}\cdot\left(\frac{\mathbf{K}_p}{\mu_p}\nabla p\right)\mathrm{d}S}^{\text{Implicit Components}}. \quad (9)$$

In order to simultaneously converge a solution to the coupled problem of Eq. (8) and Eq. (9), the numerical solution methodology is to perform a series of Picard iterations. Dry bulk modulus as well as Biot's coefficient and modulus are defined in the usual manner:

$$K_d = \frac{2}{3}\mu + \lambda, \quad (10)$$

$$b = 1 - \frac{K_d}{K_s}, \quad (11)$$

$$\frac{1}{M} = \frac{b-\phi^0}{K_s} + \frac{\phi^0}{K_p} = (1-b)\frac{b-\phi^0}{K_d} + \frac{\phi^0}{K_p}. \quad (12)$$

Eq. (8) and Eq. (9) are coupled by a fixed-strain split assumption (for coupling alternatives and descriptions, see [22, 23]). This approximation has been found to be useful for coupling with multi-phase flow equations [24].

Verification of geomechanical model

With respect to the validation case presented, it is helpful to define the undrained bulk modulus K_u, and secondarily diffusion coefficient c with respect to the eigenvalue k_p of the isotropic permeability tensor:

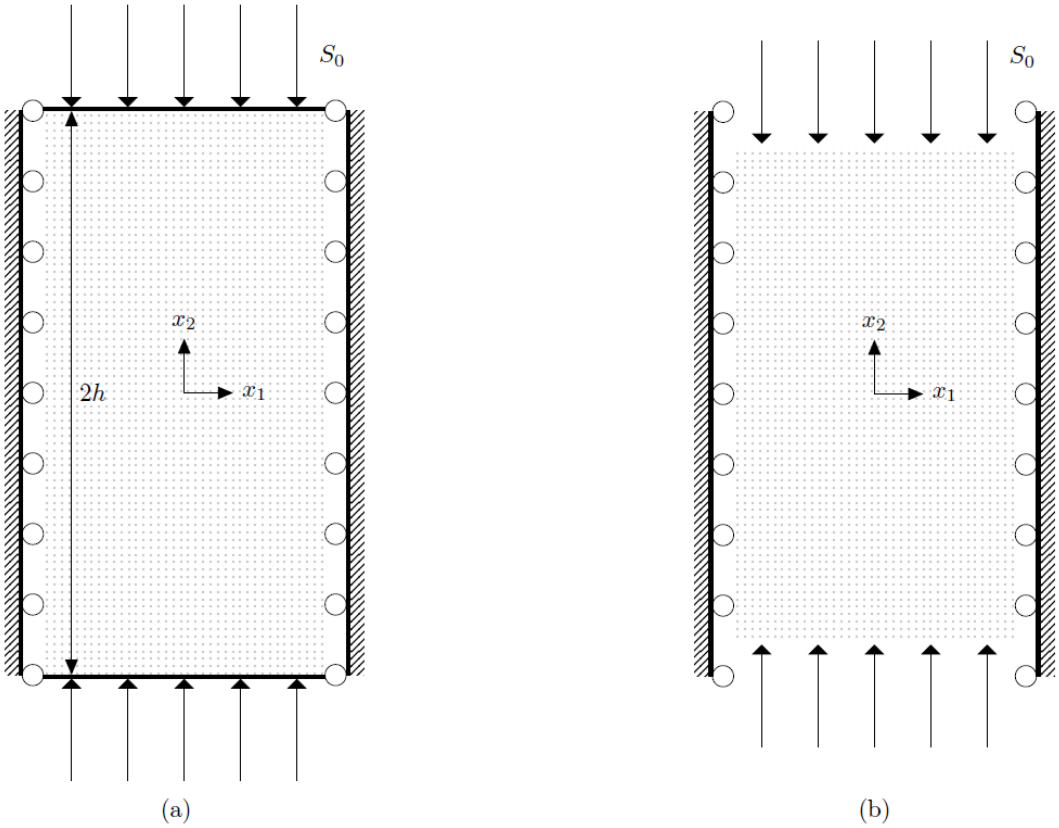

Figure 1: Terzaghi's problem test case, (a) phase 1 loading and (b) phase 2 loading.

$$B = \frac{bM}{K_u} = \frac{bM}{K_d + b^2 M}, \quad (13)$$

$$c = \frac{k_p M}{\mu_p}\left(\frac{K_d + \frac{4}{3}\mu}{K_u + \frac{4}{3}\mu}\right) = \frac{k_p}{\mu_p}\left(\frac{1}{M} + \frac{b^2}{2\mu + \lambda}\right)^{-1}, \quad (14)$$

$$\nu_u = \left(\nu + \frac{bB(1-2\nu)}{3}\right)\left(1 - \frac{bB(1-2\nu)}{3}\right)^{-1}. \quad (15)$$

The poroelastic coupling is validated against Terzaghi/Biot's one-dimensional consolidation problem [25], with material properties listed in Table 1. A rectangular

column with height $2h$ of 40 m was held at an initial uniform pressure of 0 Pa. During phase 1, a downward normal traction S_0 of 1E+5 Pa was applied on to the column. The symmetric half-volume was simulated, with no displacement allowed at the middle. Zero outward displacement conditions were applied on other boundaries. No flow was allowed through any boundary. The final phase 1 pressure inside the column was computed to be 36,448 Pa, and matches the linearized analytic solution. Phase 2 entailed relieving the no-flow boundary condition at the top and bottom boundaries by application of a zero pressure condition. The loading conditions are shown Fig. 1.

For our reference solution, the top of the column is located at x_2 = h where the load is applied. Results for pressure during phase 2 are as presented in Fig. 2, and displacement in Fig. 3. The initial pore pressure, and the time-varying pore pressures are [26]:

$$p_0 = bM\left(\frac{1-2\nu_u}{2\mu(1-\nu_u)}\right)S_0, \tag{16}$$

$$p(x_2,t) = \frac{4}{\pi}p_0\sum_{m=0}^{\infty}\left[\frac{1}{2m+1}\exp\left(-\left(\frac{(2m+1)\pi}{2h}\right)^2 ct\right)\sin\left(\frac{(2m+1)\pi}{2h}(h-x_2)\right)\right]. \tag{17}$$

The analytic solution for displacements in the x_2-axis direction is:

$$u_{2,0}(x_2) = -\left(\frac{1-2\nu_u}{2\mu(1-\nu_u)}\right)S_0x_2, \tag{18}$$

$$u_2(x_2,t) = u_2(x_2)_0 - \left(\frac{\nu_u-\nu}{2\mu(1-\nu_u)(1-\nu)}\right)S_0 \times \left\{\frac{8h}{\pi^2}\sum_{m=0}^{\infty}\frac{1}{(2n+1)^2} \times \left[1-\exp\left(-\left(\frac{(2m+1)\pi}{2h}\right)^2 ct\right)\right]\cos\left(\frac{(2m+1)\pi}{2h}(h-x_2)\right)\right\}. \tag{19}$$

The results for the numerical model overlay the analytical results.

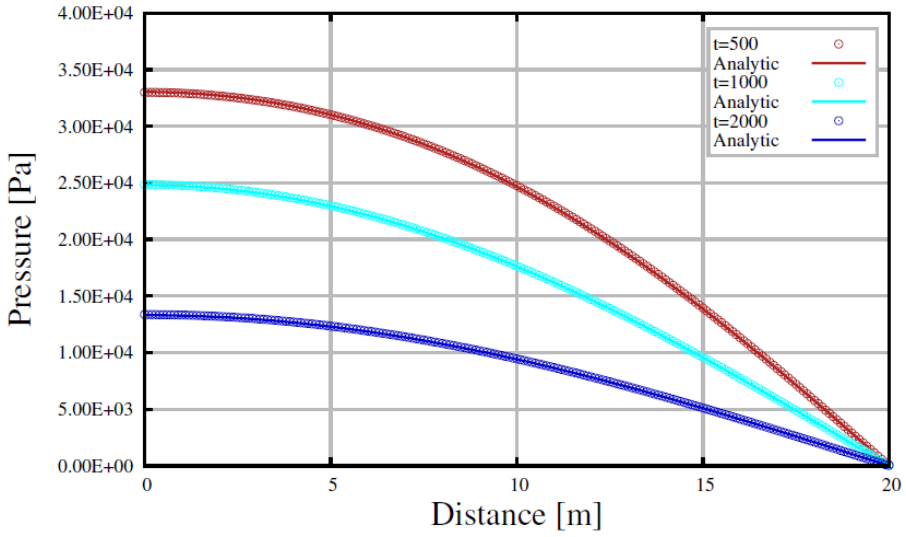

Figure 2: Terzaghi's problem test case, recovered pore pressures.

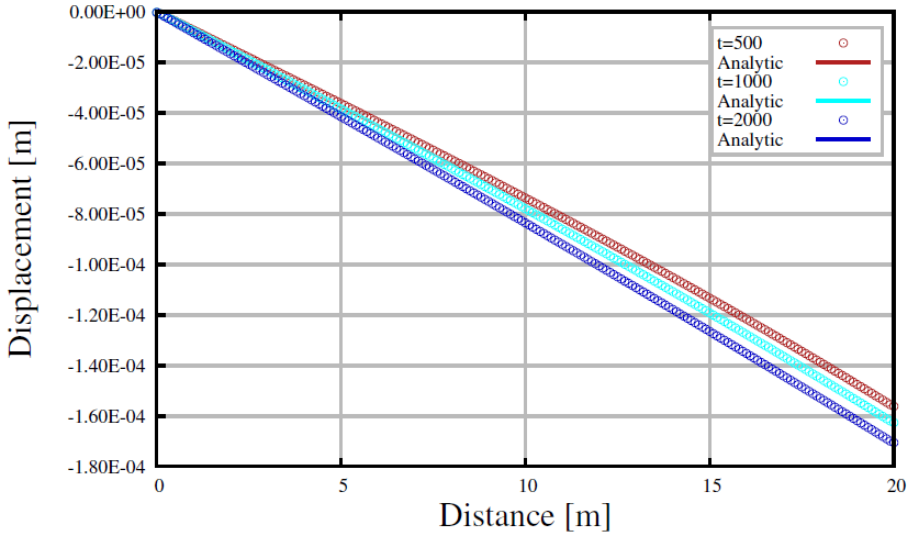

Figure 3: Terzaghi's problem test case, recovered displacements.

Bimaterial interfaces mark the location of a jump in the skeletal Lamé's parameters. Because of the cell-centered discretization, they are located along internal FV cell faces. Because it assumes a continuous cell-to-cell displacement gradient, such interfaces are not accounted for by solution of the continuum-internal displacement equation Eq. (8). Tractions are continuous. Thus simple application of Hooke's law shows a strain change across an interface between materials with different Young's moduli. Fortuitously a means to correct for these effects has previously been developed for elasticity. The approach improves stress analysis within bimaterial domains at the interface where Lamé's parameters jump. The approach is to enforce continuity of the resolved traction along each side of the interface, and so prevent unphysical stress peaking [11].

For a constant Biot's coefficient and "open pore" continuity conditions, Tuković's interface correction methodology can straightforwardly be extended to linearized poroelasticity and use of a residual stress tensor. Note the resemblance of Eq. (8) to the linear elastic equation [15]:

$$\underbrace{\int_V \frac{\partial^2 \mathbf{u}}{\partial t^2}\,\mathrm{d}V}_{\text{Dynamic Implicit Component}} = \underbrace{\oint_S \mathbf{n}\cdot(2\mu+\lambda)\nabla\mathbf{u}\,\mathrm{d}S}_{\text{Implicit Component}} + \underbrace{\oint_S \mathbf{n}\cdot[\mu(\nabla\mathbf{u})^{\mathrm{T}}+\lambda\mathrm{tr}(\nabla\mathbf{u})\mathbf{I}-(\mu+\lambda)\nabla\mathbf{u}]\mathrm{d}S}_{\text{Explicit Displacement Term}} \quad (20)$$

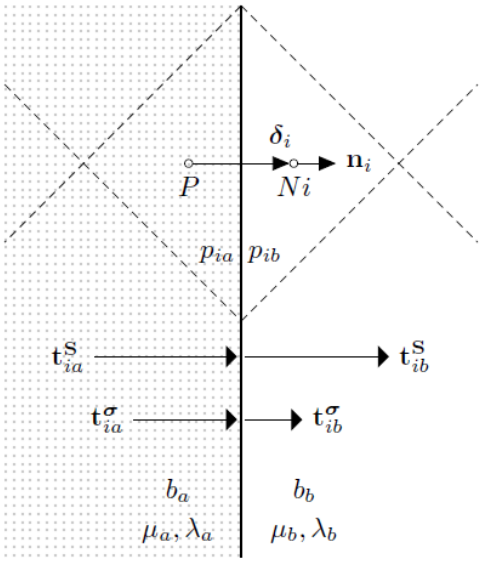

Figure 4: Closed pore continuity conditions along multi-material interface (dotted line) discretized as perpendicular to vector connecting cell center locations across interface, and continuum cell boundaries (dashed lines), (after [11]).

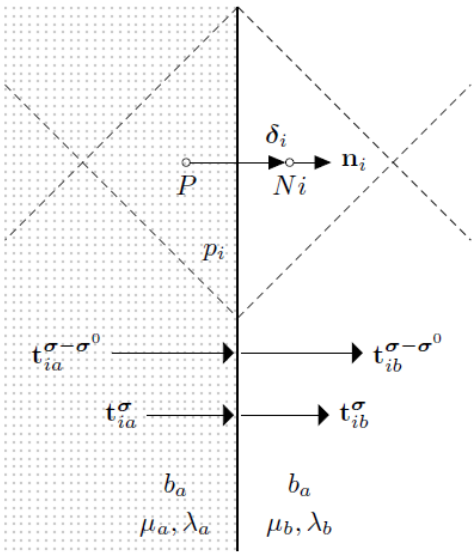

Figure 5: Reduced set of apt continuity conditions along open-pore multi-material interface, where a homogeneous Biot's coefficient implies continuity of resolved effective stress.

Clearly the second and third terms of Eq. (20) are identical to third and fourth term of Eq. (8): both equations utilize a dominant implicit vector Laplacian (having internal coefficient $2\mu + \lambda$), and contain an identical explicit function of the displacement gradient. The dynamic term is simply eliminated for quasi-static couplings.

Without complex and lengthy derivation, we easily demonstrate the validity of our approach. We write the traction, "effective traction" (resolved Biot's effective stress), and current increment of effective traction for the poroelasticity relation of Eq. (4):

$$\mathbf{t_S} = \mathbf{n}\cdot\mathbf{S} = \mathbf{t_\sigma} - bp\mathbf{n} = \mathbf{t_{\sigma-\sigma^0}} + \mathbf{n}\cdot\boldsymbol{\sigma}^0 - bp\mathbf{n}, \quad (21)$$

$$\mathbf{t_\sigma} = \mathbf{t_{\sigma-\sigma^0}} + \mathbf{n}\cdot\boldsymbol{\sigma}^0, \quad (22)$$

$$\mathbf{t_{\sigma-\sigma^0}} = \mathbf{n}\cdot(\boldsymbol{\sigma}-\boldsymbol{\sigma}^0) = \mu\mathbf{n}\cdot\nabla u + \mu\nabla\mathbf{u}\cdot\mathbf{n} + \lambda\mathrm{tr}(\nabla\mathbf{u})\mathbf{n}. \quad (23)$$

Different properties on the two sides of a poroelastic bimaterial interface are designated with subscripts ia and ib, and the value at the interface is subscripted with i. The sign convention of $\mathbf{n}_i$ is outward positive from the current interface cell's center. Fig. 4 presents the schematic, representing a closed pore interface where pressures are discontinuous (as well as Biot's coefficient). The closed pore scenario would imply no-flow, because one or more of the interface materials is impermeable.

For this work, we assume that a representative pore pressure is obtainable at the interface – and further, the pressure is known to be identical on both sides of the interface. As such, the open pore continuity of both traction and pore pressure are assumed [27]. Relevant continuity assumptions are:

$$\mathbf{t}_{ia}^{\mathbf{S}} = \mathbf{n}_i\cdot\mathbf{S}_{ia} = \mathbf{n}_i\cdot\mathbf{S}_{ib} = \mathbf{t}_{ib}^{\mathbf{S}}, \quad (24)$$

$$p_{ia} = p_{ib}. \quad (25)$$

Variations in Biot's coefficient or resolved component of the initial stress tensor over the interface are not considered, and these fields are required to be invariant. Fig. 5 shows the

open-pore, homogeneous Biot's coefficient scenario. In the absence of body forces, reasonable scenarios used to properly initialize the residual stress tensor will maintain the continuity of initial traction over the interface. Such that:

$$\mathbf{n}_i \cdot \boldsymbol{\sigma}_{ia}^0 = \mathbf{n}_i \cdot \boldsymbol{\sigma}_{ib}^0, \quad b_{ia} = b_{ib}. \qquad (26)$$

The substitution of Eq. (25) and Eq. (26) into Eq. (24) obtains the equality of the increment of effective tractions. Usefully with respect to poroelasticity, only the traction normal component $-b_i p_i \mathbf{n}_i$ need be considered. As such, the traction continuity Eq. (25) reduces upon those assumptions to continuity of incremental effective traction:

$$\mathbf{t}_{ia}^{\boldsymbol{\sigma}-\boldsymbol{\sigma}^0} = \mathbf{t}_{ib}^{\boldsymbol{\sigma}-\boldsymbol{\sigma}^0}. \quad (27)$$

In that Tuković's analysis relies only on the continuity of vectors numerically identical to the normal and tangential components of the increment of effective traction – thus, it has just been shown that the same analysis is equally applicable for poroelastic domains where Eq. (26) holds. (Parenthetically, the continuity of interface displacements, also a condition of the analysis, is de facto enforced by natural collocation of cell boundaries at the interface FV cell faces.) The bimaterial correction by enforcing said continuity, therefore captures an accurate: displacement gradient, thus strain, and hence stress state along material interfaces.

The bimaterial correction allows FV-based numerics to accurately model fracture propagation either through or along rock layer boundaries. Moreover, the procedure enhances stability of growth models. Failure to implement such a correction (combined with the domain-wide evaluation of softening behavior as with the CZ model) may result in a sudden, massive, and physically unwarranted de-bonding at strongly discontinuous interfaces. Lastly as to the numerical mesh quality required, increasing mesh skewness in

general worsens convergence. The bimaterial procedure can account for skewness of interface faces. But skewness-handling requires: decomposition of the displacement gradient, plus vertex-based schemes [28, 29].

Fractures and failure criteria

Fractures are modeled as a discontinuity – viz. having width $-\mathbf{n}_b \cdot \mathbf{u}_b$ where subscripting b marks a boundary value. The width is computed from the resolved displacements at the boundary of the numerical mesh, that represents the formation. Arbitrary crack growth has been implemented using a FV cell-face detachment method in foam-extend [16]; the model was extended with use of Tuković's interface correction to analysis of material interfaces [30]; numerically, softening behavior is applied using dynamic meshing with face detachment methods. The library incorporates the same core numerical implementation of the CZ model, but with an extended feature set which includes the capacity to simulate pressure-driven cracks, and implements the poroelastic failure model by use of the effective stress tensor.

Hence, the hydraulic fractures are propagated using essentially a standard CZ model. Accordingly, in order to determine failure along FV cell-faces, the components of effective tractions are resolved onto all cell faces within the cohesive volume:

$$\boldsymbol{\sigma}^f = \mathbf{S} + b^f p\mathbf{I} = \boldsymbol{\sigma} + (b^f - b)p\mathbf{I}, \quad (28)$$

$$\mathbf{t}_n^f = \mathbf{nn} \cdot (\mathbf{n} \cdot \boldsymbol{\sigma}^f), \quad (29)$$

$$\mathbf{t}_t^f = (\mathbf{I} - \mathbf{nn}) \cdot (\mathbf{n} \cdot \boldsymbol{\sigma}^f). \quad (30)$$

The coefficient b^f lies within the physical range $b \leq b^f \leq 1$ and for $b^f = 1$ reduces $\boldsymbol{\sigma}^f$ to the Terzaghi effective stress; for a purely elastic material $b^f = 0$, $\boldsymbol{\sigma}^f$ reduces to the total stress. For fracturing models presented here, $b = b^f$. Basic J-integral analysis of

loading at in the CZ evidences that $b = b^f$ most mimetically re-produces the linear elastic fracture mechanics (LEFM) analogue.

The norms of effective traction components $\mathbf{t}_n^f$ and $\mathbf{t}_t^f$ are then compared using the effective normal and tangential critical stresses $(\sigma_n)_c$, and $(\sigma_t)_c$, respectively, which are material properties bearing a loose relation to the effective tensile and shear material strengths. Additionally, the set of normal components of the effective traction field ($\mathbf{t}_n^f$) is filtered to include only tensile traction components. After filtering, failure initiation is then determined by computing the Mode I/II norm:

$$\left(\frac{\|\mathbf{t}_n^f\|}{(\sigma_n)_c}\right)^2 + \left(\frac{\|\mathbf{t}_t^f\|}{(\sigma_t)_c}\right)^2 \begin{cases} \geq 1^2 & \textit{potentially} \text{ a broken face, if } \mathbf{n} \cdot \mathbf{t}_n^f \geq 0, \\ < 1^2 & \text{not yet failed.} \end{cases} \quad (31)$$

To create discrete fractures discretized by the volume of the fracture-boundary displacements, the implementation of FV cell-face failure is by release methods: crack-tip faces which fail based upon this criterion are said to “break”; those mesh points topologically conjoining the newly detached faces must “split”. Failed, detached faces within the cohesive volume either have, or have not, depleted the fracture energy associated with their surface area (Fig. 6). If they are in excess of the fracture energy, the faces are not subject to tensional traction. Otherwise these faces fall inside the CZ or “softening region”, and the coupled faces are subject to an inward traction resisting further outward displacement.

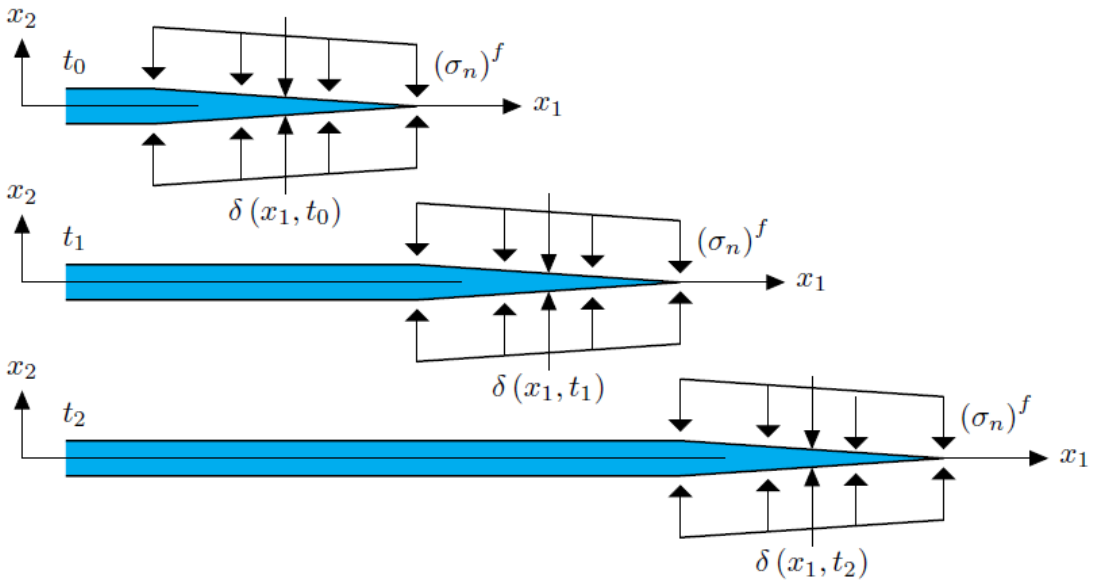

Figure 6: Fracture tip and CZ in time (after [31]).

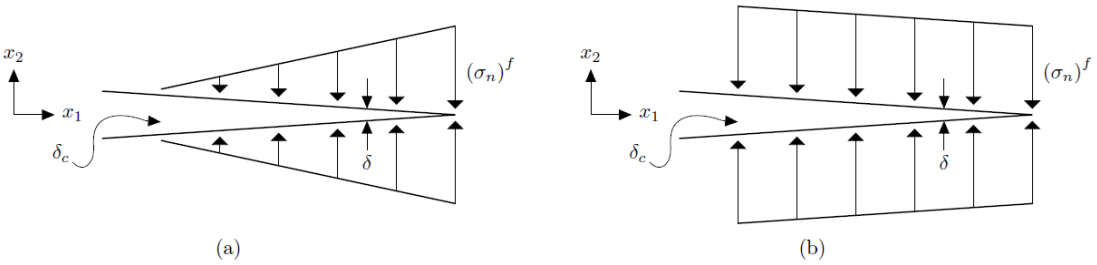

Figure 7: Cohesive (a) linear and (b) Dugdale models.

Porosity, ϕ^0 [-]	0.2
Permeability, k_p [m^2]	1.5E-14
Biot's Coefficient, b [-]	0.6
Young's Modulus, E [Pa]	1E+10
Poisson's Ratio, v [-]	0.2
Viscosity, μ_p [Pa-s]	0.001
Fluid Bulk Modulus, K_p [Pa]	2.3E+9
Downward normal traction, S_0 [Pa]	1E+5

Table 1: Terzaghi's Problem

During the face-breaking process, the normal and shear components of resolved effective stress at failure ($\mathbf{t}_n^f$ and $\mathbf{t}_t^f$) are stored as initial "initiation tractions". Cohesive tractions imposed within the CZ discount the initiation tractions based upon separation distance during the current solver iteration. Traction-separation laws relate maximum tensile and shear effective tractions to fracture energy, Fig. 7. For example, for a linear Mode I traction-separation law the cohesive tractions are approximated as:

$$\delta_c = 2\frac{G_{Ic}}{(\sigma_n)_c}, \tag{32}$$

$$(\mathbf{t}_n^f)_b = \begin{cases} (\mathbf{t}_n^f)^0\left(1-\frac{\delta}{\delta_c}\right) & \text{for } \delta < \delta_c, \\ 0 & \text{otherwise.} \end{cases} \tag{33}$$

Hence, the opening of failed faces toward a critical separation distance δ_c is used to discount the applied cohesive tractions (as long as the face remains within the CZ). The relationship between the current separation distance δ and the cohesive tractions is, therefore, a function of the traction-separation law employed: for instance in the case of a single-mode linear traction-separation law, this relationship is $G_{Ic} = \frac{1}{2}(\sigma_n)_c\delta_c$ as above.

(Here, the 1/2 factor is used to associate surface energy with the area of each half-surface of new fracture. The convention is repeated in the KGD model comparison.)

In the general case however, it may be desirable to consider mode mixity of surface energy depletion in order to model both tensional and shear-induced fracture growth. In that instance, the current surface energy release rates G_{Ic} and G_{IIc} are numerically integrated by multiplication of directional displacement and applied cohesive tractions. Where mode mixity of release rates during the cohesive softening is considered, the following metric is computed and compared to unity:

$$\frac{G_I}{G_{Ic}} + \frac{G_{II}}{G_{IIc}} \begin{matrix} \geq 1 & \text{face leaves CZ,} \\ < 1 & \text{face remains inside CZ.} \end{matrix} \quad (34)$$

Fracture energies G_{Ic} and G_{IIc} are model inputs.

Comparing external stress to fracture pressure at the boundary cell face (for a tension positive sign convention, and with fracture pressure acting as a compressive external force), the cohesive tractions reduce to an effective stress boundary condition [32, 33]:

$$\mathbf{t}_b^f = (\mathbf{t}_n^f)_b + (\mathbf{t}_t^f)_b, \quad (35)$$

$$(\mathbf{t_s})_b = \begin{cases} \mathbf{t}_b^f - b^f p^f \mathbf{n}_b & \text{inside CZ,} \\ -p^f \mathbf{n}_b & \text{otherwise as } \mathbf{t}_b^f = \mathbf{0}. \end{cases} \quad (36)$$

The incremental formulation of Hooke's law, Eq. (4), describes the tractions for a small surface area along the fracture boundary. Conversion of prescribed boundary tractions to gradients of displacement is discussed elsewhere. Nevertheless it is interesting to note the following fact. Along the physical fracture, let the boundary condition to the displacement field Eq. (8) be:

$$(\mathbf{t}_{\boldsymbol{\sigma}-\boldsymbol{\sigma}^0})_b = -p^f \mathbf{n}_b + \begin{cases} -\mathbf{n}_b \cdot \mathbf{S}_b^0 & \text{adequate for stress shadow only,} \\ -\mathbf{n}_b \cdot \boldsymbol{\sigma}_b^0 + b_b p_b \mathbf{n}_b & \text{accounts for poroelasticity.} \end{cases} \quad (37)$$

Eq. (37)a is adequate to consider stress shadow effects, as between competing fractures. However, Eq. (37)b additionally accounts for poroelastic effects in the near-fracture region. This is also referred to as "back-pressure" or "back-stress" resulting from pressure continuity during leak-off. Alternatively simulations are initialized with traction boundary conditions. In this instance, stress concentrations in the far-field do not initiate Mode I/II failures, enforced by elimination of far-field cells from the cohesive zone volume. (Here, the "arbitrary" propagation criterion is that fractures may "nucleate" at any cell-cell interface within the subset of a discretized reservoir domain described by limits of an initialized cohesive zone volume.) As above, leak-off into the formation was modeled using fracture pressure as a pore pressure boundary condition:

$$p_b = p^f. \quad (38)$$

The volumetric rate of leak-off was computed by solving Eq. (9).

Benchmarking

Benchmarking of the failure criteria and traction-separation curves was achieved for proscribed fixed outward displacements of a body in tension, until failure at the vertical half-mark (Table 2). For benchmarking, mixed Mode I/II bonding behavior was held as isotropic for both energy release rate and failure behavior; conditions for isotropic fracture energy and isotropic material failure were, respectively, $G_c = G_{Ic} = G_{IIc}$ and $(\sigma_n)_c = (\sigma_t)_c$.. The strain energy stored within the upper and lower half of this body, immediately before failure, is:

Young's Modulus, E [Pa]	1E+10
Poisson's Ratio, v [-]	1E-7
Fracture Energy, G_c [J/m^2]	400
Critical Stress, $(\sigma_n)_c$ [Pa]	20E+6
Width and Depth [m]	1E-3
Height, h [m]	2E-3
Pre-Failure Strain Energy [J]	2E-5

Table 2: CZ Benchmarking Parameters

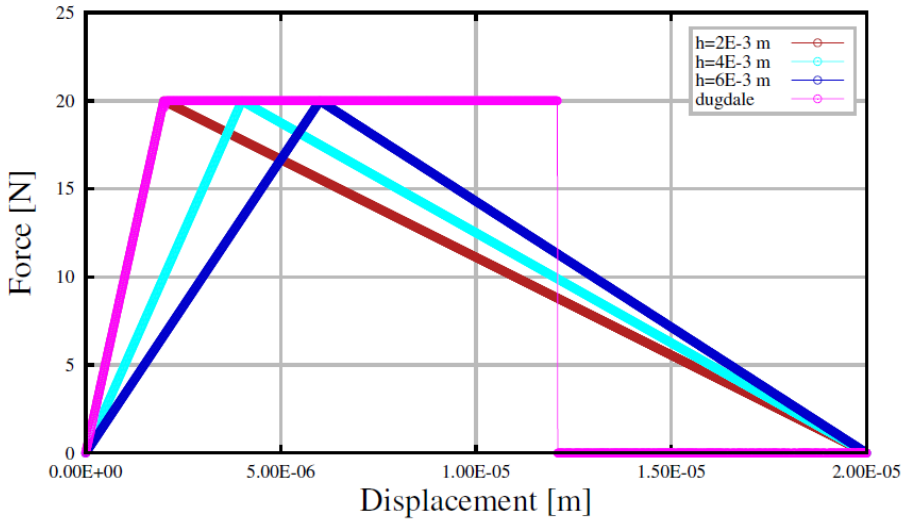

Figure 8: CZ benchmarking test case, recovered force-displacement curves.

$$U_c = \frac{h}{2}\frac{(\sigma_n)_c^2}{E}A. \quad (39)$$

A force-displacement history for variously sized bodies (heights, h) was recorded (Fig. 8). The elastic strain energy U_c stored prior to failure was measured by integration of force-displacement curve from zero displacement (undeformed configuration) until the curve's peak. Cohesive traction boundary conditions are applied to each boundary cell face during softening; for the benchmarking simulations, $b = 0$.

The numerical error associated with strain energy accumulation prior to failure initiation (at peak) was 0.16%, for both Dugdale and linear laws. The Dugdale law CZ model implementation recovered normalized fracture energy per unit area with 1.07% error, by integration of the force-displacement curve during cohesive traction-separation process only. The linear traction-displacement law curve was integrated from initial displacement (area under the entire curve), recovering fracture energy within 0.04% error in Fig. 8. Results were independent of the number or configuration of cells discretized within the body. Fracture faces leave the active cohesive zone after achieving a critical separation distance, e.g. 0.02 mm in Fig. 8.

Cohesive material parameters

Our simple approach to CZ model implementation distinguishes elastic from poroelastic cohesive zone loading. This approach entails: allowing the fracture fluid flow to penetrate within the CZ; setting surface permeability in the zone to vary with fracture width; and, an effective stress-based cohesive traction-separation law. This conceptualization has been used with a cohesive zone length with magnitude of order 1 m, in order to match a Khristianovich-Geertsma-de Klerk-type reference solution using a cubic law transmissivity (c.f. [31]). Following Carrier's idea, fracture transmissivity

within the fracture is dominated by localized porosity enhancements induced by a more tensile stress state. Flow within the cohesive zone operates at positive net pressures, and is a function of the induced permeability. (Dry tip phenomena are not considered here.) At critical stresses of order 1E+6 Pa, the CZ model/FV method implementation is numerically less likely to operate within a regime where distended traction-separation curves are recovered (unlike Fig. 8).

This approach admits a physical interpretation of the CZ model critical effective normal stress (under certain conditions): the effective tension at which cohesive processes initiate, and therefore cause a small volumetric increase in the pore space of the tensile CZ region. Although minute, this slight increase in pore volume is nonetheless potentially sufficient to convey fracture fluids (as and if present). The pressure gradient in this zone is better approximated by a fracture than the reservoir permeability. That said, numerically, the fluid-filled CZ also exhibits more monotonic recovery in fracture dimensions such as aperture. Physically, the effective normal critical stress is bounded at its upper limit by the reservoir rock's effective tensile strength. Numerically, the critical normal stress is sufficiently low to ensure no detached cell face enters and immediately exits the CZ.

Depth [ft.]	4000
Pore pressure, p^0 [Pa]	8.9E+6
Vertical Stress, S_V [Pa]	20.7E+6
Horizontal Min. Stress, S_{hmin} [Pa]	12.8E+6
Horizontal Max. Stress, S_{Hmax} [Pa]	15.0E+6
Porosity, ϕ^0 [-]	0.25
Permeability, k_p [m^2]	1E-14
Biot's Coefficient, b [-]	1.0
Young's Modulus, E [Pa]	90E+9
Poisson's Ratio, v [-]	0.25
Viscosity, μ_p [Pa-s]	0.001
Fluid Bulk Modulus, K_p [Pa]	2.3E+9

Table 3: Geomechanical Parameters

Formation Fracture Energy, G_c [J/m^2]	400
NF Fracture Energy, G_c [J/m^2]	100
Formation Critical Stress, $(\sigma_n)_c$ [Pa]	0.5E+6
NF Critical Stress, $(\sigma_n)_c$ [Pa]	0.2E+6

Table 4: Energy Parameters.

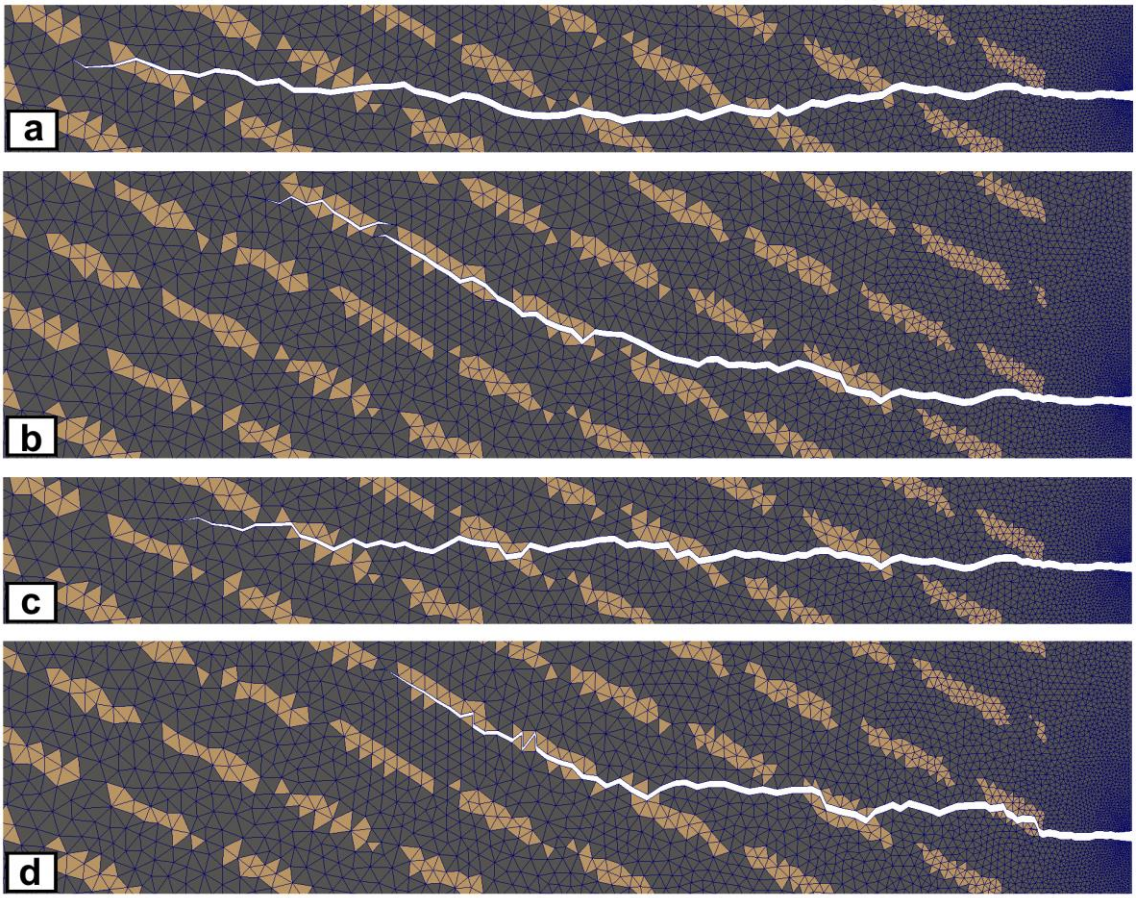

Figure 9: Fractures propagated along boundaries of original discretization (in blue): (a) no heterogeneity of parameters; (b) with anisotropic and varying parameters of toughness and critical stress; (c) heterogeneity with increased magnitude of far-field stress contrast; and, (d) with isotropic critical stresses and original stress contrast, magnified at 100x displacement.

NUMERICAL RESULTS

A fracture was considered to be propagating when a mixture of cohesive zone and completely failed faces were present along the fracture boundary (decided by Eq. (34)). For all simulations small starter fractures are discretized, with lengths on the order of ~0.01-0.5 m. Pressure pulses of high normal traction are applied to starter fractures, in

order to initiate propagation, with a fixed number of failed faces allowed per time step. During mature propagation net pressures would resolve a tip stress exceeding CZ model critical stresses; at this point, fracture boundary tractions were diminished, reducing to a net pressure ~0.5-3E+6 Pa (depending on critical stress values, permeabilities, and discretization). Default parameters and formation initial total stresses are as given in Table 3.

Fractures are shown as white discontinuities in the formation. Fractures are constrained to propagate along existing faces of original discretization, connected fractures are infinitely conductive, and material boundaries must follow original cell boundaries [34, 12]. Cell boundaries are shown occasionally to indicate the total set of available fracture paths. Stable fracture propagation is feasible using: (a) fixed displacement and symmetry far-field boundary conditions; or, (b) an initial stress tensor $\mathbf{S}^0$. combined with the resolved tractions along the far boundaries $\mathbf{n}_b \cdot \mathbf{S}_b^0$. This initialization method is practically useful for oil industry applications – and in particular for simulations utilizing a multi-material interface – in order to avoid shearing during initialization via application of compressive tractions.

Planes-of-weakness

Our first model (Fig. 9) shows the capability to simulate natural fracture networks, bedding planes, or other planes-of-weakness. Under this model, the results show that variations in induced fracture propagation path are controlled by the stress contrast and the critical effective normal and tangential stresses, $(\sigma_n)_c$, and $(\sigma_t)_c$. These critical stresses are reduced along natural fractures, causing the fractures to turn along planes-of-weakness. Toughness and fracture energy properties have secondary effects on propagation direction. Energy release rates dominate fracture widths in the cohesive zone

region, per the traction-displacement curve. In contrast, fracture trajectories in homogeneous reservoirs are aggregately straight.

Fractures in Fig. 9a through 9d initiate from the right-hand-side boundary and propagate left, with fracture critical stresses and toughness reduced only for cell-cell boundaries between lighter-colored cells. The base-case simulation Fig. 9a shows aggregately straight path of propagation up to a length of 24 m. The fracture toughness and critical stress properties for both the formation and the planes-of-weakness are identical, and valued as formation properties given in Table 4. Straightness of the base-case trajectory is facilitated by anisotropy in the imposed far-field stresses and by the symmetry boundary condition at the boundary along which the fracture was initiated (Fig. 9, right boundary). This condition forces zero perpendicular displacement along the boundary, effectively resisting any torque developed along that boundary imposed by fracture path deviation from a plane. Notably, this reservoir is discretized using a Delaunay-triangulated mesh ([35]). Uniformity of cell-face length and hence cohesive zone length are not considered in all simulations, though are recognized as engineering choices for CZ modeling ([36]). Instead, natural-fracture-adjacent cell sizes have been increased to show cell-face network pattern while evidencing fracture propagation of meaningful length.

In Fig. 9b the fracture toughness of the planes-of-weakness are changed and are given in Table 4. Simulations with formation Mode II tangential critical stress varying from 0.5E+6 to 5E+6 Pa were conducted, but without causing a significant variation in the fracture trajectory – propagation was dominantly Mode I. In Fig. 9c the fracture toughness values were kept the same as for Fig. 9b. However, the maximum far-field horizontal stress was increased to a value of 19.0E+6 Pa. The resultant fracture propagates aggregately along a straight path, while exhibiting occasional forward de-

bonding along weaker interfaces of low critical effective stress. Fig. 9 shows fractures while net pressure is maintained at 1.1E+06 Pa, although all fractures are stably propagated to an ultimate net pressure of 0.5E+06 Pa and aperture of 1.8 mm.

In Fig. 9d the tangential and normal critical effective stresses were decreased to 0.2E+6 Pa for the planes-of- weakness. Shearing occurs near the hydraulic source, increasing near-wellbore complexity. Fig. 9b and Fig. 9d simulations were run with low stress contrast and share a characteristic propagation path pattern: opening of fractures disconnected from the main fracture, or forward-lateral de-bonding, causing subsequent fracture turning to join with de-bonded regions (observable in Fig. 9b). Regarding the orientation of failed faces in Fig. 9, the jaggedness of the configuration of failed faces produced (as the boundary of a simulated propagating fracture) poses problems unaddressed by [12]. Pressures are applied as scalar values multiplied by the face normal of any particular face within the connected fracture. The component of the resultant traction vector which acts in the same direction as the face normals of adjacent boundary faces, counteracts pressures applied on those adjacent faces. Clearly, this effect has no impact on planar hydraulic fractures modeled using orthogonal Cartesian meshes.

Reversal of in-situ stress direction

Our second model (Fig. 10) shows differing fracture trajectories based upon arbitrarily directed maximum and minimum principal stresses. Where the direction of horizontal maximum and minimum principal stresses is swapped, the direction of fraction propagation is reversed. Simultaneous fracture propagation is simulated. No material parameter or other aspect of the discretization is altered between the two simulations – otherwise geometry, meshes, and physical properties are identical.

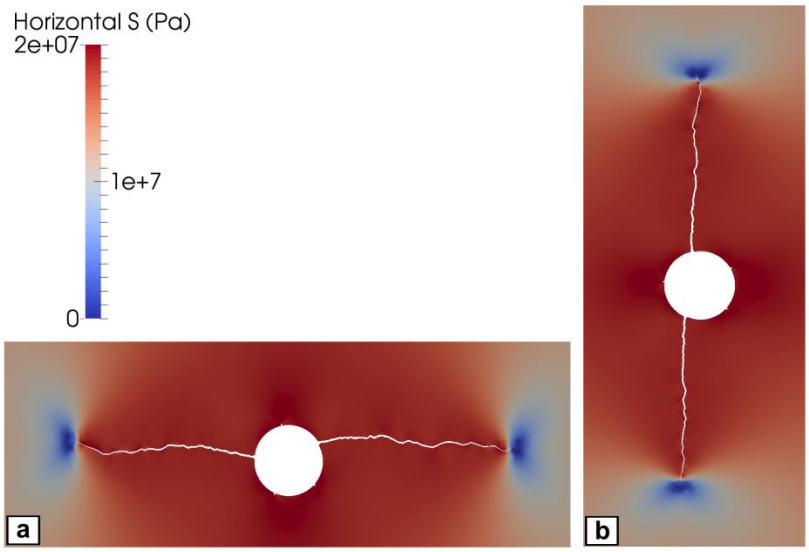

Figure 10: Fractures propagating from wellbore with reversed horizontal minimum stress direction, with stresses according to a compression positive convention: (a) in top-down direction; and, (b) in right-left direction, run on identically generated trigonal mesh, magnified at 50x displacement.

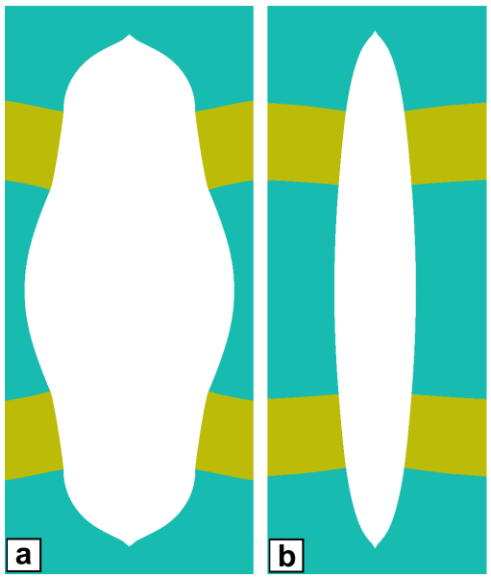

Figure 11: Vertical fracture response to Young's modulus: (a) high modulus contrast; and, (b) low contrast, magnified at 7000x displacement.

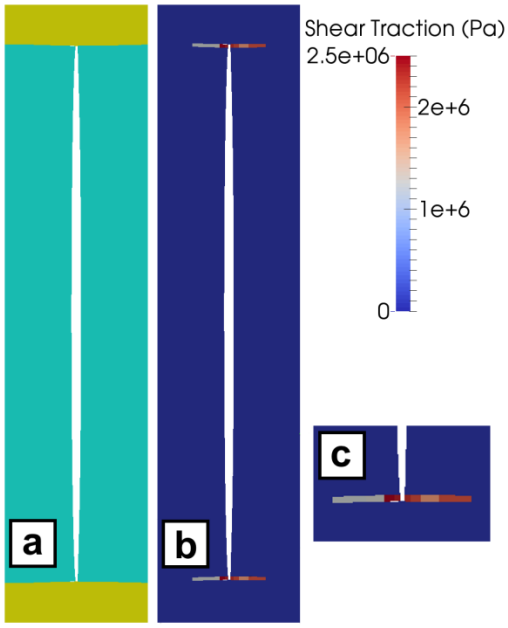

Figure 12: Vertical fracture encountering barriers: (a) schematic with barriers in yellow; (b) recorded effective shear initiation tractions; and (c) zoom view of tractions, magnified at 500x displacement.

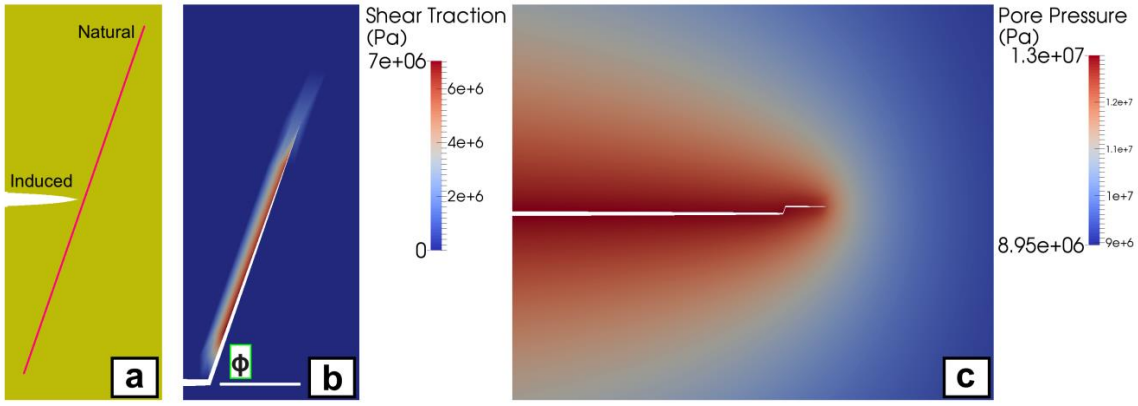

Figure 13: Fracture propagating horizontally towards a conformally meshed plane-of-weakness: (a) schematic; (b) forced-path development of cohesive zone along preexisting plane, in shear failure; and, (c) arbitrary fracture path through fracture showing pressure diffusion, magnified at 100x displacement.

This simulation describes fracture propagation from an open-hole wellbore with the net pressure (reducing to 0.2E+6 Pa), applied uniformly around the wellbore and the fracture. Slight discontinuities representing flaws are introduced around the 1.08 cm (0.425 in.) wellbore, otherwise a fracture initiates but propagates singly. The fracture propagation path for Fig. 10 is dominated by fracture face opening against the direction of the minimum principal stress for all steps simulated (Mode I), with propagation displayed to about 0.05 m length 80 um aperture. Fig. 10a shows fractures propagating out of flaws along the axis of minimum horizontal stress, in this case laterally. For the simulation shown in Fig. 10b, the direction of minimum horizontal stress is reversed.

In both simulations, as expected, increased compression develops in a region of wellbore and normal to the fracture, with a small tensile region ahead of fracture tips. Clearly the fracture path is primarily the result of the initial stress contrast, while the meshing regime produces local fracture path deviations. Mesh fining is employed to produce straighter trajectories, less impacted by mesh structure. Our results were similar to seeded random or otherwise polygonal meshes: symmetric dual fracture propagation from wellbore, and reduced local deviations along the fracture path (see similar results in [8]).

Vertical propagation

Our third model (Fig. 11 and 12) shows vertical fracture propagation, through layers with differing rock elastic properties, and fracture propagation towards a barrier layer. The fracture widths decrease during propagation through the higher elastic modulus rock. Shear failure events while encountering a barrier or otherwise failing in shear are recorded, allowing us to investigate potential microseismic events as the fracture propagates. The vertical fracture simulations shown here assume plane strain

behavior, and as such vertical propagation and fracture turning in the horizontal plane cannot be simultaneously modeled. It should be noted that the formulation and implementation of the model is in 3D and so is extensible to model the propagation of fractures in 3D.

The Young's modulus for the yellow (lighter colored) layers was held at 90E+9 Pa for all simulations run. The blue/green layers were assigned a modulus of 20E+9 Pa for Fig. 11a and of 70E+9 Pa for Fig. 11b. The rock permeability for all layers is 1E-12 m2. A fracture propagating in front of the hydraulically connected fracture was observable during the simulation that produced Fig. 11a. The difference in soft layer modulus produces a strong contrast in terms of aperture and fracture shape. Fractures in Fig. 11 have propagated to a length of 34 m, at an aperture of 1 mm and 0.4 mm for Fig. 11a and Fig. 11b respectively.

In Fig. 12 a fracture barrier case was run in order to showcase the impact of the failure mode. The fracture advances in Mode I failure until encountering a barrier. The barrier layer is characterized by a much higher normal critical stress and is, therefore, not penetrable, given fracture the propagation length, history, and net pressure distribution. A shear failure indicator field was recorded as: $\|\mathbf{t}_t^f\|$ for $\left\|\mathbf{t}_t^f\right\| > \|\mathbf{t}_n^f\|$, or otherwise zero. The fracture propagates to a length of 14 m and an end-time aperture of 0.250 mm, through rock with a critical normal effective stress of 0.1E+6 Pa and a permeability of 1E-12 m2, with end-time net pressure reducing to 0.2E+6 Pa. No tracking values were recorded during Mode I propagation (Fig. 12, up-down boundaries). As the fracture encounters a second layer with a critical normal effective stress of 6.7E+6 Pa or above, it is unable to penetrate the layer. The fracture is then diverted along the interface with fractures nucleating both in and out of hydraulic connection with the main fracture. The fracture tip remains in the cohesive zone, with extension out of Mode I/II regime

controlled by rock Young's modulus i.e. the extent of the available lateral compression. Similar shear traction events (as and if they occur) are recorded during all our simulations, e.g. for the isotropic critical stress simulation shown in Fig. 9d.

High angle intersection

The ability to capture slight kinking is a distinguishing feature of field-scale fracture modeling. Fig. 13 shows this type of complex fracture propagation. In particular the model exhibits responsiveness to: variations in tangential critical stresses (e.g., Fig. 9); development of shear failure at a barrier (Fig. 12); and, reductions in normal critical stress. To illustrate this effect, we model a high-angle intersection between an induced hydraulic and a preexisting natural fracture. The surface of the natural and induced fractures are both modeled as physically smooth. For this simulation, the parameters are as given in Table 5. The traction boundary condition was required to be per Eq. (37)a, in order to reduce the net pressure to the near minimum horizontal stress at the fracture tip.

This fracture in Fig. 13 propagates normally in Mode I failure for 7 m, until the cohesive tip intersects the natural fracture at a net pressure of 0.1E+06 Pa and an aperture of 0.4 mm. When intersection occurs, the connected fracture will propagate through, turn along the natural fracture path in Mode II failure (Fig. 13b), or kink and return to opening against the far-field minimum principal stress direction. This simulation shows that fracture paths depend upon several parameters. Given fixed material parameters and stress contrast, activation of the natural fracture in tensile failure becomes less likely as the intersection angle decreases from 90 to 0°. In Fig. 13c, the critical effective normal stress has been reduced to 1.25E+6 Pa and the fracture kinks to resume opening against the far-field minimum direction (c.f. [37]).

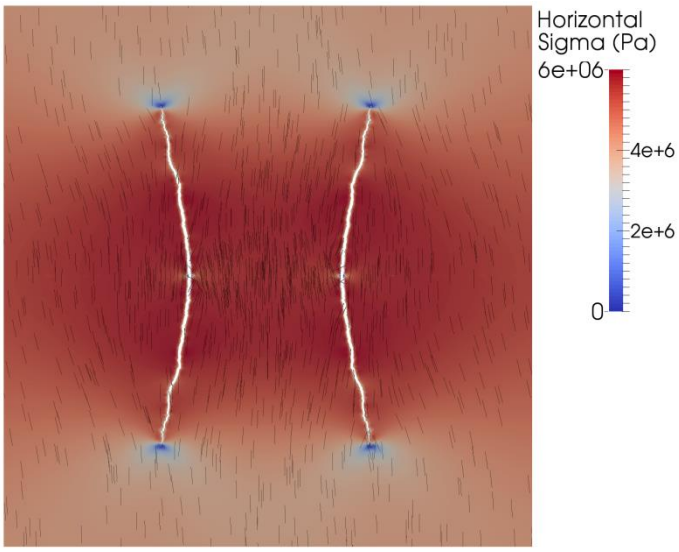

Figure 14: Fractures turning in response to stress interference effects, and propagating in direction of horizontal maximum stress (grayed line glyphs), magnified at 500x displacement.

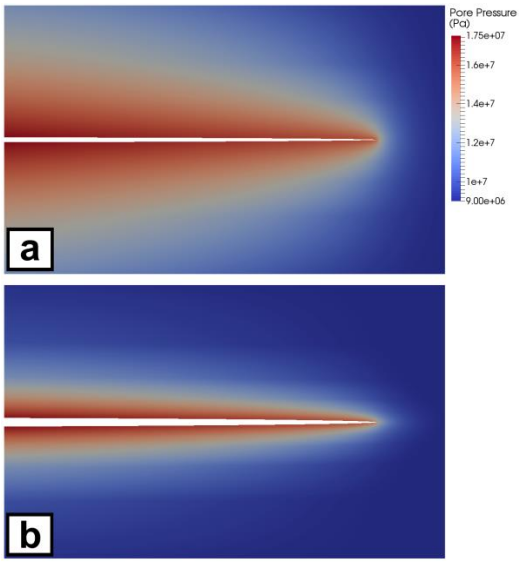

Figure 15: Parabolic near-fracture pore pressure distribution evolving with fracture pressure curve: (a) isotropic permeability; and, (b) reduced up-down directional permeability, magnified at 200x displacement.

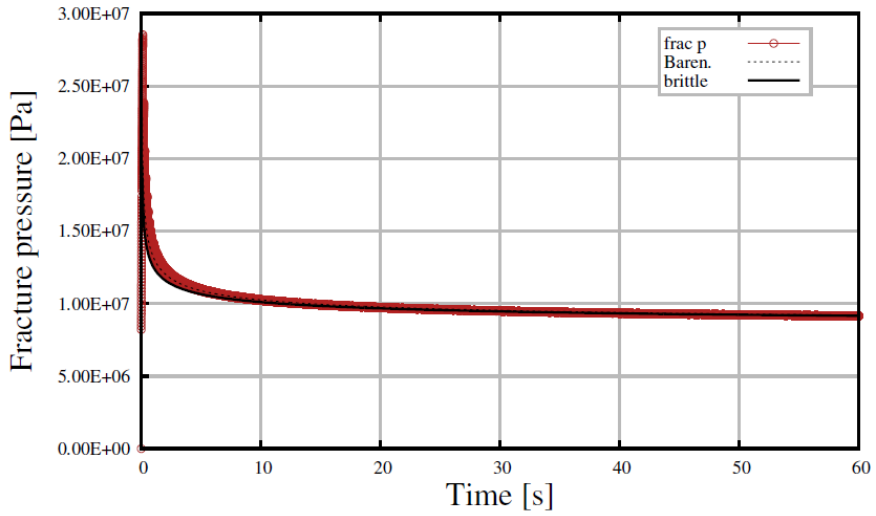

Figure 16: KGD geometry case for $(\sigma_n)_c$ = 1E+7 Pa, recovered fracturing pressures.

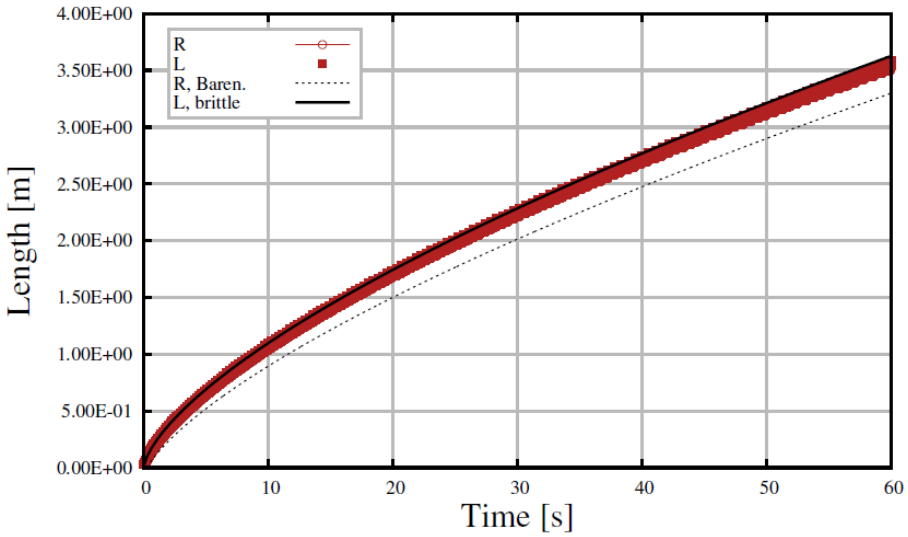

Figure 17: KGD geometry case for $(\sigma_n)_c$ = 1E+7 Pa, recovered length.

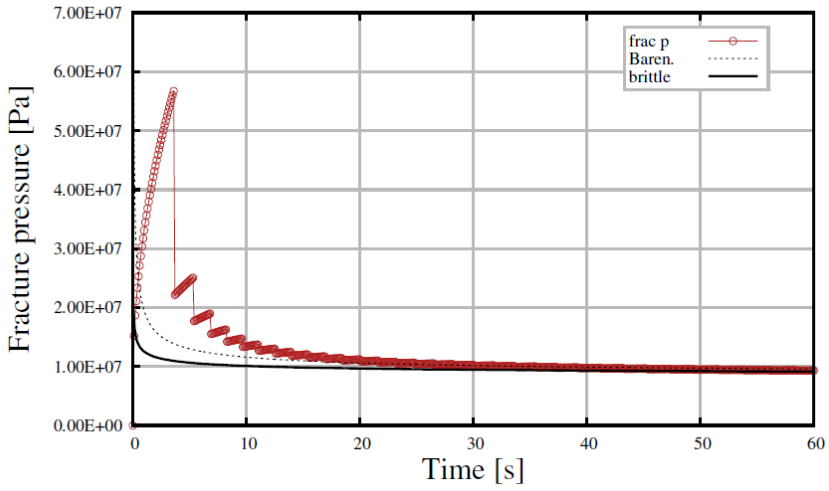

Figure 18: KGD geometry case for $(\sigma_n)_c$ = 1E+6 Pa, recovered fracturing pressures.

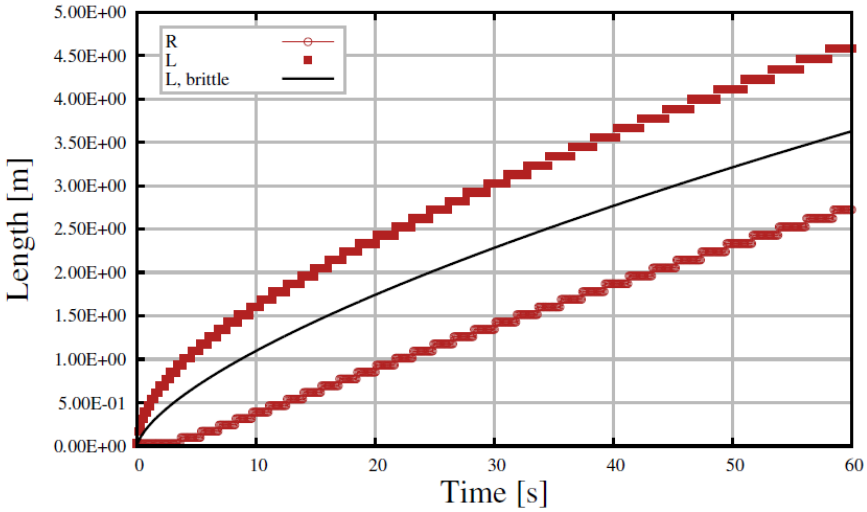

Figure 19: KGD geometry case for $(\sigma_n)_c$ = 1E+6 Pa, recovered length.

Stress shadow and poroelastic effects

Fig. 14 and 15 show models indicating stress interference effects during multiple fracture propagation, as well as pore pressure diffusion from the fracture based upon arbitrary fracture-interior pressure distributions. Stress interference effects typically occur when multiple, non-intersecting, competing fractures grow. Rival fractures incur stress interference effects within the fractures' stress shadow region. Simultaneous propagation of the rival fractures causes a distinctive propagation pattern: fractures curving away from the centerline as the fracture tip follows local changes in the maximum horizontal stress direction.

The width of fractures simulated (Fig. 14) is 0.3 mm at the aperture, with the perforations spaced 10 m apart, and normal and tangential critical the effective stresses of 0.5 and 1E+6 Pa respectively, at a fracture net pressure of 3.1E+6 Pa. Fig. 14 shows effective stress regions in tension in the vicinity of fracture tips, indicating that this region is experiencing tensile failure (by critical effective stress criterion, with stresses post-processed into a compression positive sign convention). A small disturbance in the stress field is noticeable near the perforation locations. This is associated with initialization of the residual stress tensor near discontinuities in the original discretization (unlike Fig. 10).

Fig. 15 shows a characteristic parabolic near-fracture pore pressure distribution, indicating intensification of leak-off pressures in the wake of the numerical fracture tip. Critical effective stresses are isotropic and increased to 1.25E+6 Pa, with an ultimate tip net pressure of 3.1E+6 Pa. Simulations differ in one respect only: permeability in the direction of far-field minimum stress is reduced from 1E-14 m2 in Fig. 15a to 1E-15 m2 in Fig. 15b. Fracture in Fig. 15a propagates to 1.5 mm width and 21 m length while the

fracture in Fig. 15a propagates to 2.0 mm width and 21 m length, and width reduction is associated with poroelastic effects (i.e. pressure continuity during leak-off).

Meshing-related error

Let us suppose a Mode I fracture, for which the assigned $G_{Ic} = 0$ and $(\sigma_n)_c \approx 0$. The model uses the above described CZ model. In this scenario, we expect unconstrained length growth with increasing mesh refinement at the fracture tip. To summarize, a zero toughness CZ model does not approach a mesh independent solution with regard to numerically recovered fracture dimensions. For an incompressible fluid with no leak-off, the fracture will maintain some non-zero width. Given that positive width, the fracture growth will simply be dictated by the elastic response of the material: hence, a stress singularity exists at the tip. If the mesh at the fracture tip is sufficiently fine, the resolved effects of the stress singularity will overcome the trivial tensile limit stress, plus any resolved far-field stress, resolve to the tip-adjacent FV cell face. Therefore an increase in fracture-tip mesh refinement decreases the size of the cell face, and hence radius from the singularity. As the radius diminishes, the net resolved effective stresses become more tensile. Thus refinement simply acts to extend the fracture tip, because the stress-effect of the singularity overcomes the (constant) far-field compression. As a corollary, for a fixed value of $(\sigma_n)_c$ under our methods, the near tip mesh refinement must increase with decreasing but non-zero G_{Ic} in order to maintain a cohesive zone; thus, the practical use of the CZ model is to limit fracture extension.

Therefore, to compare the fracture mechanics implementation to an analytic solution: toughness is assumed to be non-zero, and unaffected by in situ stress state. For this model, the fracture fluid is assumed to be inviscid and slightly compressible (small variations in fluid density), with a fixed injection rate at the inlet. Fig. 16 presents the

non-trivial toughness comparison for pressure; Fig. 17 presents the result for length, and as for above benchmarking simulations $b = 0$. Also, here $k_p \approx 0$ to induce no leak-off. A comparison is shown to the analytic solution of both LEFM and Barenblatt's CZ models [38]. For this case, the comparison to the LEFM solution is favorable. However, this result DOES NOT verify the correctness of surface energies during fracture turning. In fact, it has been attempted to highlight the numerical surface roughness of fractures during such re-orientation. Because the exposed rough surface is larger than a straight path along the center of the fracture, the recovered surface energy may change. Improved accommodation for small-angle turning (large radius of path curvature) is a second important consideration. These are known issues for numerical implementations using face/nodal release methods, and can be mitigated via near-tip dynamic remeshing methods [7, 39].

Near-tip fining requirements are quite restrictive; however, the mesh density requirements appear in-line with other field-scale models, in which a fracture surface is resolved (and the correct fracture energy recovered). E.g., such models include be peridynamics and phase-field crack growth models. Here the limit fining required for converging the stress-dependent, zero-toughness case to the analytic solution is a reasonable proxy. For instance, the required fining in the notation of peridynamics is $2a(\delta/2a)/m$, for: $2a$ the domain length dimension in the x_1-direction, $\delta/2a$ the horizon size per unit length, and m the neighbors in the horizon. In the case of peridynamics using a 2D KGD geometry, the matching fining is 0.1 m for a zero toughness simulation [40]. This compares to 0.018 m, for the Fig. 16 comparison where G_{Ic} is 120 J/m2.

For the CZ model, required fining reduces where $(\sigma_n)_c$ is reduced, see Fig. 18 for pressures and Fig. 19 for displacements. In these results, mesh refinement at the tip is limited to 0.07 m. However, the $(\sigma_n)_c$ reduction moves: (a) recovered "real fracture

length" (R) curve away from the brittle limit, and in the direction of Mokryakov's Barenblatt solution; and (b), total length (L, including the CZ) curve away from the brittle limit, and away from the direction of Mokryakov's solution. Therefore, the modeled location of the fracture tip becomes increasingly diffuse with decreasing $(\sigma_n)_c$; thus, where in situ stress effects are removed from the model, this effect indicates the physical interpretation of the stress parameters.

CONCLUSIONS

This work describes the development of a finite volume, cohesive zone, fracture propagation model. The method uses an iteratively coupled linearized poromechanics formulation. Our methods for solution of the displacement equation are adapted from the proven numerical solid mechanics suite developed and made available by Jasak, Tuković, and co-workers. This paper describes the appropriate means for coupling such a poroelastic-based model with fracture propagation methods based on a cohesive zone formulation. To the best of our knowledge, this paper details a poroelastic CZ model/FV method fracture growth model for the first time. The simulation model has been shown to be capable of simulating the propagation of multiple, non-planar fractures in heterogeneous porous media.

Fracture propagation in heterogeneous media can lead to complex fracture patterns and propagation behavior. To demonstrate the capabilities of the model some interesting cases are simulated, with an emphasis on presenting behaviors important to various applications in the oil industry. It is shown that fracture paths varied systematically. The fracture paths varied in response to changes in rock energy model characteristics such as normal and tangential critical effective stresses. The simulated fracture paths responded to heterogeneity by turning along the direction of planes-of-

weakness. Fracture propagation has been shown to depend on the local stress state, both in terms of degree and principal direction of anisotropy of the initialized stress tensor. Shear failure events can be mapped as the fracture propagates. Propagation through vertical layers was modeled, as was pressure diffusion into the formation. Our fracturing simulation can accept an arbitrarily variable fracture fluid pressure distribution.

In addition to the examples detailed, this model offers an opportunity to implement other important features. While not discussed here, the method is amenable to: (a) extensibility to model truly 3D problems, as the dominant finite volume-based solid mechanics libraries are inherently fully 3D; (b) feasible domain decomposition for processor-based parallelization of simulations, which is enabled by the use of shared FV data structures when solving displacement and pressure field equations; and, (c) adaptive mesh refinement using these shared data structures, in order to model 3D problems with reasonable run times.

Chapter 2: Application of finite volume-based bimaterial method to variously coupled poroelasticity

The development of hydromechanically-coupled displacement and flow equations, for the modeling of homogeneous poroelastic "bi-continuum" domains, is extensively covered in classic literature [19]. However, the domains we are now interested in modeling may include: a pore fluid flow continuum, with different initial pore pressures in various rock layers; several solid skeletal material, with spatially varying elastic material and softening parameters, as well as Biot's coefficient, porosity, and intrinsic permeability; a vertically varying residual stress state, often referred to in the completions literature as the "far-field" stress; and, impermeable barriers. The result of the enhanced stress analysis can provide a basis for: 3D modeling of the stress state at horizontal interfaces of vertically stacked, heterogeneous rock layers; or, evaluation of the rock stress state within near-wellbore region in the vicinity of a perforated steel casing with cement.

For instance, modeling of cased, cemented wellbores is necessarily a multi-material problem, as the steel casing is impermeable and has a much higher Young's modulus than the surrounding cement and rock formation. Hence, our motivation is to describe correctly the gradient of displacement and hence stress state along such interfaces. Any such efforts require accurate FV method-based stress analysis, such that all geomechanical parameters (including Biot's coefficient) can be varied across a multi-material interface (and hence model steel and rock on the same numerical mesh). Relevant practical applications for this work would include simulation of hydraulic fractures in the near-wellbore region, using the displacement-driven crack propagation previously applied to elastic materials [30].

In essence, this work presents methods that purely superimpose hydromechanical coupling terms with FV-based bimaterial stress analysis. Examples of the fixed-strain and fixed-stress iterative poroelastic couplings are presented [22, 41]. The over-relaxed solution approach to FV-discretized elasticity [15], as well as coupled poroelasticity [20], is utilized; numerical handling of multi-material domains (cf. [11]) is extended to poroelasticity and use of an initialized, residual stress tensor. Some extra attention is given to stress state initialization as well as boundary conditions – being useful in the application of multi-material geomechanical models. Verification of the numerical models is presented, firstly by standard Terzaghi's and Mandel's problems. Secondly the plane-strain analysis of an Eshelby's inclusion is extended slightly, to include effects of poroelasticity using a spatially varying initialized residual stress tensor [42, 43].

In essence, this work presents methods that purely superimpose hydromechanical coupling terms with FV-based bimaterial stress analysis. Examples of the fixed-strain and fixed-stress iterative poroelastic couplings are presented [22, 41]. The over-relaxed solution approach to FV-discretized elasticity [15], as well as coupled poroelasticity [20], is utilized; numerical handling of multi-material domains (cf. [11]) is extended to poroelasticity and use of an initialized, residual stress tensor. Some extra attention is given to stress state initialization as well as boundary conditions – being useful in the application of multi-material geomechanical models. Verification of the numerical models is presented, firstly by standard Terzaghi's and Mandel's problems. Secondly the plane-strain analysis of an Eshelby's inclusion is extended slightly, to include effects of poroelasticity using a spatially varying initialized residual stress tensor [42, 43].

INTERFACES

Methods are outlined that solve the momentum equation of linearized poroelasticity. Special treatment is provided at bimaterial interfaces, e.g. where the Young's modulus jumps across a steel/concrete interface. Continuity of the displacement gradient is not assumed, in order to resolve a more accurate stress state. Instead, the continuity of traction and solid skeletal displacement is enforced. Where both materials are permeable, the continuity of pore pressure and pore fluid relative velocities is also enforced.

Open pore interfaces

At permeable bimaterial poroelastic interfaces, we assume open pore continuity of both total traction and pore pressure, as per [27]. The notation is that the interface i exists between any two (including two identical) materials a and b. Normal vector $\mathbf{n}_i$ describes the orientation of the interface. Subscripts ia indicates the current side of the interface. Subscript ib indicates the far side of the interface. The continuity conditions are expressed as by [47],

$$\mathbf{t}^{\mathbf{S}}_{ia} = \mathbf{n}_i \cdot \mathbf{S}_{ia} = \mathbf{n}_i \cdot \mathbf{S}_{ib} = \mathbf{t}^{\mathbf{S}}_{ib}, \quad (40)$$

$$\mathbf{v}_{ia} = \frac{\partial(\mathbf{u}_{ia})}{\partial t} = \frac{\partial(\mathbf{u}_{ib})}{\partial t} = \mathbf{v}_{ib}, \quad (41)$$

$$p_{ia} = p_{ib}, \quad (42)$$

$$\mathbf{n}_i \cdot \mathbf{w}_{ia} = \mathbf{n}_i \cdot \mathbf{w}_{ib}, \quad (43)$$

where traction is $\mathbf{t}^{\mathbf{S}}$, pore pressure pressure p, solid skeletal velocity $\mathbf{v}$ (as the temporal derivative of rock skeleton's displacement, $\mathbf{u}$), and pore fluid relative velocity $\mathbf{w}$. Eq. (40) is usefully re-stated as the continuity conditions for normal ($\mathbf{t}^{\mathbf{S}}_n$) and tangential ($\mathbf{t}^{\mathbf{S}}_t$) components of traction,

$$(\mathbf{t}_n^{\mathbf{S}})_{ia} = \mathbf{n}_i\mathbf{n}_i \cdot (\mathbf{n}_i \cdot \mathbf{S}_{ia}) = \mathbf{n}_i\mathbf{n}_i \cdot (\mathbf{n}_i \cdot \mathbf{S}_{ib}) = (\mathbf{t}_n^{\mathbf{S}})_{ib}, \quad (44)$$

$$(\mathbf{t}_t^{\mathbf{S}})_{ia} = (\mathbf{I} - \mathbf{n}_i\mathbf{n}_i) \cdot (\mathbf{n}_i \cdot \mathbf{S}_{ia}) = (\mathbf{I} - \mathbf{n}_i\mathbf{n}_i) \cdot (\mathbf{n}_i \cdot \mathbf{S}_{ib}) = (\mathbf{t}_t^{\mathbf{S}})_{ib}, \quad (45)$$

where consistently subscript n is used to refer to the normal component of a vector; subscript t represents the tangential component.

The time-integrated effect of Eq. (41) is to impose the continuity of skeletal interface displacements from any reference configuration wherein the initial displacements are equal at an internal boundary. The exceptional case would be where an explicit discontinuity is introduced into a domain, such as within softening regions during fracture propagation. Various methods for enforcing Eq. (43) are important but not considered here. Overall, distance-weighed harmonic averaging of permeability is considered sufficient for geomechanical analysis at open pore interfaces.

Closed pore and impermeable interfaces

For the numerical treatment presented, the classes of closed pore and impermeable interfaces are lumped together. Closed pore interfaces are such that the pore spaces of materials a and b are disconnected along the interface. Impermeable interfaces are considered be an interface where one or both of the materials is impermeable. Continuity conditions are restated for closed pore and impermeable interfaces as:

$$\mathbf{t}_{ia}^{\mathbf{S}} = \mathbf{n}_i \cdot \mathbf{S}_{ia} = \mathbf{n}_i \cdot \mathbf{S}_{ib} = \mathbf{t}_{ib}^{\mathbf{S}}, \quad (46)$$

$$\mathbf{v}_{ia} = \frac{\partial(\mathbf{u}_{ia})}{\partial t} = \frac{\partial(\mathbf{u}_{ib})}{\partial t} = \mathbf{v}_{ib}, \quad (47)$$

$$p_{ia} = p_{ib} \leftrightarrow p_a = p_b, \quad (48)$$

$$\mathbf{n}_i \cdot \mathbf{w}_{ia} = 0 \text{ and } \mathbf{n}_i \cdot \mathbf{w}_{ib} = 0, \quad (49)$$

where: $p_a = 0$, if material a is not poroelastic; and, $p_b = 0$ if material b is not poroelastic (i.e. b is elastic). Eq. (48) indicates that, at both closed pore and impermeable

interfaces, the pressure is properly discontinuous across the interface. Eq. (49) indicates that the interface is a no-flow internal boundary.

PORE FLUID FLOW

The poroelastic coupling known as the "$\mathbf{u} - p$ approximation" reduced for quasi-static phenomena is in essence employed. We thus omit from the coupled equations terms related to fluid relative acceleration, as well as a dynamic term representing the acceleration of the bulk solid. For an arbitrary volume V with surface S, the isothermal hydromechanically-coupled single phase flow equation is:

$$\int_V [\frac{1}{M}\frac{\partial p}{\partial t} + b\frac{\partial(\nabla \cdot \mathbf{u})}{\partial t}]\mathrm{d}V = \oint_S \mathbf{n} \cdot (\frac{k_p}{\mu_p}\nabla p)\mathrm{d}S, \quad (50)$$

where gravitational effects have been omitted and the Darcy constitutive relation substituted to adduce flux from gradient. Although the above equation is a single-phase poroelastic equation, a representative coupling pressure field may also be developed from a hydromechanically-coupled multi-phase flow formulation. Biot's modulus M and Biot-Willis coefficient b are constantly valued under the (small strain) linearized poroelastic coupling, and defined as:

$$\frac{1}{M} = \frac{1}{N} + \frac{\phi^0}{K_p} = \frac{b - \phi^0}{K_s} + \frac{\phi^0}{K_p}, \quad (51)$$

$$b = 1 - \frac{K_d}{K_s}. \quad (52)$$

The pore fluid flow equation is linearized by the assumption,

$$|\frac{\rho_p - \rho_p^0}{\rho_p^0}| \ll 1, \quad (53)$$

where the above equation indicates small variations in pore fluid density, ρ_p.

LINEARIZED POROELASTICITY

From first principles, at quasi-static equilibrium alterations in the current state of total stress are unaffected by changes in the bulk acceleration term. The isothermal inertial balance is combined with the effective stress definition of linearized poroelasticity to describe the divergence of total stress, without gravity or other body forces. Thus the quasi-static balance $\mathbf{0} = \nabla \cdot \mathbf{S}$ using the poroelastic definition of total stress $\mathbf{S} = \boldsymbol{\sigma} - bp\mathbf{I}$ (TENSION POSITIVE) is developed into:

$$\mathbf{0} = \oint_S \mathbf{n} \cdot (\boldsymbol{\sigma} - bp\mathbf{I}) \mathrm{d}S. \quad (54)$$

A small strain constitutive relation is employed and returns the strain as:

$$\boldsymbol{\varepsilon} = \frac{1}{2}[\nabla\mathbf{u} + (\nabla\mathbf{u})^{\mathrm{T}}], \quad (55)$$

where $\mathbf{u}$ is defined with respect to a reference configuration. In order to account for the far-field stress state ($\mathbf{S}^0$) and pore pressures before any treatment or depletion (p^0), the concept of a residual effective stress state is employed. Viz., the residual effective stress $\boldsymbol{\sigma}^0$ is calculated from values read-in during initialization – and may vary e.g. with depth. Thus the above equation is combined with Hooke's law to obtain the current increment of effective stress $\boldsymbol{\sigma} - \boldsymbol{\sigma}^0$ from the displacement field. Hence:

$$\boldsymbol{\sigma}^0 = \mathbf{S}^0 + bp^0\mathbf{I}, \quad (56)$$

$$\boldsymbol{\sigma} - \boldsymbol{\sigma}^0 = \mu[\nabla\mathbf{u} + (\nabla\mathbf{u})^{\mathrm{T}}] + \lambda \mathrm{tr}(\nabla\mathbf{u})\mathbf{I}, \quad (57)$$

and hence $\boldsymbol{\sigma}^0$ captures the stress state for a uniformly zero displacement field. The poroelastic total stress is then,

$$\begin{aligned}\mathbf{S} &= \boldsymbol{\sigma} - bp\mathbf{I} = (\boldsymbol{\sigma} - \boldsymbol{\sigma}^0) + \boldsymbol{\sigma}^0 - bp\mathbf{I}, \\ &= \mu[\nabla\mathbf{u} + (\nabla\mathbf{u})^{\mathrm{T}}] + \lambda\mathrm{tr}(\nabla\mathbf{u})\mathbf{I} + \boldsymbol{\sigma}^0 - bp\mathbf{I}. \quad (58)\end{aligned}$$

Restating our momentum balance of Eq. (54) - with substitution of constitutive relation Eq. (58) and use of the divergence theorem - obtains:

$$\int_V [\nabla \cdot (bp\mathbf{I}) - \nabla \cdot \boldsymbol{\sigma}^0]\mathrm{d}V = \oint_S \mathbf{n} \cdot (\mu[\nabla\mathbf{u} + (\nabla\mathbf{u})^{\mathrm{T}}] + \lambda\mathrm{tr}(\nabla\mathbf{u})\mathbf{I})\mathrm{d}S\,. \quad (59)$$

Our linearization is small strain and considers only an isotropic strain tensor, as per Eq. (55). Therefore as a limit on applicability, the volumes of any discretized cells and their surface normals are subject to:

$$\left|\frac{V - V^0}{V^0}\right| \ll 1, \qquad \mathbf{n} \cdot \mathbf{n}^0 \approx 1. \quad (60)$$

where these assumptions are encoded into the semi-discretized equations, e.g. later Eq. (76).

Traction decompositions

The right-hand side term of Eq. (59) is the incremental component of resolved effective stress vector ($\mathbf{t}_{\boldsymbol{\sigma}-\boldsymbol{\sigma}^0}$), across surface defined by unit vector $\mathbf{n}$. This reduced decomposition of the traction is defined for convenience and depends only on the parameters and the current gradient of displacement. The resolved effective stress ($\mathbf{t}_{\boldsymbol{\sigma}}$) additionally contains the contribution of the stored residual stress state at initialization. The traction vector is defined as the product of the unit normal vector $\mathbf{n}$ and the total stress tensor. These are,

$$\mathbf{t}_{\boldsymbol{\sigma}-\boldsymbol{\sigma}^0} = \mathbf{n}\cdot(\boldsymbol{\sigma}-\boldsymbol{\sigma}^0) = \mu\mathbf{n}\cdot\nabla u + \mu\nabla\mathbf{u}\cdot\mathbf{n} + \lambda\mathrm{tr}(\nabla\mathbf{u})\mathbf{n}, \quad (61)$$

$$\mathbf{t}_{\boldsymbol{\sigma}} = \mathbf{t}_{\boldsymbol{\sigma}-\boldsymbol{\sigma}^0} + \mathbf{n}\cdot\boldsymbol{\sigma}^0, \quad (62)$$

$$\mathbf{t}_{\mathbf{S}} = \mathbf{n}\cdot\mathbf{S} = \mathbf{t}_{\boldsymbol{\sigma}} - bp\mathbf{n} = \mathbf{t}_{\boldsymbol{\sigma}-\boldsymbol{\sigma}^0} + \mathbf{n}\cdot\boldsymbol{\sigma}^0 - bp\mathbf{n}, \quad (63)$$

where Eq. (61) define the incremental component of the resolved effective stress vector, with respect to an initial reference state.

Use of a tangential gradient operator decomposes the displacement gradient, by removing the component of that tensor normal to unit vector n. The normal component of traction is vector $\mathbf{t}_n^{\mathbf{S}}$; and, the tangential component is $\mathbf{t}_t^{\mathbf{S}}$:

$$\mathbf{t}_n^{\mathbf{S}} = (2\mu+\lambda)\mathbf{n}\cdot\nabla\mathbf{u}_n + \lambda\mathbf{n}\mathrm{tr}(\nabla_t\mathbf{u}_t) + \mathbf{n}\mathbf{n}\cdot(\mathbf{n}\cdot\boldsymbol{\sigma}^0) - bp\mathbf{n}, \quad (64)$$

$$\mathbf{t}_t^{\mathbf{S}} = \mu\mathbf{n}\cdot\nabla\mathbf{u}_t + \mu\nabla_t u_n + (\mathbf{I}-nn)\cdot(\mathbf{n}\cdot\sigma^0), \quad (65)$$

$$\nabla_t = (\mathbf{I}-\mathbf{n}\mathbf{n})\cdot\nabla \quad (66)$$

where the tangential gradient operator ∇_t is introduced [11] for FV-discretized solid mechanics, but appears with applications explained in [48]. Eq. (64) contains the observation that pore pressure acts entirely in the direction normal to surfaces. Accordingly, the tangential components of all traction decompositions exclude any pore pressure field term. By summation of Eqs. (64) and (65), the traction vector may be recovered,

$$\mathbf{t}_{\mathbf{S}} = (2\mu+\lambda)\mathbf{n}\cdot\nabla\mathbf{u} - (\mu+\lambda)\mathbf{n}\cdot\nabla\mathbf{u}_t + \mu\nabla_t u_n + \lambda\mathbf{n}\mathrm{tr}(\nabla_t\mathbf{u}_t) + \mathbf{n}\cdot\boldsymbol{\sigma}^0 - bp\mathbf{n}. \quad (67)$$

This vector is the internal interface condition provided to the numerical implementation of Eq. (59), in order to enforce above listed continuity of the resolved stress.

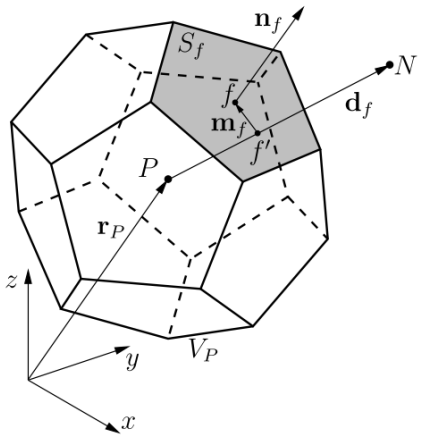

Figure 20: Control volume representing a polyhedral FV cell with cell center located at centroid P having volume V_P, showing in gray face with center located at point f having surface area S_f and face normal $\mathbf{n}_f$. Cell center located at P joined to centroid of cross-face neighbor N by vector $\mathbf{d}_f$ (from [11]).

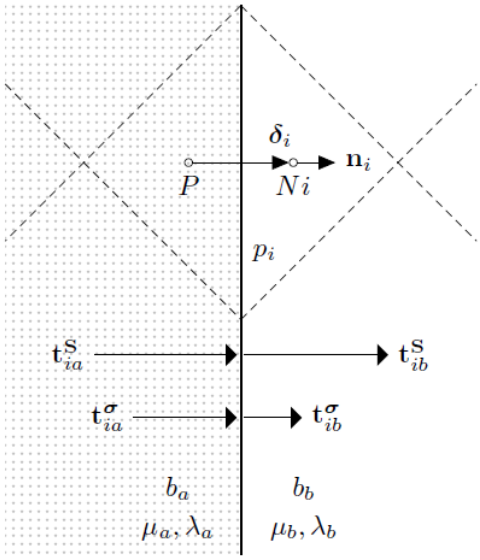

Figure 21: Open-pore interface of two finite volume cells on either side of the internal boundary of materials a and b. Cell under current consideration is centered at point P, and properties at current cell-side interface labeled with subscript ia. Neighboring cell is centered at point N_i, and properties at neighbor-side interface labeled with subscript ib (after [47, 11]).

Resolved effective stress

Various decompositions of the resolved effective stresses may be desirable as a post-processing step of the poroelastic coupling – i.e. to model fracture growth. If desired, the effective traction vector field ($\mathbf{t}_{\boldsymbol{\sigma}}$) is evaluated using a modified version of Eqs. (61) and (62) within material parameter-constant subdomains to produce the failure traction field. The failure field of tractions is therefore:

$$\mathbf{t}_f = \mathbf{n} \cdot (\mathbf{S} + b^f p\mathbf{I}) = \mathbf{t}_{\boldsymbol{\sigma}-\boldsymbol{\sigma}^0} + \mathbf{n} \cdot \boldsymbol{\sigma}^0 + (b^f - b)p\mathbf{n}, \quad (68)$$

where $\mathbf{t}_f$ is the field of e.g. cohesive zone initiation tractions, and as above b^f is not necessarily b; further the values of p must be appropriately interpolated or extrapolated to surfaces. Therefore, while coefficient b is spatially variable, b^f is considered to be selectable to implement the desired physics for all cases considered; for $b^f = 1$ the field $\mathbf{t}_f$ reduces to the resolved Terzaghi effective stress.

Interface resolved effective stress

While total traction across the interface will be well defined by Eq. (67) and is continuous, in a poroelastic medium the failure behavior is dictated by the effective stress state – which is often discontinuous. Thus to evaluate interface softening behavior, a representative resolved effective stress is defined as,

$$\mathbf{t}_i^f = \mathbf{t}_i^{\mathbf{S}} + \bar{b}_i^f p_i \mathbf{n}_i. \quad (69)$$

In forming $\mathbf{t}_i^f$, $\mathbf{t}_i^{\mathbf{S}}$ is simply over-written using the result of Eq. (67) – parenthetically, to be expressed in semi-discretized form as Eq. (100). So, in order to determine softening initiation, we provide the interface effective traction $\mathbf{t}_i^f$ with the most positive pore pressure contribution. The most positive contribution $\bar{b}_i^f p_i$ is:

$$\bar{b}_i^f p_i = \begin{cases} \max(b_{ia}^f p_{ia}, b_{ib}^f p_{ib}) & \text{if } a, b, \text{ or interface is impermable,} \\ \max(b_{ia}^f, b_{ib}^f) p_i & \text{if } a \text{ and } b \text{ and interface are peremable.} \end{cases} \quad (70)$$

(Alternate variants of Eq. (70) may be feasible, as representing continuity assumptions applied at the boundary. However here, such equations are written as prove workably consistent with effective stress-based cohesive initiation tractions and traction-separation laws.) Thus the above equation contains the following two observations. First, for any non-zero pore pressure field, the continuity of total traction over an interface with variable Biot's coefficient on either side, implies a discontinuity in the resolved effective stresses $\mathbf{t}_{ia}^f$ and $\mathbf{t}_{ib}^f$. Second, maximization of the resolved effective stresses at internal cell-to-cell faces is our criterion for the initiation of softening behaviors and hence to model fractures.

Porosity

Coupled Eq. (50) and (59) do not indicate that porosity or fluid density values are considered invariant under this model. As such, the porosity is not fixed, nor is the fluid incompressible; rather, a set of substitutions made during the coupling's formulation eliminate the requirement for explicit porosity or density updates. As such, the model does not require explicit computation of porosity change $\phi - \phi^0$ to solve the linearized poroelastic system.

In general, the current increment of porosity may anytime be recovered by recourse to:

$$\phi - \phi^0 = b(\nabla \cdot \mathbf{u}) - (\frac{1}{M} - \frac{\phi^0}{K_p})(p - p^0). \quad (71)$$

The incremental porosity expression follows directly from the definition of b and $1/N$ as poroelastic tangent properties [19]. Nevertheless, it is also useful to define the quantity ϕ^*, such that

$$\phi^* = \phi - \frac{\phi^0}{K_p}(p - p^0), \quad (72)$$

where ϕ^* is the variation in fluid mass content normalized by density. Per coupling assumptions, the model assumes the hypotheses of small variations in Lagrangian porosity,

$$\left|\frac{\phi - \phi^0}{\phi^0}\right| \quad \ll \quad 1. \quad (73)$$

Specifically the initialized porosity ϕ^0 is the reservoir porosity at which current pressures are invariant from initial pressure field p^0, for an initial state of zero displacement with respect to reference stress and configuration ($\mathbf{u} = \mathbf{0}$ and thus $\nabla \cdot \mathbf{u} = 0$). Zero displacement is presumed to be the in situ state, being that geological strains are converted to residual stresses during initialization step.

PORE FLOW DISCRETIZATION

See Fig. 20 for a full description of properties associated with the arbitrary polyhedral FV-method cell of size V_P. The total surface S_P of any such control volume may be discretized according to the summation of all continuum-material internal faces S_f, heterogeneous material interface faces S_i, and boundary faces S_b,

$$S_P = \partial V_P = \sum_f S_f + \sum_i S_i + \sum_b S_b, \quad (74)$$

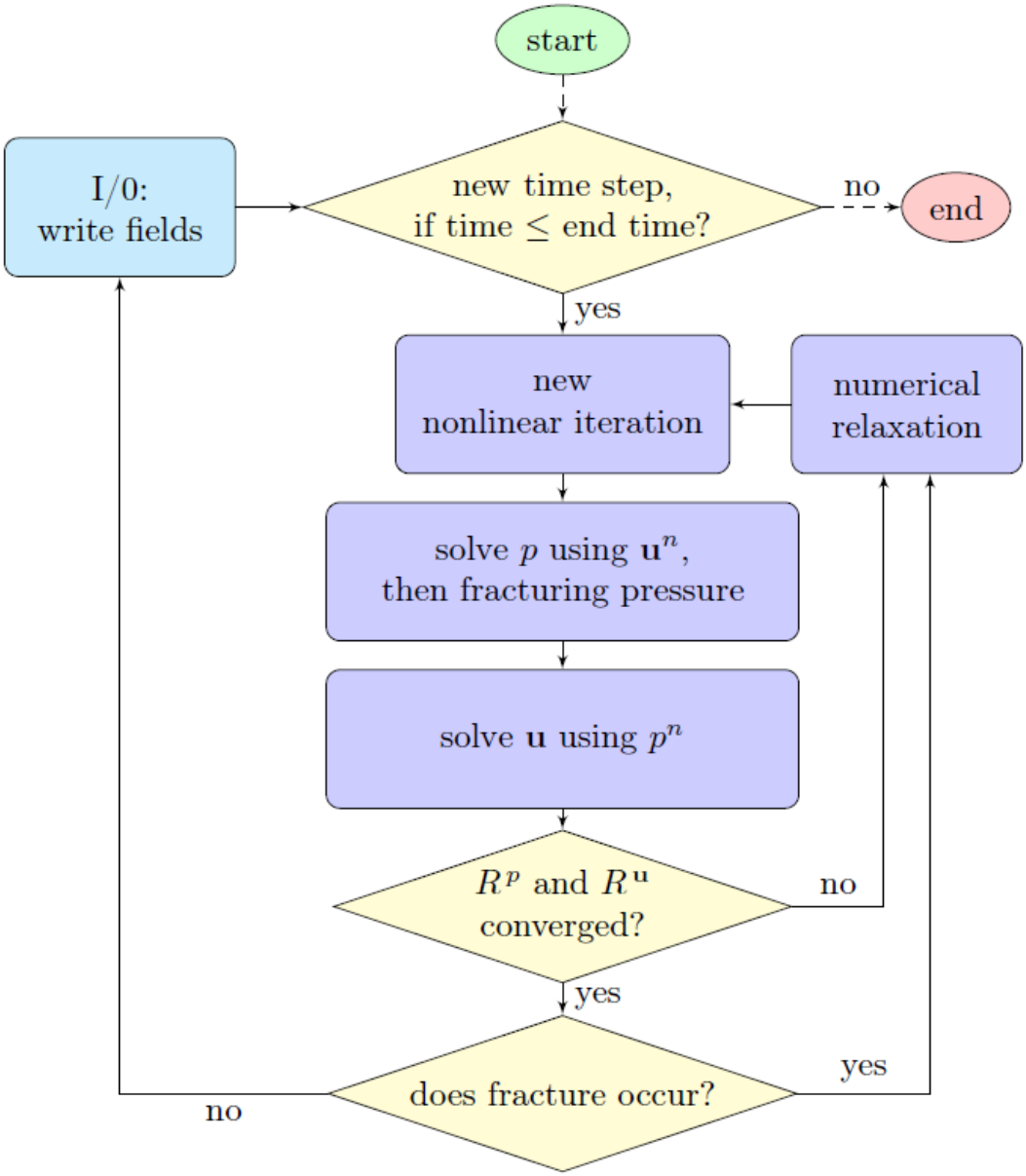

Figure 22: Flow chart of fixed-strain solver logic.

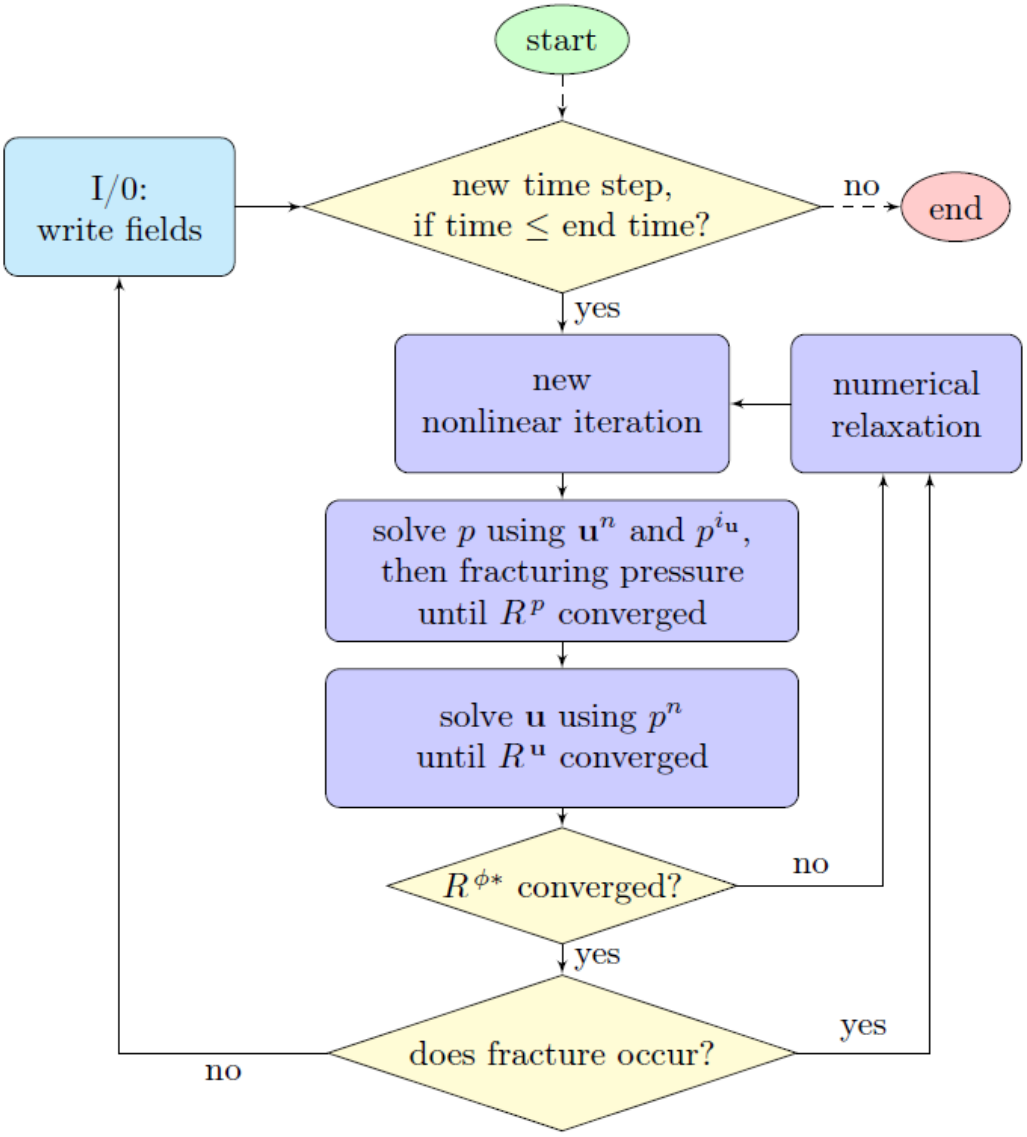

Figure 23: Flow chart of fixed-stress solver logic.

where the subscript f represents a material-continuum internal face, i is an interface face, and b a boundary face. The discretized interface for open pore continuity with a discontinuous Biot's coefficient is presented in Fig. 21.

Coupling splits

In this work, the interface-corrective method to enforce open pore continuity Eqs. (40 - 43) or closed pore Eqs. (46 - 49) is indifferent to the form of the iterative $\mathbf{u} - p$ coupling employed. We assume only: (a) an iterative coupling of the pressure and displacement partial differential equations, converged to a residual or residuals using the FV method; and, (b) that consequently, the pressure field equation is correctly solved within the coupling iteration, and prior to the displacement field equation. To define the implicit component of the pore fluid spatial equation discretization, let us define the term:

$$\mathcal{L}(p) \equiv \sum_{f} (\mathbf{n} \cdot \frac{k_p}{\mu_p} \nabla p)_f S_f + \sum_{i} (\mathbf{n} \cdot \frac{\bar{k}_p}{\mu_p} \nabla p)_i S_i + \sum_{b} (\mathbf{n} \cdot \frac{k_p}{\mu_p} \nabla p)_b S_b \,, \quad (75)$$

where $\mathcal{L}(p)$ is a convenience term. The permeability $\bar{k}_p$ is an averaged value which may be zero for closed and impermeable interfaces, as below. The permeability may also be expressed by replacing k_p with $\mathbf{K}_p$, where the latter is a symmetric positive definite tensor.

Fixed-strain split

For a fixed-strain split poroelastic coupling, the discretization of the pore pressure inside our flow equation is:

$$\mathcal{L}(p^n) = [\frac{1}{M} \frac{p_P^n - p_P^o}{\Delta t} + b \frac{(\nabla \cdot \mathbf{u})_P^n - (\nabla \cdot \mathbf{u})_P^o}{\Delta t}] V_P. \quad (76)$$

where subscript P represents cell-center values. Superscripts n, o, and oo represent the current t^n, previous t^o, and previous to previous t^{oo} time instances. The fixed-strain split has previously been extended to poro-elasto-plasticity [20]. Convergence of the pressure equation (including linear solver iterations and non-orthogonality correction) is measured by residual R^p. A flow chart presenting tightly iteratively coupled convergence is presented in Fig. 22.

Fixed-stress split

For a fixed-stress split poroelastic coupling, stability and convergence properties have been investigated previously [22, 41]. In essence, the mean stress is held constant during the coupling half-step. The discretization of the pore pressure inside our flow equation is:

$$\begin{aligned}\mathcal{L}(p_P^n) \quad = \quad & [(\frac{1}{M}+\frac{b^2}{\lambda})(\frac{p_P^n - p_P^o}{\Delta t}) + b\frac{(\nabla\cdot\mathbf{u})_P^n - (\nabla\cdot\mathbf{u})_P^o}{\Delta t}]V_P \\ & -[\frac{b^2}{\lambda}(\frac{p_P^{i_\mathbf{u}} - p_P^o}{\Delta t})]V_P, \end{aligned} \tag{77}$$

where b^2/λ is a constant related to the domain properties. This method improves the approximation within the pressure equation of poroelastic effects, and as such that constant may vary based upon constraints and compatibility of the problem. For all examples presented where a fixed-stress split is used, then exactly $b^2/\lambda = b^2/\lambda$ was used in our results. Superscript $i_\mathbf{u}$ indicates the immediately prior coupling iteration within the same time step, in which the displacement was fully converged.

Convergence of the pressure equation is measured by residual R^p. However, as momentum and flow equations are not simultaneously converged, a residual describing the coupling must be formed. This residual is,

$$R^{\phi*} = \max\left|\frac{[b(\nabla\cdot\mathbf{u})]^n - [\frac{b^2}{\lambda}]([p]^n - [p]^0)}{[\phi^*]^n}\right|, \quad (78)$$

where the residual definition follows the approach of [46], and where "[]" brackets indicate terms arranged in the solution vector order. A flow chart presenting convergence to $R^{\phi*}$ is presented in Fig. 23.

Explicit fixed-stress

The solution approach for a fixed-stress-split, explicit-in-time coupling has been discussed previously e.g. [49]. The time derivative of volumetric strain (as divergence of displacement relative to reference configuration) is resolved as an explicit term plus a function of the pore pressure in the present iteration,

$$\begin{aligned}\frac{\partial(\nabla\cdot\mathbf{u})^n}{\partial t} &\approx \frac{\partial(\nabla\cdot\mathbf{u})^o}{\partial t} + \frac{b}{K_d^*}\frac{\partial(p^n - p^o)}{\partial t}, \\ &= \frac{(\nabla\cdot\mathbf{u})_P^o - (\nabla\cdot\mathbf{u})_P^{oo}}{\Delta t} + \frac{b}{\lambda}\left[\left(\frac{p_P^n - p_P^o}{\Delta t}\right) - \left(\frac{p_P^o - p_P^{oo}}{\Delta t}\right)\right]. \quad (79)\end{aligned}$$

For a fixed-strain split, single-phase poroelastic coupling, the discretization of the flow equation returns,

$$\begin{aligned}\mathcal{L}(p^n) &= \left[\frac{1}{M}\frac{p_P^n - p_P^o}{\Delta t} + b\frac{(\nabla\cdot\mathbf{u})_P^o - (\nabla\cdot\mathbf{u})_P^{oo}}{\Delta t}\right]V_P \\ &\quad + \left[\frac{b^2\Delta t}{\lambda}\left(\frac{p_P^n - 2p_P^o + p_P^{oo}}{(\Delta t)^2}\right)\right]V_P \qquad (80)\end{aligned}$$

Under this iterative strategy, given sufficiently small time steps, the field equations can be uncoupled excepting evaluation of fracturing behaviors. Displacements are computed in order to estimate softening behavior at the end of the first softening iteration – i.e. to extend a propagating fracture. If fracturing processes initiate, then further fracturing may

occur within the same time step. Thus, still within the explicit time-marching formulation, but subsequent to fracture growth the approximation becomes:

$$\frac{\partial(\nabla\cdot\mathbf{u})^n}{\partial t} \approx \frac{\partial(\nabla\cdot\mathbf{u})^n}{\partial t}+\frac{b}{\lambda}\frac{\partial(p^n-p^{i_\mathbf{u}})}{\partial t}, \\ = \frac{(\nabla\cdot\mathbf{u})_P^n-(\nabla\cdot\mathbf{u})_P^o}{\Delta t}+\frac{b}{\lambda}[(\frac{p_P^n-p_P^o}{\Delta t})-(\frac{p_P^{i_\mathbf{u}}-p_P^o}{\Delta t})]. \quad (81)$$

Discretization of the pore flow equation returns,

$$\mathcal{L}(p^n) = [\frac{1}{M}\frac{p_P^n-p_P^o}{\Delta t}+b\frac{(\nabla\cdot\mathbf{u})_P^n-(\nabla\cdot\mathbf{u})_P^o}{\Delta t}]V_P \\ +[\frac{b^2}{\lambda}(\frac{p_P^n-p_P^o}{\Delta t})-\frac{b^2}{\lambda}(\frac{p_P^{i_\mathbf{u}}-p_P^o}{\Delta t})]V_P, \quad (82)$$

where n is the post-fracture iteration of the $\mathbf{u}-p$ system, whereas $i_\mathbf{u}$ represents the pre-fracture coupling iteration. Thus the result of Eq. (77) is recovered, here with effect for explicit time-marching. Eq. (82) can be iterated over within the same time step, until softening processes no longer initiate.

Interface pressures

Consider five types of interfaces: (a) interfaces discretizing the boundary of a porous medium adhered to an impermeable medium; (b) the interface of two impermeable media; (c) interfaces over which the porosity and permeability of the porous medium change, or "permeable medium interface"; (d) those interfaces over which Lamé's parameters vary, implying therefore a sharp discontinuity in the gradient of displacement, and consequently the requirement for an extensive method by which to ensure the continuity of total tractions, and which are called "material interfaces"; and, (e) interfaces over which the Lamé's parameters, permeability, residual stress state, and

Biot's coefficient may vary, and which constitute interfaces of both the material and the pore fluid flow continua, as well as coupling characteristics.

Yet the numerical handling is general, and requires only disparate treatment for two lumped groups of interfaces. These are: first, "closed interfaces" which groups interface types (a) and (b), from above; and second, "open interfaces", which groups interface types (c) - (e) – viz. where a representative interface p_i is obtainable, i.e. indicating ongoing cross-interface flow. Extrapolation of pressures at impermeable interfaces is presented in Table 5.

Open pore interfaces

Along a multi-material interface, the current cell P's properties are represented with the subscript ia. The interface-neighboring cell N_i's properties are represented with subscript ib. For a description of interface geometry, see Fig. 21. A representative pressure at these interfaces p_i is determinable (for both single- and multi-phase flows): it follows from the continuity assumption that $p_i = p_{ia} = p_{ib}$.

For example, a single-phase interface pressure can be approximated as follows. It is assumed that the interface permeability can be estimated from interface k_{ia} and k_{ib} alone; hence, averaging of adjacent permeabilities is used at the open pore interface. In the instance of Darcy flow, the flow equation's implicit spatial discretization as a Laplace equation argues for weighed harmonic averaging of the diffusivity constant. The interpolation to the polyhedral interface face (represented with the subscript i) is,

$$\overline{(k_p)}_i = \frac{k_{ia}k_{ib}}{\frac{\delta_{bn}}{\delta_{in}}k_{ia} + \frac{\delta_{an}}{\delta_{in}}k_{ib}}, \qquad p_i = \frac{\overline{(k_p)}_i \delta_{an}}{(k_p)_{ia}\delta_{in}}(p_{Ni} - p_P) + p_P, \quad (83)$$

where: $\overline{k_p}$ is the averaged permeability; p_P and p_{Ni} represent cell-center values of pore pressure in current and interface neighbor cells, respectively; and, $\delta_{in} = \delta_{an} + \delta_{bn}$ where δ_{an} is the distance from cell center to the interface. The effect of the interpolated interface pressure is linearly super-imposed to ascertain interface tractions.

Closed pore and impermeable interfaces

Our motivation to attempt to discretize impermeable media is driven by the use of steel casings to line wellbores during the completion of hydraulic fractures. Such impermeable media without disconnected porosity (such as steel) are numerically characterized by an exactly zero-valued Biot's coefficient ($b = 0$). These regions are assigned negligible porosities and permeabilities, in order to allow for solution of the pore pressure fluid flow over the entire numerical domain. However there is no coupled hydromechanical response to flow in these regions ($b = 0$).

Boundaries of impermeable media are zero-gradient boundaries with respect to pore fluid flow, such that $\mathbf{n} \cdot (\bar{k}_p/\mu_p)\nabla p = 0$. Along internal interfaces between permeable and impermeable media, the permeability is set to $\bar{k}_p = 0$. In the case of a tensorial permeability, setting for closed pore interfaces $\bar{\mathbf{K}}_p = (\mathbf{I} - \mathbf{n}_i\mathbf{n}_i) \cdot \mathbf{K}_p$, where $\mathbf{K}_p$ is the material-interior permeability was found to be insufficient to completely halt flow. This may be associated with using meshes that are not K-orthogonal. As such, the entire face-interpolated permeability is set to the zero tensor at the closed pore/impermeable interface. Lastly, the representative pressure at interfaces of impermeable media with connected porous media is set to the pore pressures of the adjacent cell-centers, when computing interface traction per Eq. (69).

MOMENTUM BALANCE DISCRETIZATION

The general approach to linearization of the momentum balance follows the "over-relaxed" solution approach [15]. Specifically, the coefficient of the vector Laplacian contributing implicitly evaluated matrix off-diagonal coefficients is $(2\mu + \lambda)$ (cognizable as the uniaxial bulk modulus). The semi-discretized form of momentum balance Eq. (59) equates hydromechanical terms as against the increment of effective tractions acting against the cell's surface.

In the case that Biot's coefficient is discontinuous over bimaterial interfaces, it is desirable to write:

$$\begin{aligned} \mathbf{0} \quad = \quad & \sum_f (\mathbf{t}_{\boldsymbol{\sigma}-\boldsymbol{\sigma}^0} + \cdot\, \sigma^0 - bp\mathbf{n})_f^n S_f + \sum_i (\mathbf{t}_{\mathbf{S}})_i^n S_i \\ & + \sum_b (\mathbf{t}_{\boldsymbol{\sigma}-\boldsymbol{\sigma}^0} + \cdot\, \sigma^0 - bp\mathbf{n})_b^n S_b \,. \end{aligned} \tag{84}$$

In the instance of am invariant Biot's coefficient, we may reduce Eq. (84) to:

$$\begin{aligned} [\nabla \cdot (bp\mathbf{I})_P^n - \nabla \cdot \boldsymbol{\sigma}_P^0] V_P \quad = \quad & \sum_f (\mathbf{t}_{\boldsymbol{\sigma}-\boldsymbol{\sigma}^0})_f^n S_f + \sum_i (\mathbf{t}_{\boldsymbol{\sigma}-\boldsymbol{\sigma}^0})_i^n S_i \\ & + \sum_b (\mathbf{t}_{\boldsymbol{\sigma}-\boldsymbol{\sigma}^0})_b^n S_b . \end{aligned} \tag{85}$$

Above, we presume all cell face tractions to have been converted to the increment of effective form, e.g. see later Eq. (103). Other linear operators are as follows. When applied to pore pressure gradient, representative cell-face center values of pressure are first obtained e.g. by weighted interpolation,

$$\nabla \cdot (bp\mathbf{I})_P = \nabla (bp)_P = \frac{1}{V_P} \sum_f \mathbf{n}_f b_f p_f S_f \,. \tag{86}$$

For numerical simulation of homogeneous domains, the hydromechanical coupling term is predominately evaluated as a simple pressure gradient term. The residual stress consideration, here expressed as a divergence, is here evaluated as (without discussion of adjustment for mesh non-orthogonality or skewness):

$$(\nabla p)_P = \frac{1}{V_P}\sum_f \mathbf{n}_f p_f S_f\,, \qquad (\nabla \cdot \boldsymbol{\sigma}^0)_P = \frac{1}{V_P}\sum_f \mathbf{n}_f \cdot \boldsymbol{\sigma}_P^0 S_f\,, \quad (87)$$

where reciprocal V_P is consistently a normalization term. The divergence operator also follows from Gauss-Green cell-based gradient evaluation. Convergence of the displacement equation is measured by a residual $R^{\mathbf{u}}$.

Bimaterial interfaces

The simultaneous decomposition of the traction into normal and tangential components, paired with the description of tractions as a combination of normal and tangential components of the gradient of displacement presented in Eqs. (64) and (65), which constituted Tuković's fungible and generative insight [11]. This presently allows for the method's extension to poroelastic and other coupled problems. Thus, it is shown that enforcing the continuity conditions of poroelasticity can be achieved as an extension of the linear algebraic system describing multi-material elasticity.

Normal traction

The normal component of traction vectors are defined along the current interface side (as $(\mathbf{t}_n^{\mathbf{S}})_{ia}$), and on the other side of the interface (as $(\mathbf{t}_n^{\mathbf{S}})_{ib}$). These equations are formed by discretizing Eq. (64):

$$(\mathbf{t}_n^{\mathbf{S}})_{ia} = (2\mu_{ia} + \lambda_{ia})\frac{(\mathbf{u}_n)_i - (\mathbf{u}_n)_P}{\delta_{an}} + \lambda_{ia}\mathbf{n}_i \mathrm{tr}(\nabla_t \mathbf{u}_t)_{ia} + \mathbf{n}_i\mathbf{n}_i \cdot (\mathbf{n}_i \cdot \boldsymbol{\sigma}_{ia}^0) - b_{ia}p_i\mathbf{n}_i, \quad (88)$$

$$(\mathbf{t}_n^{\mathbf{S}})_{ib} = (2\mu_{ib} + \lambda_{ib})\frac{(\mathbf{u}_n)_{Ni} - (\mathbf{u}_n)_i}{\delta_{bn}} + \lambda_{ib}\mathbf{n}_i \mathrm{tr}(\nabla_t \mathbf{u}_t)_{ib} + \mathbf{n}_i\mathbf{n}_i \cdot (\mathbf{n}_i \cdot \boldsymbol{\sigma}_{ib}^0) - b_{ib}p_i\mathbf{n}_i. \quad (89)$$

The sign associated with the unit normal applied to pressure, in Eqs. (88) and (89), follows from the physical continuity of traction outward from the interface. In essence, the substitution $\mathbf{n}_i = \mathbf{n}_{ia} = -\mathbf{n}_{ib}$ is made. This substitution is also used where the component is decomposed from a cell-centered tensor field (as in the case of the stored initial effective stress tensor). Along the current and the distant sides of the interface, the component of normal traction excluding the normal component of displacement dependency can be written as:

$$(\mathbf{t}_n^{-\mathbf{u}_n})_{ia} = \lambda_{ia}\mathbf{n}_i \mathrm{tr}(\nabla_t \mathbf{u}_t)_{ia} + \mathbf{n}_i\mathbf{n}_i \cdot (\mathbf{n}_i \cdot \boldsymbol{\sigma}_{ia}^0) - b_{ia}p_i\mathbf{n}_i, \quad (90)$$

$$(\mathbf{t}_n^{-\mathbf{u}_n})_{ib} = \lambda_{ib}\mathbf{n}_i \mathrm{tr}(\nabla_t \mathbf{u}_t)_{ib} + \mathbf{n}_i\mathbf{n}_i \cdot (\mathbf{n}_i \cdot \boldsymbol{\sigma}_{ib}^0) - b_{ib}p_i\mathbf{n}_i, \quad (91)$$

which are substituted into Eqs. (88) and (89), respectively, as a convenience. The continuity assumption of total normal traction at the interface Eq. (44) is used to equate Eqs. (88) and (89), with substitution of Eq. (90) and Eq. (91). This obtains the normal component of interface displacement (with respect to the interface face unit normal vector $\mathbf{n}_i$):

$$(\mathbf{u}_n)_i = \frac{(2\mu_{ia} + \lambda_{ia})\delta_{bn}(\mathbf{u}_n)_P + (2\mu_{ib} + \lambda_{ib})\delta_{an}(\mathbf{u}_n)_{Ni}}{(2\mu_{ia} + \lambda_{ia})\delta_{bn} + (2\mu_{ib} + \lambda_{ib})\delta_{an}} + \frac{\delta_{an}\delta_{bn}\left[\left(\mathbf{t}_n^{No-\mathbf{u}_n}\right)_{ib} - \left(\mathbf{t}_n^{No-\mathbf{u}_n}\right)_{ia}\right]}{(2\mu_{ia} + \lambda_{ia})\delta_{bn} + (2\mu_{ib} + \lambda_{ib})\delta_{an}}. \quad (92)$$

Case	Material a	Material b	Pressure continuity	Pressure values	Biot's coefficient
I.	Impermeable	Impermeable	Discontinuous	Interface p_{ia} & p_{ib}	Interface b_{ia} & b_{ib}
II.	Permeable	Impermeable	Discontinuous	Interface p_{ia} & p_{ib}	Interface b_{ia} & b_{ib}
III.	Impermeable	Permeable	Discontinuous	Interface p_{ia} & p_{ib}	Interface b_{ia} & b_{ib}
IV.	Permeable	Permeable	Continuous	Interpolated p_i	Interface b_{ia} & b_{ib}

Table 5: Pressure Extrapolation

Substituting the normal component of displacement of Eq. (92) into the normal component of traction definition of Eq. (88), we find the traction's normal component,

$$(\mathbf{t}_n^{\mathbf{S}})_i = \overline{(2\mu+\lambda)}_i \frac{(\mathbf{u}_n)_{Ni} - (\mathbf{u}_n)_P}{\delta_{in}} + \frac{(2\mu_{ia}+\lambda_{ia})\delta_{bn}(\mathbf{t}_n^{-\mathbf{u}_n})_{ib} + (2\mu_{ib}+\lambda_{ib})\delta_{an}(\mathbf{t}_n^{-\mathbf{u}_n})}{(2\mu_{ia}+\lambda_{ia})\delta_{bn} + (2\mu_{ib}+\lambda_{ib})\delta_{an}}, \quad (93)$$

where weighed harmonic averaging obtains a representative elastic material coefficient over the interface.

Tangential traction

The tangential component of traction vectors are formed in the same manner as Eqs. (88) and (89). The discretized form of Eq. (65) is,

$$(\mathbf{t}_t^{\mathbf{S}})_{ia} = \mu_{ia}\frac{(\mathbf{u}_t)_i - (\mathbf{u}_t)_P}{\delta_{an}} + \mu_{ia}(\nabla_t u_n)_{ia} + (\mathbf{I} - \mathbf{n}_i\mathbf{n}_i)\cdot(\mathbf{n}_i\cdot\boldsymbol{\sigma}_{ia}^0), \quad (94)$$

$$(\mathbf{t}_t^{\mathbf{S}})_{ib} = \mu_{ib}\frac{(\mathbf{u}_t)_{Ni} - (\mathbf{u}_t)_i}{\delta_{bn}} + \mu_{ib}(\nabla_t u_n)_{ib} + (\mathbf{I} - \mathbf{n}_i\mathbf{n}_i)\cdot(\mathbf{n}_i\cdot\boldsymbol{\sigma}_{ib}^0), \quad (95)$$

where the pore pressure exerts no tangential stresses along the interface. Along the interface, the components of tangential total and effective traction excluding the normal component of displacement dependency can be written as:

$$(\mathbf{t}_t^{-\mathbf{u}_t})_{ia} = \mu_{ia}(\nabla_t u_n)_{ia} + (\mathbf{I} - \mathbf{n}_i\mathbf{n}_i)\cdot(\mathbf{n}_i \cdot \boldsymbol{\sigma}_{ia}^0), \quad (96)$$

$$(\mathbf{t}_t^{-\mathbf{u}_t})_{ib} = \mu_{ib}(\nabla_t u_n)_{ib} + (\mathbf{I} - \mathbf{n}_i\mathbf{n}_i)\cdot(\mathbf{n}_i \cdot \boldsymbol{\sigma}_{ib}^0), \quad (97)$$

which are substituted into Eqs. (94) and (95), respectively. Enforcing continuity of tangential tractions Eq. (45), and therefore equating Eqs. (94) and (95), the tangential displacement at the interface becomes:

$$(\mathbf{u}_t)_i = \frac{\mu_{ia}\delta_{bn}(\mathbf{u}_t)_P + \mu_{ib}\delta_{an}(\mathbf{u}_t)_{Ni}}{\mu_{ia}\delta_{bn} + \mu_{ib}\delta_{an}} + \frac{\delta_{an}\delta_{bn}[(\mathbf{t}_t^{-\mathbf{u}_t})_{ib} - (\mathbf{t}_t^{-\mathbf{u}_t})_{ia}]}{\mu_{ia}\delta_{bn} + \mu_{ib}\delta_{an}}. \quad (98)$$

The result of above is then substituted into Eq. (94), the traction's tangential component is:

$$(\mathbf{t}_t^{\mathbf{S}})_i = \bar{\mu}_i \frac{(\mathbf{u}_t)_{Ni} - (\mathbf{u}_t)_P}{\delta_{in}} + \frac{\mu_{ia}\delta_{bn}(\mathbf{t}_t^{-\mathbf{u}_t})_{ib} + \mu_{ib}\delta_{an}(\mathbf{t}_t^{-\mathbf{u}_t})_{ia}}{\mu_{ia}\delta_{bn} + \mu_{ib}\delta_{an}}, \quad (99)$$

where weighted harmonic averaging again obtains a representative shear modulus over the interface. By summation of Eq. (93) and Eq. (99), the traction vector at the interface is recovered,

$$\mathbf{t}_i^{\mathbf{S}} = \overline{(2\mu+\lambda)}_i \frac{\mathbf{u}_{Ni} - \mathbf{u}_P}{\delta_{in}} - [\overline{(2\mu+\lambda)}_i - \bar{\mu}_i]\frac{(\mathbf{u}_t)_{Ni} - (\mathbf{u}_t)_P}{\delta_{in}} + \frac{(2\mu_{ia}+\lambda_{ia})\delta_{bn}(\mathbf{t}_n^{-\mathbf{u}_n})_{ib} + (2\mu_{ib}+\lambda_{ib})\delta_{an}(\mathbf{t}_n^{-\mathbf{u}_n})_{ia}}{(2\mu_{ia}+\lambda_{ia})\delta_{bn} + (2\mu_{ib}+\lambda_{ib})\delta_{an}} + \frac{\mu_{ia}\delta_{bn}(\mathbf{t}_t^{-\mathbf{u}_t})_{ib} + \mu_{ib}\delta_{an}(\mathbf{t}_t^{-\mathbf{u}_t})_{ia}}{\mu_{ia}\delta_{bn} + \mu_{ib}\delta_{an}}. \quad (100)$$

Matrix assembly is by extension of Tuković with linear super-position of poroelastic and residual traction components. In order to numerically obtain displacement

gradient tangential components, various means for the approximation of the tangential component of displacement have been investigated [11]. In general these operations are resolved using separate linear operators.

Skeletal tractions and boundary gradients

Effective stress boundary tractions (Eq. (62)) must by the application of those identities be converted into their incremental counterpart $\mathbf{t}_{\boldsymbol{\sigma}-\boldsymbol{\sigma}^0}$, in order to set a fixed gradient on the displacement equation. Likewise, total stress boundary tractions (Eq. (63)) must be converted to $\mathbf{t}_{\boldsymbol{\sigma}-\boldsymbol{\sigma}^0}$. Hence when Eq. (67) is discretized, the effective traction vector for boundary faces becomes:

$$(\mathbf{t_S})_b^n = (\mathbf{t}_{\boldsymbol{\sigma}-\boldsymbol{\sigma}^0})_b^n + \mathbf{n}\cdot\boldsymbol{\sigma}_b^0 - (bp)_b^n\mathbf{n}_b, \tag{101}$$

$$\begin{aligned}(\mathbf{t}_{\boldsymbol{\sigma}-\boldsymbol{\sigma}^0})_b^n &= (2\mu_b+\lambda_b)\mathbf{n}_b\cdot(\nabla\mathbf{u})_b^n - (\mu_b+\lambda_b)\mathbf{n}_b\cdot(\nabla\mathbf{u}_t)_b^n \\ &\quad +\mu_b(\nabla_t u_n)_b^n + \lambda_b\mathbf{n}_b\mathrm{tr}(\nabla_t\mathbf{u}_t)_b^n[(\nabla\mathbf{u}_t)_b^n], \\ &= (2\mu_b+\lambda_b)\mathbf{n}_b\cdot(\nabla\mathbf{u})_b^n - (\mu_b+\lambda_b)\mathbf{n}_b\cdot(\nabla\mathbf{u})_b^n \\ &\quad +\mu_b\mathbf{n}_b\cdot\left[(\nabla\mathbf{u})_b^{\mathrm{T}}\right]^n + \lambda_b\mathbf{n}_b\mathrm{tr}(\nabla\mathbf{u})_b^n[(\nabla\mathbf{u}_t)_b^n].\end{aligned} \tag{102}$$

Above Eq. (102) is provided to Eqs. (84) and (85) for the full discretization of stress boundary conditions (without discussion of boundary-cell skewness). In the case of specified displacement, no special adjustment for the residual stress state or poroelasticity is required. Therefore, by equating an imposed boundary traction $\mathbf{t_S}$ with Eq. (102), a fixed traction boundary condition is applied:

$$\begin{aligned}\mathbf{n}_b\cdot(\nabla\mathbf{u})_b^n &= \frac{\overset{\mathbf{t}_{\boldsymbol{\sigma}-\boldsymbol{\sigma}^0}}{(\mathbf{t_S} -\cdot\,\sigma_b^0 + bp\mathbf{n})_b^n}}{(2\mu_b+\lambda_b)} \\ &\quad + \frac{\mathbf{n}_b\cdot[(\mu_b+\lambda_b)(\nabla\mathbf{u})_b^n - \mu_b[(\nabla\mathbf{u})_b^{\mathrm{T}}]^n]}{(2\mu_b+\lambda_b)} \\ &\quad - \frac{\lambda_b\mathbf{n}_b\mathrm{tr}(\nabla\mathbf{u})_b^n}{(2\mu_b+\lambda_b)}.\end{aligned} \tag{103}$$

Frequently in geomechanics modeling, far-field stresses are specified as a fixed in situ total stress tensor ($\mathbf{S}^0$) which may be spatially variable, i.e. between rock layers and with depth. To run simulations more easily and with lesser opportunity for unintended error, it is sometimes attractive to set fixed displacements at domain boundaries. Alternately, the tractions applied at far-field boundaries can automatically be specified as the resolved residual stress tensor by setting:

$$(\mathbf{t_S})_b^n = \mathbf{n}_b \cdot \mathbf{S}_b^0. \quad (104)$$

Specifically if all boundary conditions are applied as tractions per Eq. (104) for boundary pressures specified at value p^0, this implies a continuity of the resolved total stress tensor over every boundary and hence an equilibrium state near the far boundary. The surface-normal gradient Eq. (103) with substitution of Eq. (104) is then:

$$\begin{aligned} \mathbf{n}_b \cdot (\nabla \mathbf{u})_b^n \quad = \quad & \frac{(bp\mathbf{n} - bp^0\mathbf{n})_b^n}{(2\mu_b + \lambda_b)} \\ & + \frac{\mathbf{n}_b \cdot [(\mu_b + \lambda_b)(\nabla \mathbf{u})_b^n - \mu_b[(\nabla \mathbf{u})_b^{\mathrm{T}}]^n]}{(2\mu_b + \lambda_b)} \\ & - \frac{\lambda_b \mathbf{n}_b \mathrm{tr}(\nabla \mathbf{u})_b^n}{(2\mu_b + \lambda_b)}, \end{aligned} \quad (105)$$

where p_b may also be fixed.

Skeletal tractions and boundary gradients

It may be desirable to introduce a vertical gradient in the initial total stress tensor $\mathbf{S}^0$ or pore pressures p^0, corresponding to the effect of gravity. In this instance, the introduction of body force term should be carefully coordinated, in order that the system not be initialized to disequilibrium in the reference configuration. Therefore, in order to linearly decrease the vertical component of the initial stress with depth, as well as prevent

rapid fluid loss from overpressured pay layers, initial stress state, body forces, and even permeabilities within shale barriers must be jointly coordinated.

This concern is independent of the use of a multi-material correction procedure, and applies to all coupling splits presented. For this reason, we have indicated that the vertical stresses must be specified as a "constant value". Yet, if and where the normal components of initialized effective stresses do indeed vary over an interface, it is shown that the interface correction term enables accurate stress analysis – by comparison to Eshelby's inclusion, below.

NUMERICAL RESULTS

Verification cases are presented for: (a) Biot's consolidation with regard to a fixed-stress split case, (b) Mandel's problem and (c) stress-state evaluation with a fixed (numerically unsolved) pore pressure distribution, for which there exists an analytic solution.

Terzaghi's problem

All poroelastic couplings are validated against Terzaghi's 1D consolidation problem ([25]), with material properties listed in Table 6. A rectangular column with height $2h$ of 40 m was held at an initial uniform pressure of 0 Pa. During phase 1, a downward normal traction S_0 of 1E+5 Pa was applied on the top and bottom of the column. Zero outward displacement conditions were applied on other boundaries. No flow was allowed through any boundary. The final phase 1 pressure inside the column was computed to be 36,448 Pa, and matches the linearized analytic solution.

Phase 2 entailed relieving the no-flow boundary condition at the top and bottom boundaries by application of a zero pressure condition. Loading conditions during phase

2 are presented in Fig. 24. Only the x_1-symmetric half-space was discretized and solved (length h), with a zero-displacement boundary condition at along the symmetric axis.

Results for pressure and displacement during Phase 2 are as presented in Fig. 25 for pressures and in Fig. 26 for displacements, with curves labeled by time [s]. Unusually, the multi-material solution procedure was used to recover the solution; each material was allocated to an equivalent extent (length $h/2$). Thus the full bimaterial treatment was utilized in order to converge the displacements during ongoing flow. Error was greatest during early-time flow (t = 20 s curve), and error reduces with decreased time-step size.

Mandel's problem

All poroelastic couplings are validated against Mandel's 2D problem [19], with the same material properties listed in Table 6. A slab of infinite out-of-plane length with in-plane extent $2a$ of 40 m was held at an initial uniform pressure of 0 Pa. A downward normal traction S_0 of 1E+5 Pa is applied on top of the impermeable confining plates, and no displacement allowed at the bottom. Zero traction and pressure conditions were applied on other boundaries, at which outflow was allowed. Loading conditions are presented in Fig. 27.

Results for pressure are presented in Fig. 28, with curves labeled by time [s]. The results overlay the analytic solution. Only the x_1- and x_2-symmetric quarter-space was discretized and solved (length a); the analytic solution at the plate is applied and is presented as recovered, Fig. 29. Error was greatest during early-time flow (t = 20 s curve), and error reduces with decreased time-step size.

Porosity, ϕ^0 [-]	0.2
Permeability, k_p [m^2]	1.5E-14
Biot's Coefficient, b [-]	0.6
Young's Modulus, E [Pa]	1E+10
Poisson's Ratio, v [-]	0.2
Viscosity, μ_p [Pa-s]	0.001
Fluid Bulk Modulus, K_p [Pa]	2.3E+9
Downward normal traction, S_0 [Pa]	1E+5

Table 6: Terzaghi and Mandel's Problems

Inhomogeneous inclusion

With regard to verification of poroelastic stress analysis, a case is presented describing an elliptical inclusion in 2D plane strain. The extent of the enclosing matrix is presumed to be infinite, whereas the inclusion is both spatially finite and materially inhomogeneous. The ellipse's major and minor axes coincide with axes x_1 and x_2, with horizontal and vertical semi-axes of length a_1^* and a_2^*, Fig. 30. The Lamé's parameters of the inclusion with respect to the matrix are discontinuous, and are marked by superscripting $*$.

The solution is Eshelby's inclusion method for plane-strain poroelasticity [42]. It describes stresses induced by a dilational stress change within the inhomogeneity. These changes can be caused either by a pore pressure Δp, or a dilational change in the residual stresses $\Delta\sigma^0$. The result of the analysis is to recover non-dimensional and tensorial stress arching ratios $\boldsymbol{\gamma}_\alpha^*$ and $\boldsymbol{\gamma}_\alpha$. Together, these arching ratios describe the field-wide stress state: as such, $\boldsymbol{\gamma}_\alpha^*$ is spatially invariant but applies only within the inclusion; in contrast, the components of $\boldsymbol{\gamma}_\alpha$ decline in absolute value with increasing distance from the inclusion.

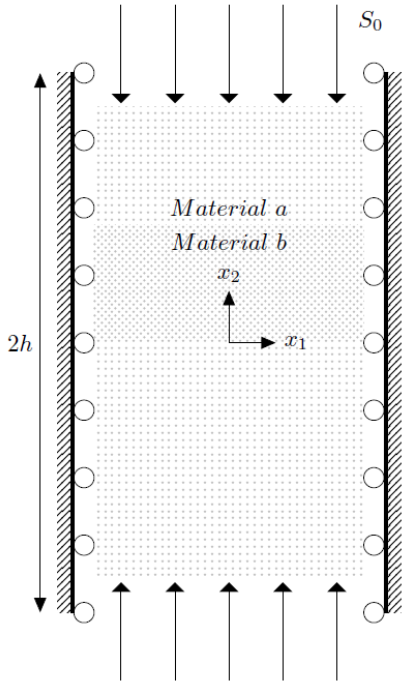

Figure 24: Terzaghi's problem test case during phase 2 loading, with homogeneous materials a and b receiving full bimaterial treatment..

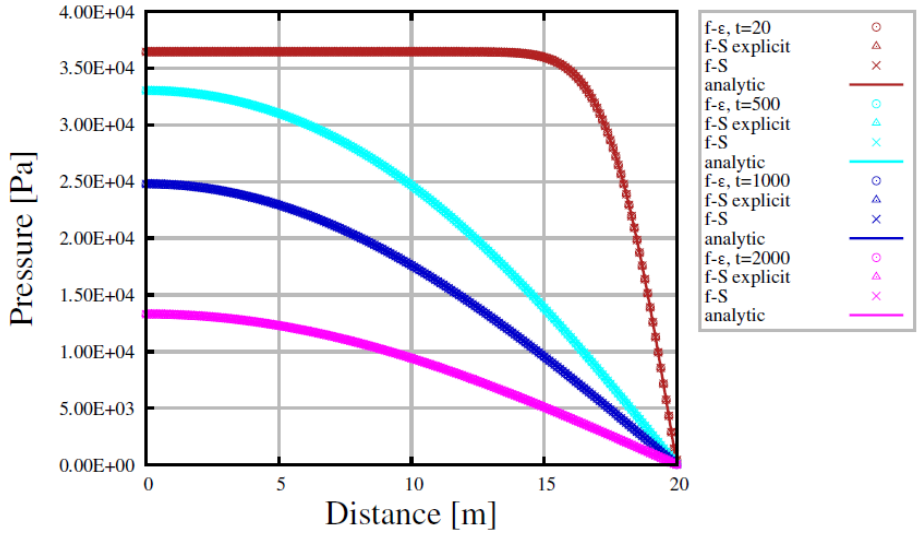

Figure 25: Terzaghi's problem test case, recovered pore pressures.

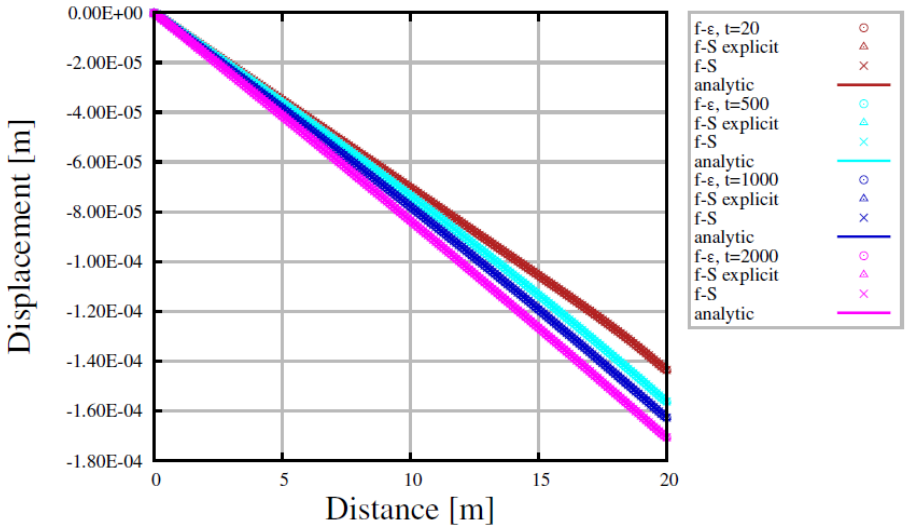

Figure 26: Flow chart of fixed-stress solver logic.

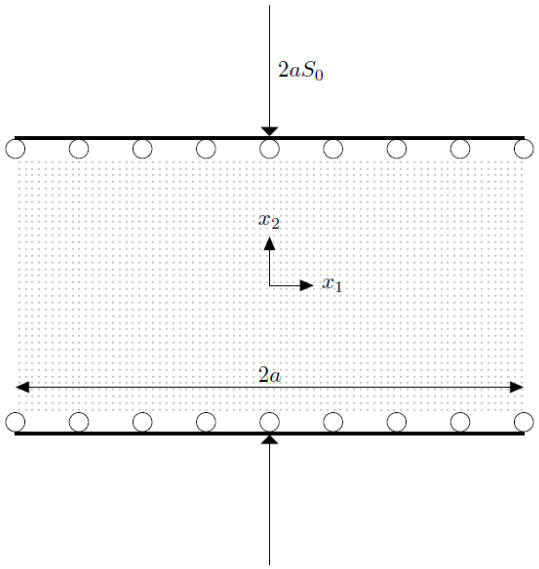

Figure 27: Mandel's problem test case, dimensions and loading.

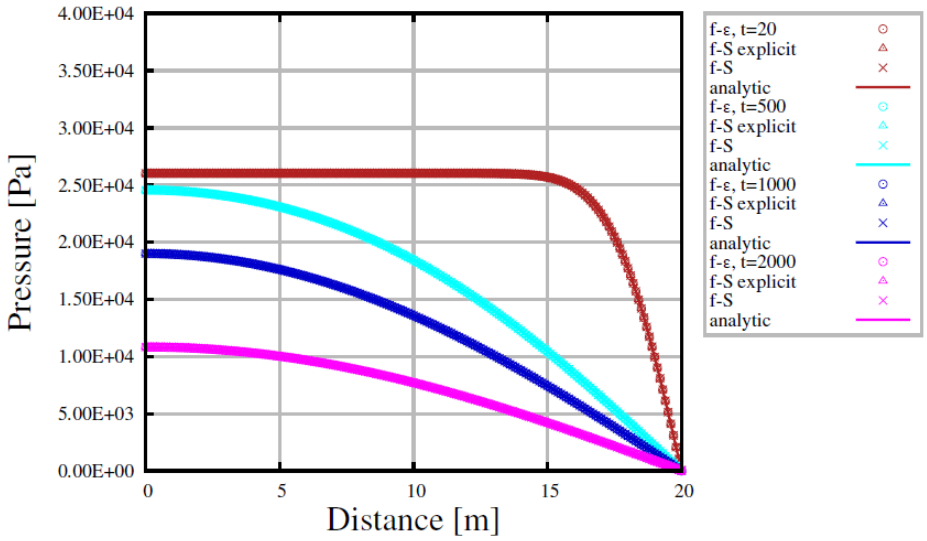

Figure 28: Mandel's problem test case, recovered pore pressures.

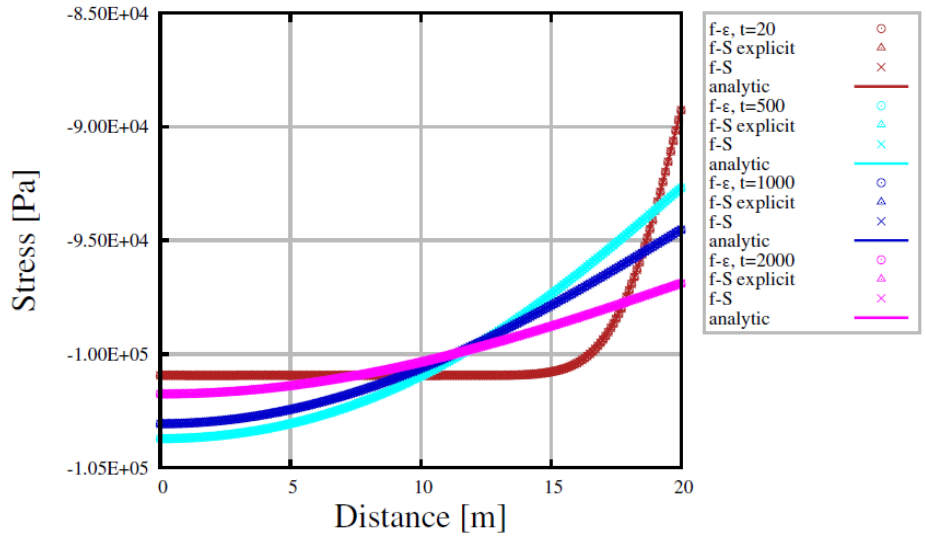

Figure 29: Mandel's problem test case, enforced/recovered stresses.

Parameter	Inclusion	Matrix
Pore pressure, p^0 [J/m^2]	Δp	-
Residual stress tensor, $\mathbf{S}^0$ [Pa]	$\Delta\sigma^0\mathbf{I}$	-
Biot's Coefficient, b [-]	1.0	-
Young's Modulus, E [Pa]	-	20E+9
Poisson's Ratio, v [-]	0.2	0.2
Horizontal dimension, a_1 [m]	1.5	$50a_1^*$
Vertical dimension, a_1 [m]	1	$50a_2^*$

Table 7: Matrix and Inclusion

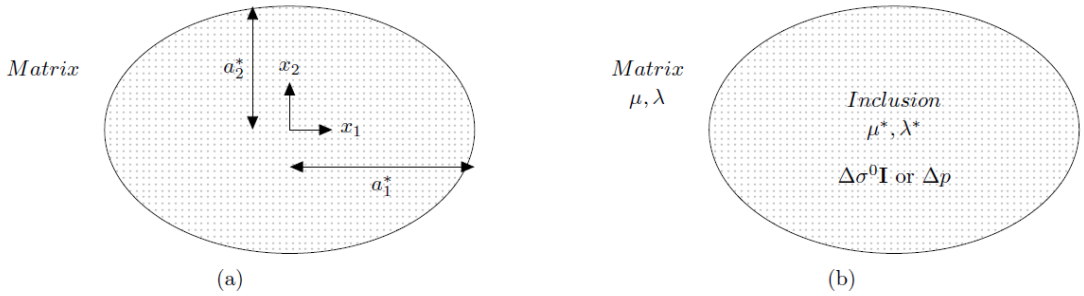

Figure 30: Inhomogeneous inclusion test case, (a) dimensions and (b) loading.

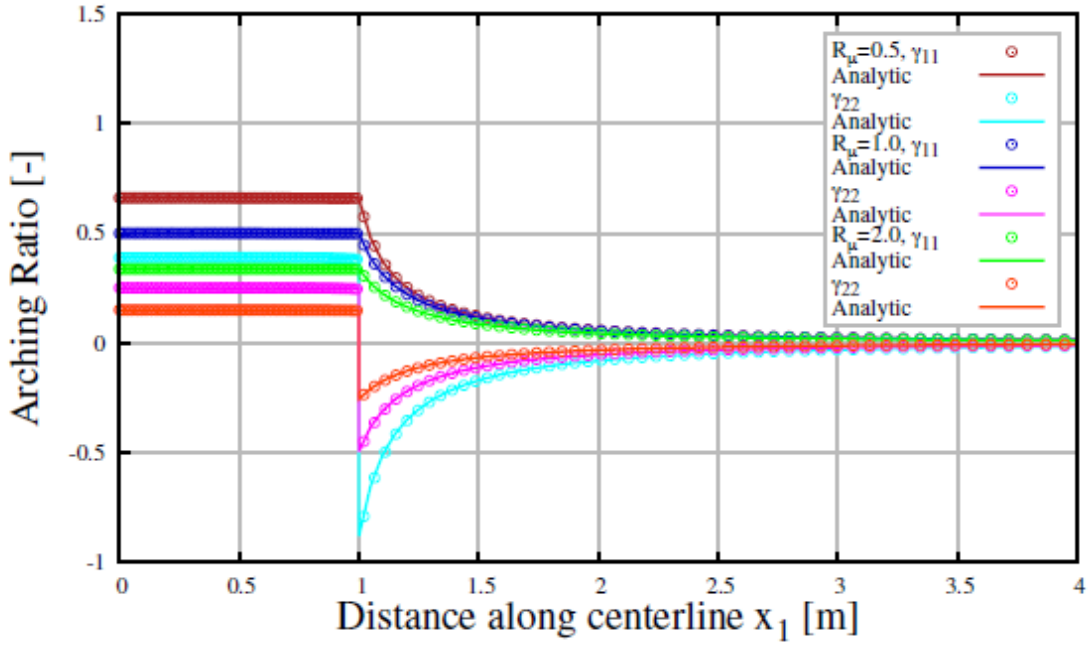

(a)

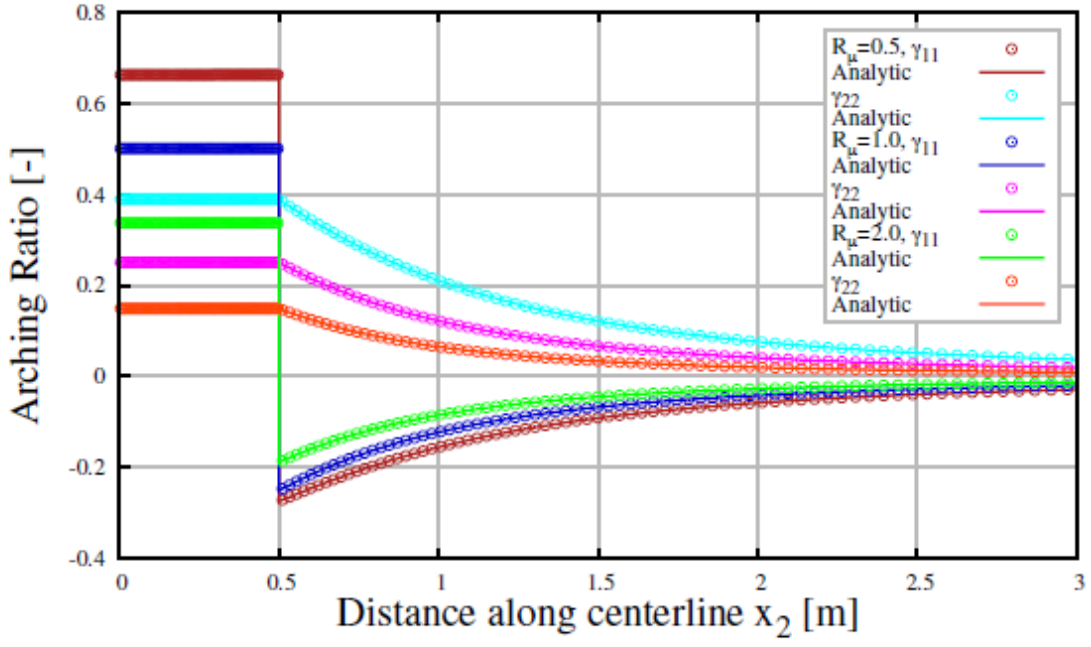

(b)

Figure 31: Inhomogeneous inclusion test case, showing $\boldsymbol{\gamma}_{\alpha}^{*}$ and $\boldsymbol{\gamma}_{\alpha}$ (after [42]).

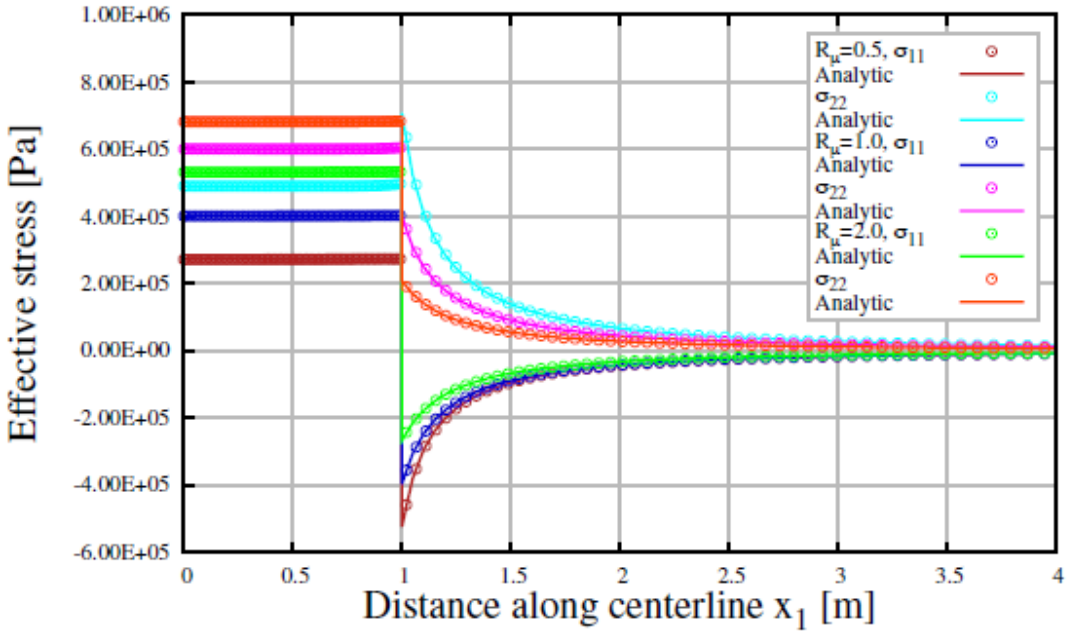

(a)

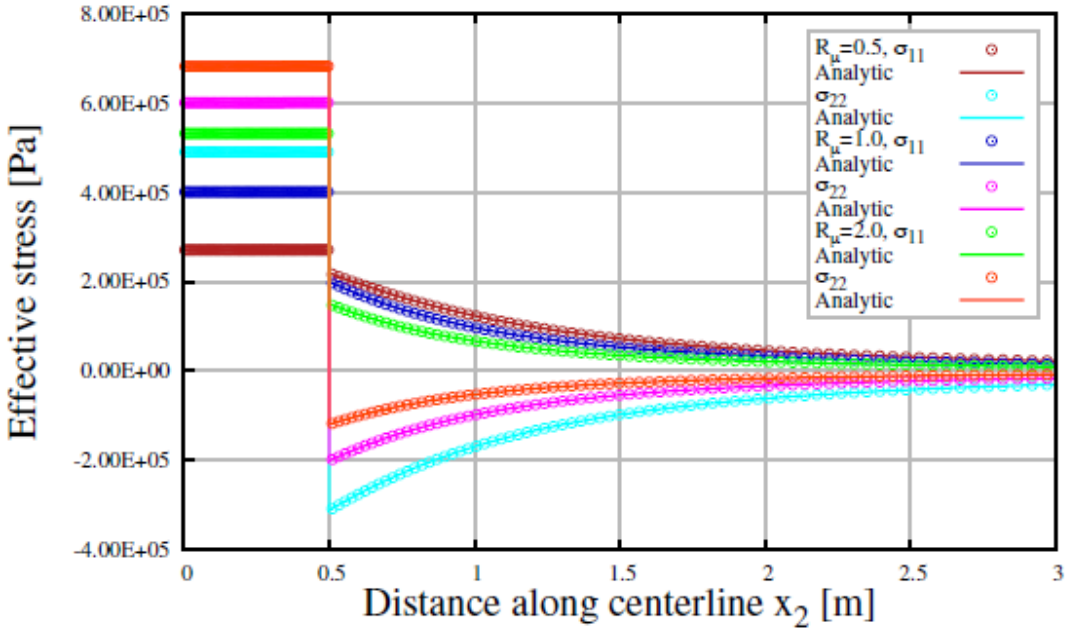

(b)

Figure 32: Inhomogeneous inclusion test case, showing $\Delta\boldsymbol{\sigma}^*$ and $\Delta\boldsymbol{\sigma}$ for change Δp.

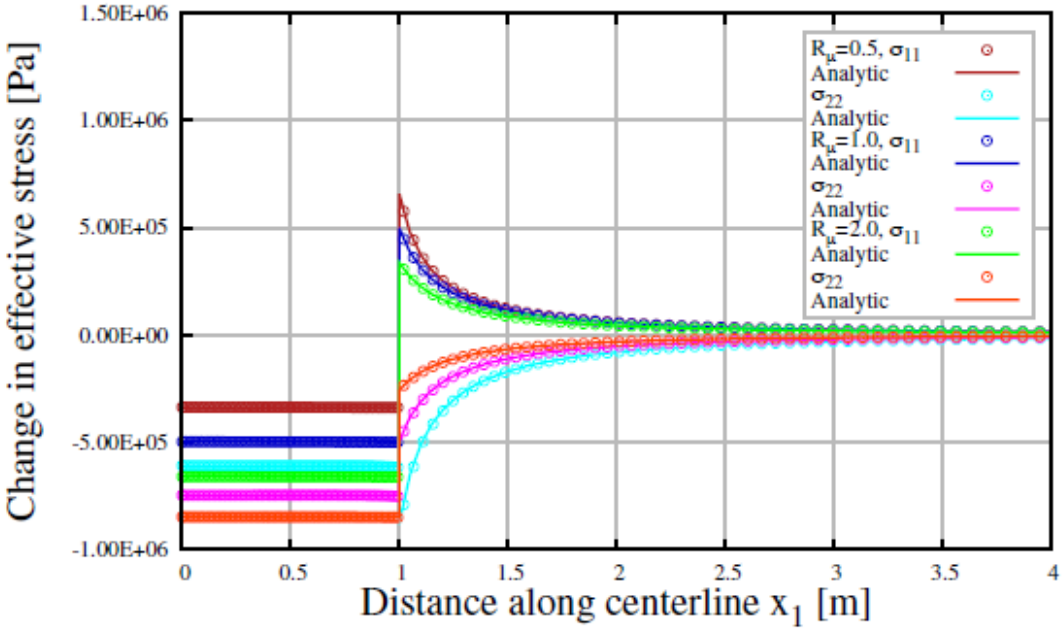

(a)

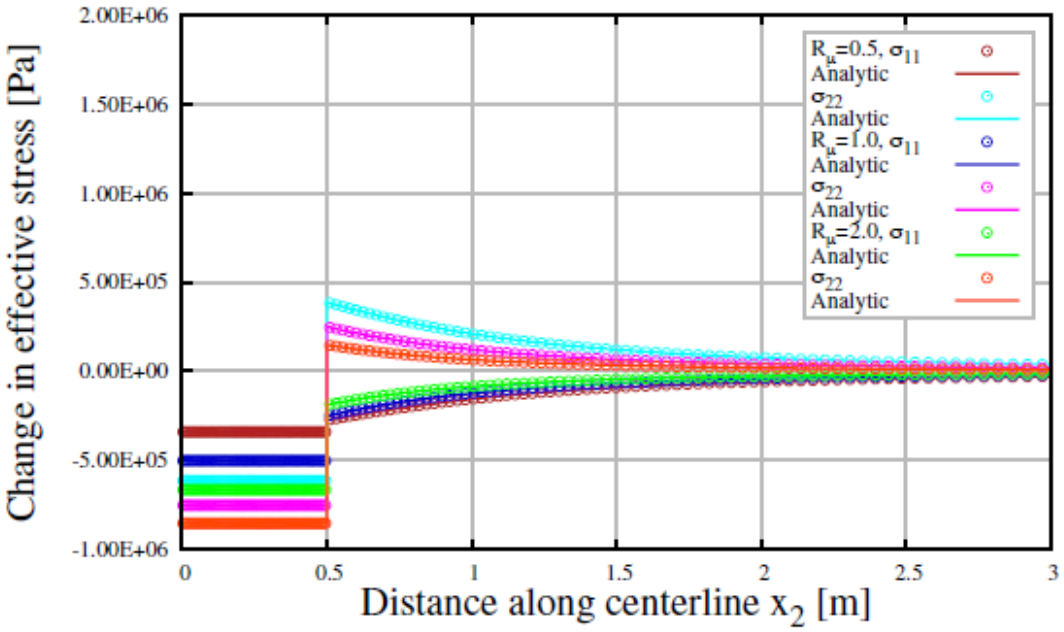

(b)

Figure 33: Inhomogeneous inclusion test case, showing $\Delta\boldsymbol{\sigma}^*$ and $\Delta\boldsymbol{\sigma}$ for change $\Delta\sigma^0$.

Parameter	Rock	Steel
Pore pressure, p^0 [Pa]	10.0E+6	-
Horizontal Min. Stress, S_{hmin} [Pa]	12.0E+6	12.0E+6
Horizontal Max. Stress, S_{Hmax} [Pa]	14.0E+6	14.0E+6
Porosity, ϕ^0 [-]	0.25	-
Permeability, k_p [m^2]	1.5E-18	-
Biot's Coefficient, b [-]	0.5	-
Young's Modulus, E [Pa]	20E+9	200E+9
Poisson's Ratio, v [-]	0.3	0.3
Viscosity, μ_p [Pa-s]	0.001	-
Fluid Bulk Modulus, K_p [Pa]	2.3E+9	-

Table 8: Rock and Steel

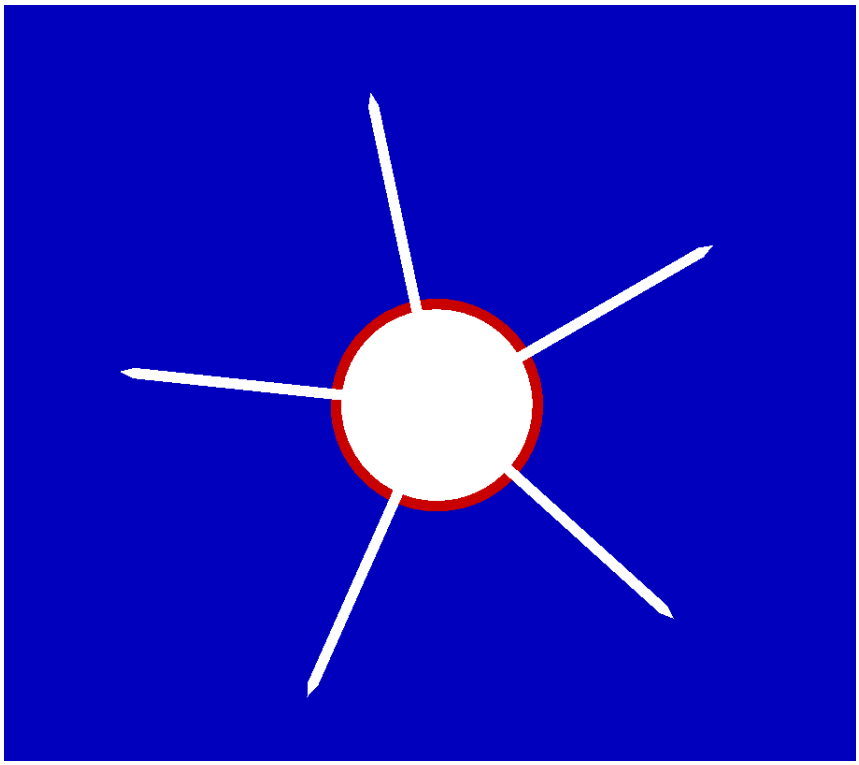

Figure 34: Rock and steel case (formation in darker color, steel in lighter).

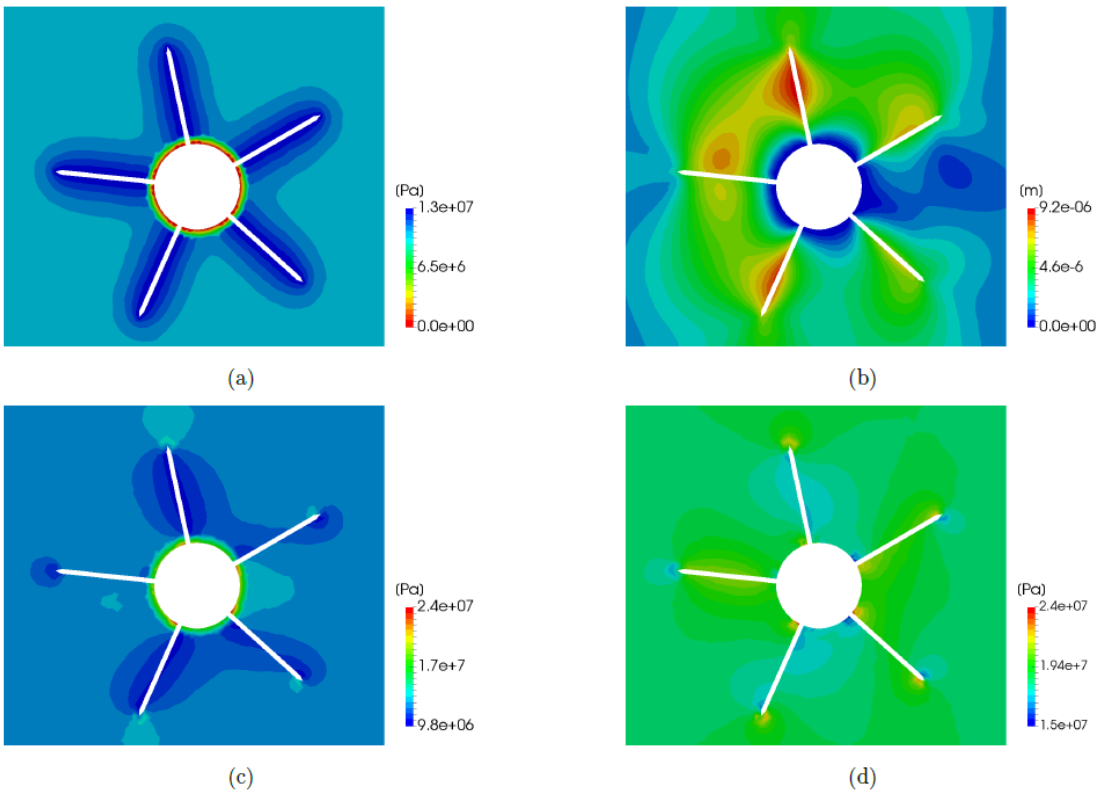

Figure 35: Rock and steel case, showing at t = 60 s: (a) pressure; (b) displacement; (c) effective stress magnitude; and, (d) total stress magnitude.

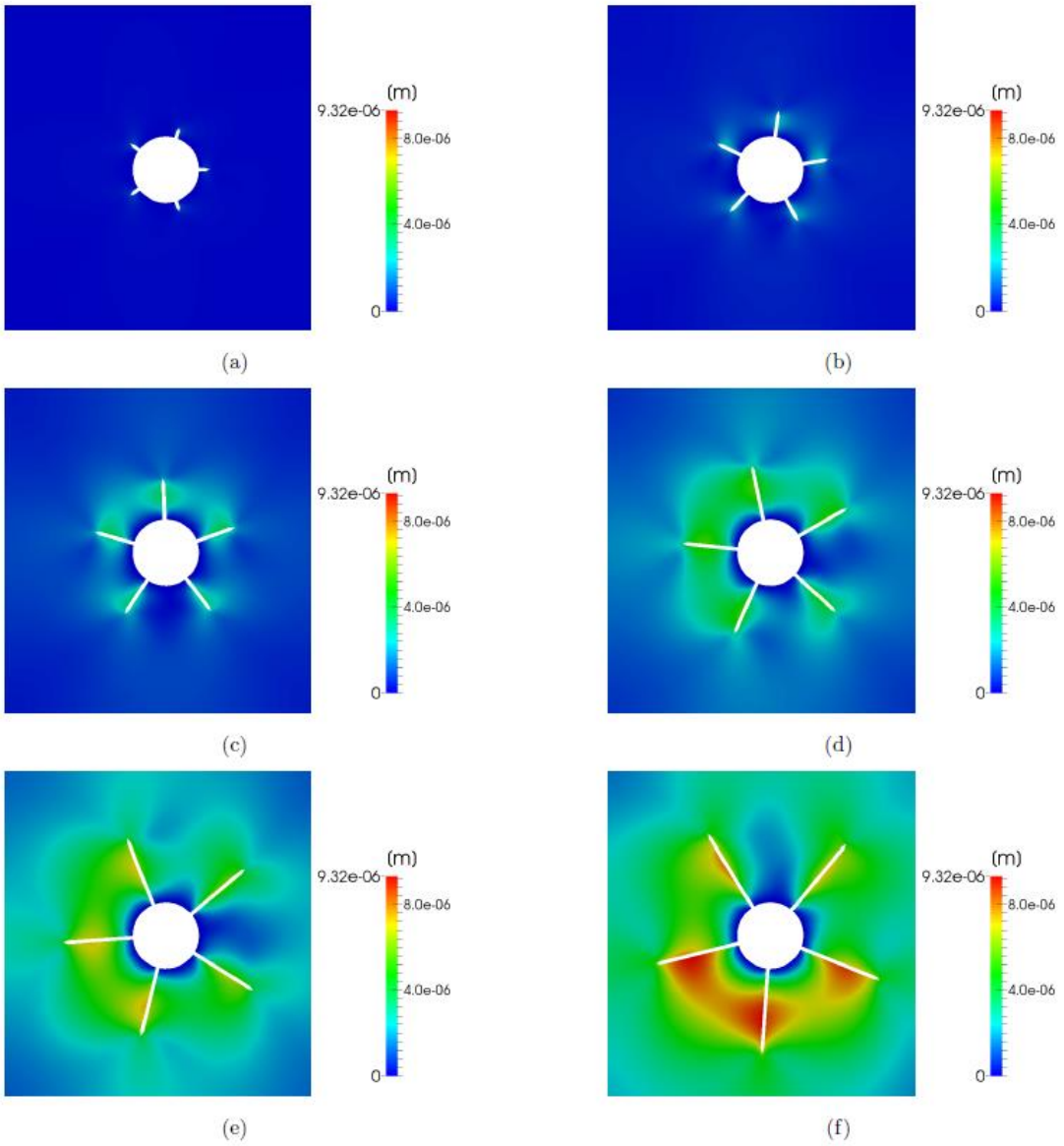

Figure 36: Rock and steel case showing displacement at t = 60 s, parametrically increasing perforation extension by 0.4 R from 0.2 R with rotation 10°.

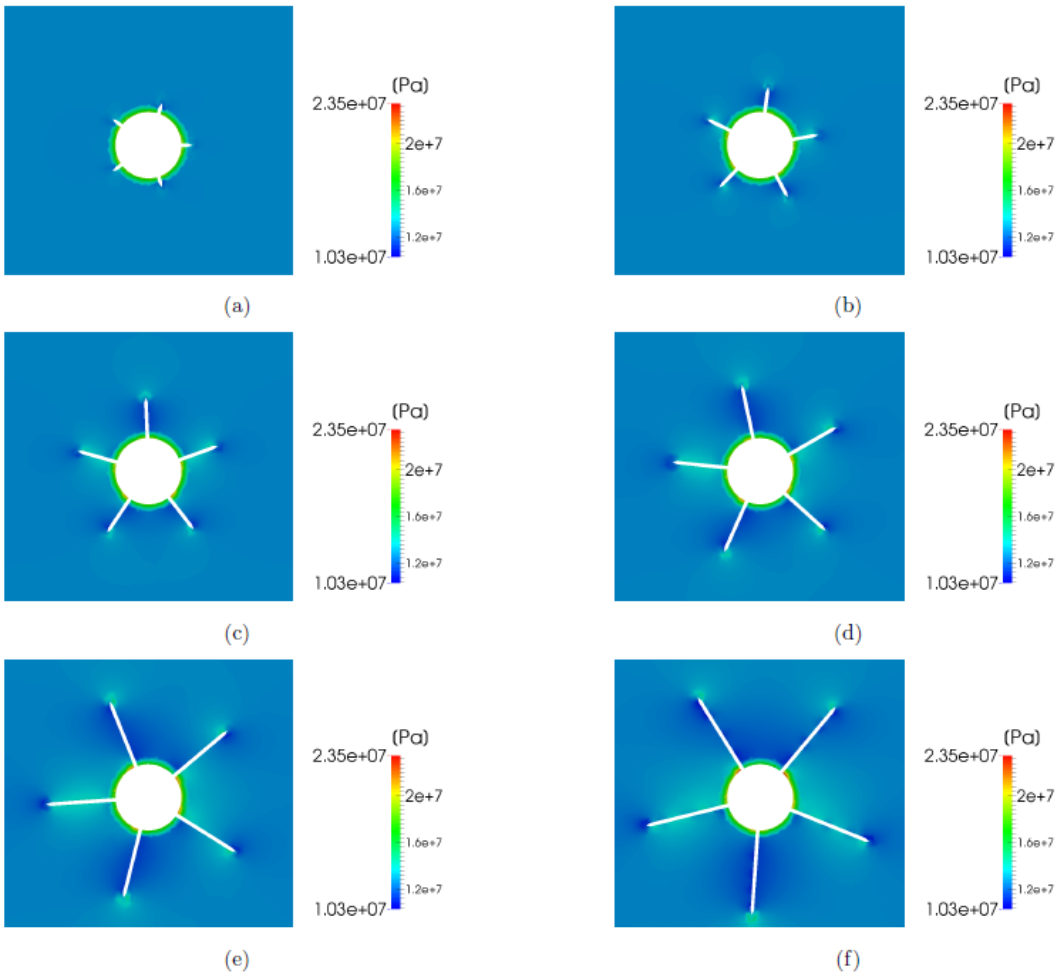

Figure 37: Rock and steel case showing stress at $t = 60$ s, parametrically increasing perforation extension by 0.4 R from 0.2 R with rotation 10°.

The nature of the dimensionless solution is independent of the included area. It requires non-dimensional parameters,

$$e = \frac{a_2^*}{a_1^*}, \qquad R_\mu = \frac{\mu^*}{\mu} \quad (106)$$

where e is the elliptical dimension ratio, and R_μ is the ratio of the inclusion over the matrix's shear modulus. The solution is also sensitive to differences in Poisson's ratios ν^* versus ν.

Open pore continuity conditions corresponding to Eqs. (40-43) cannot be used to match the solution. A sharp pressure contrast must be employed at the interface. Specifically, the pressure change occurs uniformly, within the heterogeneity. As such, a discontinuous pressure field was used for matching the analytic stress field. Substituting closed pore continuity conditions recovers the analytic solution for $\boldsymbol{\gamma}_\alpha^*$ and $\boldsymbol{\gamma}_\alpha$, as plotted in Fig. 31 – which presents recovery of the example calculations provided [42]. Finally while infinite in theory, our numerical model was run within a matrix of finite extent. The matrix dimensions of the finite matrix domain are also elliptical and dimensioned a_1 and a_2,. At the far-field boundaries, the condition of zero displacement is specified. Model parameters are in Table 7.

Pore pressure

The inclusion test case can be used to verify the mathematical model and implementation of methods to superimpose additional poroelastic components of the traction. A pore pressure change Δp is initialized in the inclusion, and the resulting numerically computed stress analyzed. For a zero initial effective stress, the change in effective stress becomes the converged effective stress state. A good match to the analytic

solution is presented in Fig. 32. Error is greatest along the x_1 axis inside the inclusion near the interface, and error reduces with increased local mesh refinement.

Residual stress

The semi-analytic description of the same inclusion test case can be augmented to verify cross-interface resolved residual stress application. The diagonal tensor $\mathbf{S}^{0*} = \Delta\sigma^0\mathbf{I}$ is initialized in the inclusion, and also pore pressure change $\Delta p = 0$. The created eigenstrain is therefore dilational, and hence conforms to the solution's requirement. A good match to the analytic solution is presented in Fig. 33; the change in effective stress shown is $\Delta\boldsymbol{\sigma}^* = \boldsymbol{\sigma}^* - \Delta\sigma^0\mathbf{I}$ in the inclusion and $\Delta\boldsymbol{\sigma} = \boldsymbol{\sigma}$ in the matrix.

Metal casing

A multi-material interface case is run in 2D plane-strain. The outer radius of the steel wellbore is R = 3" with an inner radius of 0.9 R. The width of each perforation is 0.1 R, and there are five perforations. Each perforation extends 2 R into the poroelastic formation. Material parameters are displayed in Table 8. Results of the multi-material stress analysis are presented in Fig. 35. The exposed perforation surface has been pressurized to 13.0E+6. Pore fluid diffusion occurs in the formation but not in the steel, where the pressure field is initialized to and remains 0. As such, the interface between steel and rock acts as a no-flow boundary.

The key result is the contrast of Fig. 35c versus Fig. 35d. Poroelastic effects are strongly evident in the vicinity of the perforations. Effective stresses are strongly discontinuous at the rock/steel interface, varying with the step change in pore pressure. Yet the stress field remains completely continuous as traveling across the bimaterial interface. Stress concentrations form at: locations along the casing-interior steel surface,

consonant with the fixed displacement boundary condition; and, within the near-tip region of the perforation locations.

The FV discretization provides for immediate parametrization of model geometry, even for multi-material cases. A parameterization of both induced displacements and stresses is presented, Fig. 36 and Fig. 37. The parametrization varies the perforation length dimension, as well as simultaneously their rotation with respect to in situ stress anisotropy. With all models maintaining the same boundary pressurization, the increase in induced displacements with perforation length is highly apparent. Those stress concentrations at the peroration tips exhibit a more subtle trend, though would indicate softening initiation in the maximum far-field stress direction.

CONCLUSION

FV-based bimaterial interface methods have been extended to quasi-static linearized poroelasticity. As interfaces of practical interest which involve sharp contrasts in the Young's modulus, sharp step changes in the displacement gradient are accounted for. Both impermeable and permeable interfaces are accounted for. The application of this method is compatible with the various coupling methods presented, which utilize both fixed-stress and fixed-strain assumptions on the coupling half-step. The entailed stress analysis is useful for various means of softening and fracturing evaluation, inclusive of phase-field approximation and cohesive-type models.

The numerical results presented also suggest appropriate best practices with respect to modeling fracture growth. It is important to note that the type and location of stress concentrations apparent in the parametric case-study presented – which do not necessarily collocate exactly with the perforation tip locations – indicates strongly a requirement for the softening model. To capture near-wellbore effects it may be desirable

to: (a) initialize damage in near-perforation regions corresponding to the physical damage from shape charges; and (b) employ a softening model independent of the numerical mesh, in order to capture breakdown in the most favorable direction and hence at the correct wellbore pressures.

Chapter 3: A finite area method for the solution of variously coupled hydraulic fracture continuity equations

The Finite Volume (FV) method is a spatial discretization for volumes (3D domains), and in the same sense the Finite Area (FA) method is a spatial discretization for surfaces (2D domains). We propose use of the FA method in order to discretize the continuity equation describing fluid flow inside hydraulic fractures. Without loss of generality, fracture growth is modeled using a CZ model and presumes use of FV-based methods to discretize the deforming and fracturing rock matrix. The constitutive relation for the rock matrix is linearized poroelasticity, with coupled Darcy-type pore fluid flow. Consequently, fracture geometry is extracted from discontinuities that evolve inside the rock, as enforced by CZ-based softening. An evolving fracture surface, fracture fluid injection, flow, and leak-off is modeled. The proposed framework is immediately extensible to small-strain poro-plasticity (having been implemented in a modular and object-oriented framework).

The FA method is a spatial discretization for 2D domains, which accounts for the effects of surface curvature on the numerical modeling of surface transport processes. FA numerics solve differential equations along surfaces discretized by arbitrary polygons. Hence, FA-modeled domains require only the positional surface data along FV domain boundaries for their discretization. Without exception, FA domain can be entirely initialized by the collection of FV cell-faces which compose a specified boundary of an arbitrary FV mesh [50, 51, 52]. Consequently for our purposes, use of the FA discretization offers a parsimonious data structure; use of FA numerics eliminates the requirement for a secondary FV mesh to compute fracture flow. Moreover, these fractures can be modeled dynamically. Dynamic growth is based upon evaluation of fracturing or softening behavior in the solid, Fig. 38. Except for dynamic growth and

geomechanical couplings, the solution of the fluid transport equation is to be considered as an extension of prior work on FA-discretized Reynolds flow [53, 54].

A significant fraction of this work deals with fracture flow solution within the CZ tip region. If not utilizing a CZ model, these sections can be disregarded. Yet in that exclusive context, separate considerations of two spatially non-overlapping fracture conservation equations is important. In particular, the conservation equation within the CZ proves critical for both physical and also numerical reasons. Firstly as to its physicality, this measure provides a description of pore fluid conservation – as the main fracture advances to encompass new boundary surface previously contained within the CZ (see [31]). Thus, it vitiates the sudden appearance of nontrivial, zero-pressure volumes during main fracture extension. Secondly as to the numerical consequences, CZ conservation encourages smooth recovery of fracture statistics like aperture (the opening width at injection location). When using a fluid-filled CZ tip, the changes in solid-boundary displacements are more monotonic during softening; because of the monotonic changes, the optimization of the linear algebraic matrix solution is more straightforward. (Less obviously, fluid-filled tip systems are additionally less dependent on mesh refinement at the fracture tip – a deciding consideration. On this point, compare [31] against [55] – the latter exhibiting jagged, mesh-dependent aperture reductions engendered by every instance of real fracture extension.) This aspect of our model follows de Borst and co-workers, where additional CZ tip physics are more comprehensively considered [56]. For a detailed description of differences between the real fracture and CZ tip region, see [38].

Essentially two leak-off models are described in this work: the gradient-based method, and the Carter model. Gradient-based methods assume continuity of flux in each iteration, and converge continuity of the pore fluid boundary and fracturing pressures in

each iteration. Gradient methods are more naturally amenable to block-coupled matrix inversion of fracturing fluid and pore pressure equations (meaning via block combination of the implicit scalar Laplacian operators for both domains). In contrast, Carter model-type leak-off decouples fracturing and pore fluid conservation equations [57]. Thus Carter models are useful in the following scenarios: (a) simulation of fracture growth in a fast, forward-marching manner; (b) capturing effects of rapidly dispersed leak-off into the far-field, in order to explain high rates of leak-off in a naturally fractured formation; (c) where pore fluid average versus fracture compressibilities differ significantly – such as during energized fracturing completion – such that an additional sub-cycling method is desirable when solving the fracture conservation equation; and, (d) where proppant models couple highly non-linear density and bridging effects. However, the Carter model implementation is natively crude, because not enforcing mass conservation into the reservoir. (Alternate mass-conserving implementations are feasible. As implemented in this work, continuity of the pore and fracturing pressures is instead preferred.)

Proppant concentrations are modeled as uncoupled scalar transport equations. Here the focus is on verification of advective transport inside the fracture. The proppant model may be extended based upon empirical and/or derived correlations based upon particle simulation [58]. For other treatment for effects of the fracture-transverse pressure gradient and where slurry effects are considered, see recent developments in [59, 60].

In the way of background, coupled fracture fluid flow and deforming solid mechanics has been solved using Reynolds flow utilizing the Finite Element (FE) method [61], showing convergence to the relevant asymptotic solutions [31]. Real-world fractures exhibit the type of complexity we are attempting to capture [62]. This document assumes a failure process within a poroelastic or poroplastic solid domain as outlined in Fig. 39.

MATHEMATICAL MODELS

The continuity equation for fluid flow inside a fracture is stated as a surface integral formulation. A separate equation of continuity is stated for fluid flow inside a CZ. The latter equation accounts for porosity effects within the softening zone. Pressures across the width of the fractured and fracturing discontinuity can be assumed constant for the purpose of modeling slit flow.

Fracture continuity equation

Consider flow within a fracture assuming small variations in fluid density. A cubic law flow can be considered as an integral of fluid volume change in response to change in pressure, change in a volume V, and volumetric fluxes in and out. With the assumption of small changes in fluid density, the strong integral form of the isothermal flow equation becomes:

$$\int_V [\frac{1}{K^f}\frac{\partial p^f}{\partial t} + \frac{1}{V}\frac{\partial V}{\partial t}]\mathrm{d}V = -\oint_S \mathbf{n}\cdot\mathbf{q}\mathrm{d}S + Q \quad (107)$$

where K is the bulk modulus, p the pressure, t time, $\mathbf{n}$ the surface normal vector, $\mathbf{q}$ the flux, V the volume, S the surface, and Q the volumetric rate of production; superscripting f indicates a variable or property of the fracturing fluid.

In order to apply FA-based numerics, the fracture fluid flow must be considered as though along a surface - and hence not within a series of control volumes. Therefore the volume is decomposed: $V = Sw$ for S the invariant surface area and w the fracture width. (The nature of the control surface S is a discontinuity in the rock or other solid domain, and we suppose that the location of the solid's boundary is known. In this work the bounding solid is assumed to deform under a small-strain assumption. Therefore all

discretized S are constant in time and hence "invariant.") In this manner, we can define the evolved fracture surface as the discontinuity exposed by deformation and failure of a bounding solid. But, the fracture surface is inherently dual – in that each fracture face has an opposite or "shadow" surface from which it was detached during deformation. The current and shadow faces are "twins", in that they possess exactly the same shape and lie in the same plane, and at a state of zero deformation would be co-located. (As later discretized, the twin surface is marked by subscripting sP).

Thus, the current fracture width w is defined between any face and its shadow face. The associated substitutions for $V = Sw$ return:

$$\int_S [\frac{1}{K^f}\frac{\partial p^f}{\partial t} + \frac{1}{Sw}S\frac{\partial w}{\partial t}]w\mathrm{d}S = -\oint_{\partial S} \mathbf{m} \cdot (\int_0^w \mathbf{q})\mathrm{d}L + Q \quad (108)$$

where $\mathbf{m}$ is the edge bi-normal vector. A tensorial fracture transmissivity $\mathbf{K}^f$ associated with flow down the fracture is assumed. However, in the direction transverse to flow – approximately $\mathbf{n}_P$ with as numerical mesh fining increases – it is $\mathbf{n}_P \cdot (\mathbf{n}_P \cdot \mathbf{K}^f) \to \infty$. Consequently when modeling axial flow, $\mathbf{K}^f$ is replaced by scalar k^f. In this sense axial flux is:

$$\mathbf{q} = -\frac{k^f}{12\mu^f}\nabla_s p^f \quad (109)$$

where the physical units of k^f are in squared length. The above Darcy-type constitutive relation is substituted in Eq. (108). Further, we assume uniformity of pressure gradient over the width of the fracture control surface's edges. Also, the substitution is made that $w \to w/2$, in order to represent the constraint that each half-side of the fracture only captures half of the width,

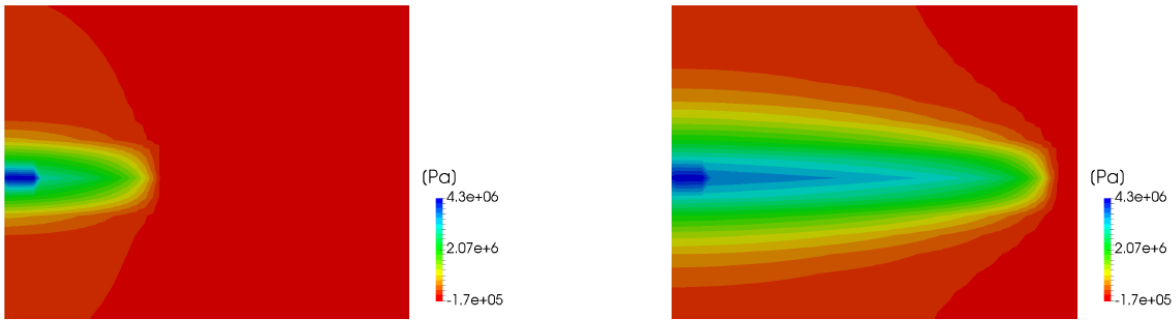

(a) (b)

Figure 38: Coupled, dynamically grown fracture (a) at early time, and (b) bigger at later time.

$$\int_S [\frac{w}{K^f}\frac{\partial p^f}{\partial t} + \frac{\partial w}{\partial t}]\mathrm{d}S = \oint_{\partial S} \mathbf{m} \cdot (w\frac{k^f}{12\mu^f}\nabla_s p^f)\mathrm{d}L + 2Q. \quad (110)$$

In the above continuity equation, the strain can be recognized by normalization of all terms by width coefficient-w – such that the equation's terms possess units of reciprocal time. For that normalization, the appearance of term $(1/w)(\partial w/\partial t)$ would represent the approximate temporal derivative of engineering strain. Clearly then, all appearances of the coefficient-w in Eq. (110) must be all identically valued (at any particular time), to promote consistency.

Tip continuity equation

With the assumption of small changes in fluid density, the strong integral form of the isothermal CZ flow equation becomes:

$$\int_V [\frac{1}{M^c}\frac{\partial p^f}{\partial t} + \frac{b^c}{V}\frac{\partial V}{\partial t}]\mathrm{d}V = -\oint_S \mathbf{n} \cdot \mathbf{q}\mathrm{d}S + Q, \quad (111)$$

where M is the Biot's modulus, and b the Biot's coefficient – as computed for the deforming poroelastic solid. The above conservation equation recognizes the compatibility relating deformation of the skeletal pores to the volume occupied by pore fluid within a softening region. Making identical substitutions as produce Eq. (110):

$$\int_S [\frac{w}{M^c}\frac{\partial p^f}{\partial t} + b^c\frac{\partial w}{\partial t}]\mathrm{d}S = \oint_{\partial S} \mathbf{m}\cdot(w\frac{k^f}{12\mu^f}\nabla_s p^f)\mathrm{d}L + 2Q. \quad (112)$$

In regard to (solid) boundary displacements and values, the deforming poroelastic solid is solved using the "over-relaxed" approach for linear elasticity [15] as extended to poroelasticity [20], with softening behavior evaluated as in [16] and extended to multi-material elasticity with softening in [11, 30]. The approach to enforcing boundary gradients of strain is the same as in [18].

Proppant advection

After normalization by density, the proppant mass balance inside the fracture can be simplified as an advection equation with use of semi-empirically determined internal coefficients of the divergence. The identical change in fracture volume approximation (with respect to the temporal derivative) is applied as in Eq. (107):

$$\int_V [\frac{\partial c}{\partial t} + \frac{c}{V}\frac{\partial V}{\partial t}]\mathrm{d}V = -\oint_S \mathbf{n}\cdot(c\mathbf{q}^{\mathrm{p}})\mathrm{d}S + C^{\mathrm{p}}, \quad (113)$$

where c is concentration, and source term C^{p}. (The complete advection-diffusion equation is straightforward to implement; however, our concentration equation is constrained to follow the reduced system in [58].) It is anticipated that the condition for proppant concentration injection is: fixed-value at boundary inlets, and zero-gradient at

any outlets. According to the Darcy constitutive relation as above, the proppant velocity is:

$$\mathbf{q}^{\mathrm{p}} = \mathbf{A}^{\mathrm{p}}\mathbf{q} + \mathbf{b}^{\mathrm{p}} \quad (114)$$

where both coefficients are empirical relations, $\mathbf{A}^{\mathrm{p}}(w)$ and $\mathbf{b}^{\mathrm{p}}(w, \rho)$ for ρ indicating the set of density effects. As above, substitutions are made for the invariant surface, and letting $w \to w/2$:

$$\int_S [\frac{\partial c}{\partial t} + \frac{cS}{S(w/2)}\frac{\partial (w/2)}{\partial t}](\frac{w}{2})\mathrm{d}S = -\oint_{\partial S} \mathbf{m} \cdot (c\int_0^{w/2} \mathbf{q}^{\mathrm{p}})\mathrm{d}L + C^{\mathrm{p}}. \quad (115)$$

Again, the flow velocities $\mathbf{q}^{\mathrm{p}}$ of proppant transport containing empirical relations are considered to be invariant across the width. Then cancellation returns simply

$$\int_S [w\frac{\partial c}{\partial t} + c\frac{\partial w}{\partial t}]\mathrm{d}S = -\oint_{\partial S} \mathbf{m} \cdot (wc\mathbf{q}^{\mathrm{p}})\mathrm{d}L + 2C^{\mathrm{p}}. \quad (116)$$

Clearly density effects of the slurry as effects the flow model are neglected (as relates to Eq. (110)).

NUMERICAL DISCRETIZATION

Volumetric domains presented in this work are discretized using the FV method. Temporally, the total simulation time is split into a finite number of time steps Δt not necessarily of uniform period. Spatially, the domain is decomposed into a finite number of non-overlapping polyhedral control volumes (cells), bounded by flat polygons (faces) here also assumed to be convex. A representative numeric control volume V_P is presented in Fig. 20, showing: the location of centroid P located in the global coordinate system by

vector $\mathbf{r}_P$; and, the location of the centroid N of a neighboring control volume located at a distance from P described by vector $\mathbf{d}_f$. The cell boundary associated with centroid-to-centroid vector $\mathbf{d}_f$ is face f is of area S_f, the plane of which is described by surface normal $\mathbf{n}_f$ as originates from the centroid of the face.

Surface domains presented in this work are discretized using the FA method. For this work, the same time step Δt is used on surface domains (although not required). A representative numeric control area S_P is presented in Fig. 40, showing: the location of area centroid P, with surface normal $\mathbf{n}_P$ extending from that centroid; similarly for a neighboring control area centered N and surface normal $\mathbf{n}_N$; edge vector $\mathbf{e}$ connecting vertices of the control area i to j; vertex normal $\mathbf{n}_i$ of vertex i; the edge normal $\mathbf{n}_e$ originating from the center of the associated edge. Fig. 40 also indicates identities of the spatial discretization, showing: edge length L_e; distance vector $\mathbf{d}_e$ with magnitude of the euclidean distance between P and N, utilized in interpolation functions; and, the bi-normal me perpendicular to $\mathbf{n}_e$ and $\mathbf{e}$, depicted as originating from the center of edge e. Construction of the bi-normals at fracture tips provides for a limiting case of the FA discretization. Every bi-normal is defined as a vector perpendicular to both (a) the averaged point normals of points along the edge, and (b) the edge. Each vertex normal $\mathbf{n}_i$ is computed using a weighted average of the cross product vectors constructed using the edges connected to the point. By geometric argument for each fracture tip vertex, the summation to compute $\mathbf{n}_i$ will contain an equal number of opposite cross-product vectors. This observation follows from: (a) symmetric connectivity of edges around tip vertices; and, (b) the small-strain assumption which does not permit computational mesh deformation during fracture opening. In this event, the summation of those equal and opposite vectors is not normalized, such that $\mathbf{n}_i = \mathbf{0}$ for any vertex along the fracture tip. By eventual geometric arguments, it follows that the net effect is the imposition of zero-

gradient boundary conditions at the fracture tip – in the bi-normal direction (the product with $\mathbf{m}_e = \mathbf{0}$ is also 0 for all spatial operators). The consequence that the Neumann condition at the tip is imposed purely by the procedure of discretization, was one of the most surprising and interesting aspects of executing this work.

Fracture coupling splits

To define the implicit component of the pore fluid spatial equation discretization – a Laplacian operator with spatially variable internal coefficients – let us define:

$$\mathcal{L}_s(p^f) \equiv \sum_e (\mathbf{m} \cdot (w^{n*} \frac{(k^f)^\theta}{12\mu^f} \nabla_s (p^f)^n))_e L_e + \sum_b (\mathbf{m} \cdot (w^{n*} \frac{(k^f)^\theta}{12\mu^f} \nabla_s (p^f)^n))_b L_b \,, \quad (117)$$

where $\mathcal{L}_s(p^f)$ is a convenience term; subscripting e and b represents internal edge-center values. The coefficient-w width term in above will may be taken as w^{n*}; superscript $n*$ indicates a value which may be derived from prior time step – consonant with the engineering definition of strain.

Fixed-strain width

For a fixed-strain split poroelastic coupling, the discretization of the fracture pressure flow equation is,

$$\mathcal{L}_s(p^f) + 2Q_P = [\frac{w_P^{n*}}{K^f} (\frac{(p^f)_P^n - (p^f)_P^o}{\Delta t}) + \frac{w_P^n - w_P^o}{\Delta t}] S_P. \quad (118)$$

Here, subscript P represents face-center values. Superscripts n, o, and oo represent the current t^n, previous t^o, and previous to previous t^{oo} time instances. For $Q_P = 0$ this discretized equation: (a) would not handle intersections; (b) assumes flow to proceed

entirely along one fracture surface; and, (c) cannot provide for leak-off. The opening width between current face S_P and twin shadow face S_{sP} is recovered as:

$$w_P = \mathbf{n}_b \cdot (\mathbf{u}_{sb} - \mathbf{u}_b), \quad (119)$$

where subscript b indicates a boundary value of the FV domain at face-center P, and sb a boundary value at shadow face-center sP. Thus the above indicates that width is defined as the magnitude of normal displacement between the centroids of the twin faces, in the direction normal to the face.

Fixed-stress width

For a fixed-stress split poroelastic width coupling, the appropriate pressure-response coefficient has been investigated previously [45]. In essence, the mean stress is held constant during the coupling half-step. The discretization of the fracturing pressure inside our flow equation is:

$$\begin{aligned} \mathcal{L}_s(p^f) + 2Q_P \quad = \quad & [w_P^{n*}(\frac{1}{K^f} + \gamma^f)(\frac{(p^f)_P^n - (p^f)_P^o}{\Delta t}) + \frac{w_P^n - w_P^o}{\Delta t}]S_P \\ & -[w_P^{n*}\gamma^f(\frac{(p^f)_P^{i_{\mathbf{u}}} - (p^f)_P^o}{\Delta t})]S_P, \end{aligned} \quad (120)$$

where γ^f is a constant related to the domain properties. This method improves the approximation within the pressure equation of poroelastic effects, and as such that constant may vary based upon constraints and compatibility of the modeled problem. For all examples presented where a fixed-stress width-split is used, then exactly:

$$\gamma^f = \frac{1}{K^f(\beta\lambda - 1)}, \quad (121)$$

$$\beta = \frac{1}{Mb^2} + \frac{1}{b^2}(\frac{b^2}{\lambda}). \quad (122)$$

Superscript $i_{\mathbf{u}}$ indicates the immediately prior coupling iteration within the same time step, in which the displacement was fully converged. The last parameter (b^2/λ) is an independent parameter derived from compatibility analysis of the poroelastic loading. It is to be as used in fixed-stress split $\mathbf{u}-p$ coupling – i.e. valued as within the solid.

Explicit fixed-stress

The solution approach taken below is by analogy to a fixed-stress split explicit-in-time poroelastic $\mathbf{u}-p$ coupling of quasi-static poroelasticity. The time derivative of width is resolved as an explicit term plus a function of the fracturing pressure in the present iteration,

$$\begin{aligned}\frac{\partial(w)^n}{\partial t} &\approx \frac{\partial(w)^o}{\partial t} + w_P^o\gamma^f\frac{\partial((p^f)^n-(p^f)^o)}{\partial t},\\ &= \frac{w_P^o - w_P^{oo}}{\Delta t} + w_P^o\gamma^f[(\frac{(p^f)_P^n-(p^f)_P^o}{\Delta t}) - (\frac{(p^f)_P^o-(p^f)_P^{oo}}{\Delta t})]. \quad (123)\end{aligned}$$

For a fixed-strain width-split, discretization of the continuity equation returns,

$$\begin{aligned}\mathcal{L}_s(p^f)+2Q_P &= [\frac{w_P^o}{K^f}(\frac{(p^f)_P^n-(p^f)_P^o}{\Delta t}) + \frac{w_P^o-w_P^{oo}}{\Delta t}]S_P\\ &\quad +[w_P^o\gamma^f\Delta t(\frac{(p^f)_P^n-2(p^f)_P^o+(p^f)_P^{oo}}{(\Delta t)^2})]S_P. \quad (124)\end{aligned}$$

Under this iterative strategy, given sufficiently small time steps, the displacement field and fracture continuity equations can be decoupled excepting evaluation of fracture growth and consequent permeability enhancement. If fracturing processes initiate, then further fracturing may occur within the same time step. Thus, still within the explicit time-marching formulation, but subsequent to fracture to fracture growth the approximation becomes:

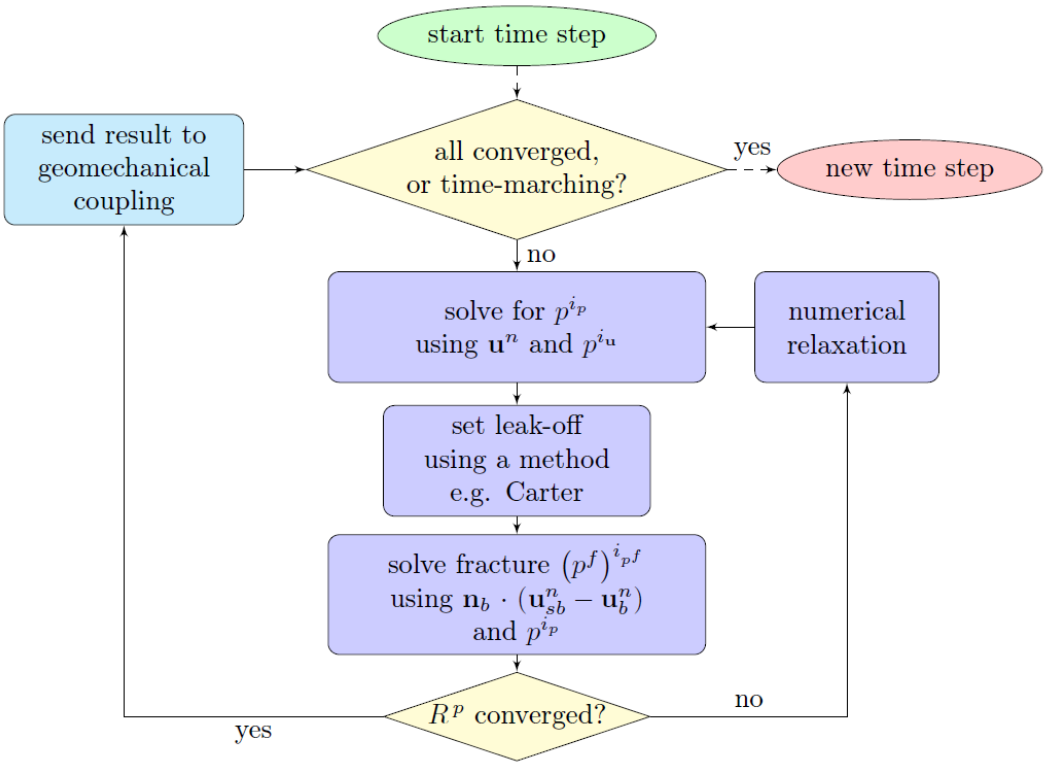

Figure 39: Flow chart of coupling logic: relating pore pressure and fracture flow systems, after [63].

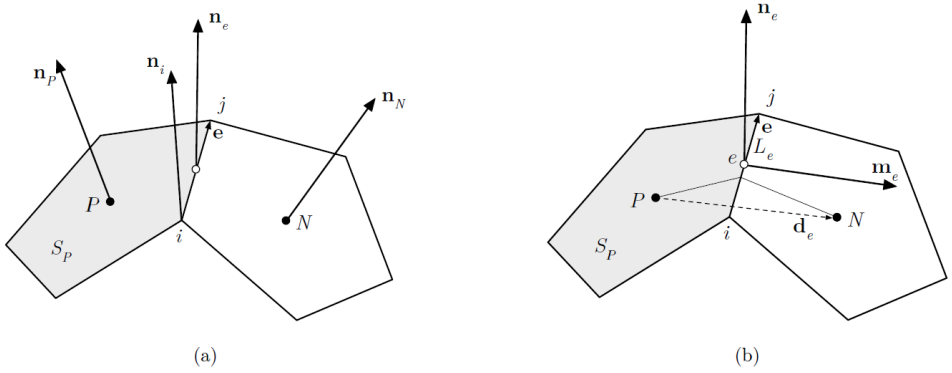

Figure 40: Polygonal control area with (a) area and point normals, and (b) bi-normal, after [50].

$$\frac{\partial(w)^n}{\partial t} \approx \frac{\partial(w)^n}{\partial t} + w_P^{n*}\gamma^f \frac{\partial((p^f)^n - (p^f)^{i_u})}{\partial t},$$
$$= \frac{w_P^n - w_P^o}{\Delta t} + w_P^{n*}\gamma^f[(\frac{(p^f)_P^n - (p^f)_P^o}{\Delta t}) - (\frac{(p^f)_P^{i_u} - (p^f)_P^o}{\Delta t})]. \quad (125)$$

Discretization of the flow equation returns,

$$\mathcal{L}_s(p^f) + 2Q_P = [\frac{w_P^{n*}}{K^f}\frac{(p^f)_P^n - (p^f)_P^o}{\Delta t} + \frac{w_P^n - w_P^o}{\Delta t}]S_P$$
$$+[w_P^{n*}\gamma^f(\frac{(p^f)_P^n - (p^f)_P^o}{\Delta t}) - w_P^{n*}\gamma^f(\frac{(p^f)_P^{i_u} - (p^f)_P^o}{\Delta t})]S_P. \quad (126)$$

Thus the result of Eq. (120) is recovered, here with effect for explicit time-marching. Eq. (126) can be iterated over within the same time step, until softening processes no longer initiate.

TIP COUPLING SPLITS

The discretized form of the tip continuity equation differs from the one used inside the fracture – but not by the form of the implicit Laplacian linear operator (although its internal coefficients may spatially vary). Simply put, the continuity equation varies to recognize that CZ-tip flow occurs through debonding pore space. This result can be adduced by stress analysis – and hence only effects face-center value coefficients utilized like the porelastically-coupled modulus of compressibility or tangent modulus of strain with respect to porosity.

Fixed-strain width

For a fixed-strain split poroelastic coupling, the discretization of the tip flow equation is:

$$\mathcal{L}_s(p^f) + 2Q_P = [\frac{w_P^{n*}}{M_P^c}(\frac{(p^f)_P^n - (p^f)_P^o}{\Delta t}) + b_P^c \frac{w_P^n - w_P^o}{\Delta t}]S_P. \quad (127)$$

where the result that Biot's modulus in the cohesive region M^c is $M^c(K^f)$, e.g., cannot be extracted from J-integral analysis of the fracture tip.

Fixed-stress width

The pressure-response coefficient appropriate inside the cohesive zone is obtained by (easy) visual inspection of the previous investigation [45]. While the mean stress is constant during the half-step, simple adjustment is made for multiplication into the strain derivative of the Biot's coefficient. The discretization of the pore pressure inside our flow equation is:

$$\begin{aligned}\mathcal{L}_s(p^f) + 2Q_P \quad = \quad & [w_P^{n*}(\frac{1}{M_P^c} + \gamma_P^{cf})(\frac{(p^f)_P^n - (p^f)_P^o}{\Delta t}) + b_P^c \frac{w_P^n - w_P^o}{\Delta t}]S_P \\ & -[w_P^{n*}\gamma_P^{cf}(\frac{(p^f)_P^{i_{\mathbf{u}}} - (p^f)_P^o}{\Delta t})]S_P, \end{aligned} \quad (128)$$

where the CZ coefficient is:

$$\gamma^{cf} = \frac{1}{M^c(\beta(\lambda/b^c) - 1)}, \quad (129)$$

where λ/b^c is a physical parameter and unrelated to the poroelastic fixed-stress coefficient b^2/λ. In fact hhe effects of b^2/λ are contained in β. Other methods for fully explicit, time-marching schemes can be straightforwardly adduced from Eq. (124) and Eq. (126).

VOLUMETRIC FLOWS AND BOUNDARY GRADIENTS

Injection rates applied as fluid fluxes in the longitudinal direction of the fracture are applied as Neumann conditions along the FA mesh edges. However, both leak-off and correction terms are not naturally discretized by FA spatial operators. Hence, they are both applied as source terms within the discretized equation (meaning the terms contribute to Q_P, the face-centered discretization of volumetric production).

Leak-off term

The FA method offers no discretized boundary in the direction normal to a fracture face, by which to convey leak-off from the fracture into the formation. Fortunately none is required. Also, our definition of leak-off as a volumetric source term maintains the assumption of a zero pressure gradient over the width of the fracture (infinite transverse fracture permeability). This source term is applied to the volume discretized by the control surface of the fracture.

Gradient discharge

To couple the fracture and pore fluid systems, it is assumed that the total discharge (of leak-off) leaving the fracture is equal to the rate of fluid entering the porous material. Hence by Darcy's law, the normal flux q_{bn} of fluid entering the porous boundary is a function of the gradient of pressure along the fracture boundary,

$$q_{bn} = -(\mathbf{n} \cdot \frac{k_{pbn}}{\mu_p} \nabla p)_b \quad (130)$$

where subscript b indicates a boundary value on the solid. So, the volumetric leak-off is applied to the discretized equation as:

$$Q_{leak}^{n} = q_{bn}^{n} S_P = -(\mathbf{n} \cdot \frac{k_{pbn}}{\mu_p} \nabla p)_b^n S_P \quad (131)$$

emphasizing that $\mathbf{n}_b$ has the opposite orientation as $\mathbf{n}_P$. (So that $\mathbf{n}_b = -\mathbf{n}_P$, where the surface normal $\mathbf{n}_P$ is a fictitious outward normal of area S_P.)

Carter discharge

Use of the Carter model represents application of the analytic solution for 1D, single-phase isothermal diffusion from the fracture into the formation. All material properties are assumed to be homogeneous; effects of poroelasticity are not accounted for. Factors such as fracture wall build-up of plugging fines may be included (for an overview of production estimations, c.f. [64]). The model presented here differs from the classical application on one or two manners. First, to make some accommodation for coupled poroelasticity the Biot's modulus rather than the single-phase compressibility is substituted (c.f. [65]),

$$C_{leak} = \sqrt{\frac{\phi_b^0 k_{pbn}}{\pi M_b \mu_p}} \quad (132)$$

where ϕ^0 is the porosity. Furthermore, accuracy of the classical Carter model is enhanced by the presence of high far-field stresses (above in situ pore pressures in the formation). This is because the volume of leak-off is taken to depend upon a known, time-invariant pressure inside the fracture. For small apertures, this value would be approximately the resolved stress component: $S_{bn}^0 = \mathbf{n}_b \cdot (\mathbf{n}_b \cdot \mathbf{S}_b^0) < 0$ (TENSION POSITIVE), neglecting poroelastic back-stress on the fracture boundary. The Carter leak-off term would then be:

$$Q_{leak}^{n} = q_{bn}^{n} S_P = C_{leak}\left(\frac{S_{bn}^{0} + p_b^{0}}{\sqrt{t^* - t^{0c*}}}\right) S_P = -\left(\frac{C_{leak}^{*}}{\sqrt{t^* - t^{0c*}}}\right) S_P \quad (133)$$

where p^0 represents the undisturbed in situ pore pressure at exactly the fracture boundary, and superscripting $0c*$ marks when cohesive processes completed. For the discretized time step, this is approximated as $t^{0c*} = t - \Delta t$ in order to provide consistency with surfaces initialized at zero-time for which $t^{0c*} = 0$. In order to apply a central approximation, in Eq. (133) and later Eq. (134) the time term is then $t^* = t - (\Delta t/2)$. If including CZ tip leak-off, then let $t^{0c*} \to t^{0c}$, where superscripting $0c$ marks when cohesive processes initiated. Finally we note, term $C_{leak}^{*} > 0$ represents the classical Carter coefficient of production engineering practice.

Implicit Carter discharge

Second instead of the analytic approximation – which relies on a time-invariant pressure drop from the fracture to the far-field – the current fracturing pressure is used (at all times). Altogether contributing both implicit and explicit terms, the Carter discharge is then:

$$Q_{leak}^{n} = q_{bn}^{n} S_P = -C_{leak}\left(\frac{(p^f)_P^n - p_b^0}{\sqrt{t^* - t^{0c*}}}\right) S_P. \quad (134)$$

It may be preferable to exclude leak-off effects from the CZ tip, or a mix of methods such that the gradient method or zero-gradients are locally applied within that zone. (In other words, differing leak-off models in the real fracture and in the CZ are viable, even where the CZ is solved as fluid-filled.) Further, neither the fixed-stress nor the fixed-strain coupling split discussed predicate a leak-off model – or even the

continuity of flux. Thus all leak-off models presented may be applied in conjunction with any combination of reservoir and fracture coupling splits.

Permeabilities

The fracture width for any control surface is defined as above to be w_e^θ, which may differ from the Eulerian distance $\overline{LPsP}$ between centroid of control surface area S_P and shadow control surface area S_{sP}. Fracture transmissivity is based on the width w_e^θ; however, differing from the mass-conserving fracture width, for numerical stability some limiting positive value may be applied to the permeability-coupling width, such that,

$$(k^f)_e^\theta = (w_e^\theta)^2 \quad (135)$$

where superscripting θ indicates use of the theta method. The purpose is to eliminate non-linearity during the converging time-step. However, as stated above, the Laplacian term of Eq. (117) acts only along each side of the fracture. In that we correct for this effect: the axial-directional permeability is utilized to scale transverse fluxes, as below.

Edge boundary gradients

Fixed injection rate boundaries provide axial inlet fluxes for injection of fluid into the fracture. As describing the entry flux, the fixed volumetric rates constitute a Neumann boundary condition. The edge normal gradient of fracture pressure $\mathbf{m}_b \cdot (\nabla_s p^f)_b$ is set as a function of rate, total area of current aperture, and the constitutive relation describing flux. For a set volumetric injection rate Q_{inj}, it is assumed that boundary flux q_{bm} is equal for each edge along the inlet. Hence by continuity:

$$q_{bm} = -\frac{Q_{inj}}{\sum_b (\frac{w}{2})_b^{n^*} L_b} = \mathbf{m}_b \cdot (-\frac{k^f}{12\mu^f} \nabla_s p^f)_b \quad (136)$$

Re-arranging the Darcy constitutive equation:

$$\mathbf{m}_b \cdot (\nabla_s p^f)_b^n = (-\frac{12\mu^f}{k^f} q)_{bm}^n = (\frac{12\mu^f}{k^f})_b^\theta [\sum_b (\frac{w}{2})_b^{n*} L_b]^{-1} Q_{inj}^n \quad (137)$$

where subscripting bm indicates an edge-boundary value in the edge bi-normal direction. Above, as with Eq. (110), it is assumed that fracture pressure gradient is constant across the transverse width. This method for setting boundary gradients has been described for a FV-discretized fracture in [39].

MATRIX ASSEMBLY

The details of the discretized equation may vary based upon the coupling split chosen. For example, the field equation inside the fracture is assembled:

$$\mathcal{L}_s(p^f) + 2Q_{corr} + 2Q_{leak} = [\frac{w_P^{n*}}{K^f} (\frac{(p^f)_P^n - (p^f)_P^o}{\Delta t}) + \frac{w_P^n - w_P^o}{\Delta t}] S_P \quad (138)$$

where the example of fixed-strain width split is provided, and the substitution $Q_P = Q_{corr} + Q_{leak}$ is made. In the above equation, coefficient 2 in $2Q_{corr}$ is arbitrary but included for consistency.

Gradient model/fixed-strain width

Presume that no fracturing/pore pressure continuity is enforced at the fracture tip, and that a gradient-based leak-off method is utilized. The fully discretized form of the fixed-strain fracture pressure equation is:

$$
\begin{aligned}
0 \quad = \quad & -(H_s^n)[\frac{w_P^{n*}}{K^f}(\frac{(p^f)_P^n-(p^f)_P^o}{\Delta t})+\frac{w_P^n-w_P^o}{\Delta t}]S_P \\
& -(1-H_s^n)[\frac{w_P^{n*}}{M_P^c}(\frac{(p^f)_P^n-(p^f)_P^o}{\Delta t})+b_P^c\frac{w_P^n-w_P^o}{\Delta t}]S_P \\
& +\sum_e(\mathbf{m}\cdot(w^{n*}\frac{(k^f)^\theta}{12\mu^f}\nabla_s(p^f)^n))_eL_e \\
& +\sum_b(\mathbf{m}\cdot(w^{n*}\frac{(k^f)^\theta}{12\mu^f}\nabla_s(p^f)^n))_bL_b \\
& +2\alpha_{cor}\sum_{i_{pf}}[w_P^{n*}\frac{(k^f)_P^\theta}{12\mu^f}((p^f)_{sP}^{i_{pf}}-(p^f)_P^{i_{pf}})] \\
& -2(H_s^n)[(\mathbf{n}\cdot\frac{k_{pbn}}{\mu_p}\nabla p)_b^n]S_P, \qquad (139)
\end{aligned}
$$

where H_s is a unit step function of fracture surface (s) that is 1 in the fracture and 0 in the CZ. Note when comparing with above, $Q_{leak} < 0$ expresses outflow from the fracture into the formation.

Carter model/fixed-stress width

Presume that no pore pressure continuity is enforced at the fracture tip, and that the explicit Carter model leak-off is utilized. The fixed-stress split equation is cleaned into:

$$
\begin{aligned}
0 \quad = \quad & -(H_s^n)[w_P^{n*}(\frac{1}{K^f}+\gamma^f)(\frac{(p^f)_P^n-(p^f)_P^o}{\Delta t})]S_P \\
& -(H_s^n)[\frac{w_P^n-w_P^o}{\Delta t}-w_P^{n*}\gamma^f(\frac{(p^f)_P^{i_{\mathbf{u}}}-(p^f)_P^o}{\Delta t})]S_P \\
& -(1-H_s^n)[w_P^{n*}(\frac{1}{M_P^c}+\gamma_P^{cf})(\frac{(p^f)_P^n-(p^f)_P^o}{\Delta t})]S_P \\
& -(1-H_s^n)[b_P^c\frac{w_P^n-w_P^o}{\Delta t}-w_P^{n*}\gamma_P^{cf}(\frac{(p^f)_P^{i_{\mathbf{u}}}-(p^f)_P^o}{\Delta t})]S_P \\
& +\sum_e(\mathbf{m}\cdot(w^{n*}\frac{(k^f)^\theta}{12\mu^f}\nabla_s(p^f)^n))_eL_e \\
& +\sum_b(\mathbf{m}\cdot(w^{n*}\frac{(k^f)^\theta}{12\mu^f}\nabla_s(p^f)^n))_bL_b \\
& +2\alpha_{cor}\sum_{i_{pf}}[w_P^{n*}\frac{(k^f)_P^\theta}{12\mu^f}((p^f)_{sP}^{i_{pf}}-(p^f)_P^{i_{pf}})] \\
& -2(H_s^n)[\frac{C_{leak}^*}{\sqrt{t-(\Delta t/2)-t^{0c*}}}]S_P
\end{aligned}
\tag{140}
$$

where $C_{leak}^* > 0$ is a time-invariant leak-off coefficient.

Proppant concentration

The cell center flux quantity $\mathbf{q}_P^{\mathrm{p}}$ is written as:

$$
(\mathbf{q}_P^{\mathrm{p}})^n = -(\mathbf{A}_P^{\mathrm{p}})^n(\frac{(k^f)^\theta}{12\mu^f}\nabla_s(p^f)^n)+(\mathbf{b}_P^{\mathrm{p}})^n. \tag{141}
$$

In numerical practice, the interpolation scheme for the internal coefficient of the Laplacian in Eq. (117) is to be consistent as applies to the Darcy constitutive relation in above equation. The proppant concentration is discretized, with the second right-hand-side term accounting for volumetric deformation:

$$[w_P^{n*}(\frac{c_P^n - c_P^o}{\Delta t}) + c_P^{n*}(\frac{w_P^n - w_P^o}{\Delta t})]S_P = -\sum_e (\mathbf{m} \cdot (w^{n*} c^n (H_s^n)(\mathbf{q}^{\mathrm{p}})^n))_e L_e \,. \quad (142)$$

The slurry's coupling, density and fracture permeability effects are neglected, as relates to Eq. (110). The above left-hand-side, second term may be made explicit by neglecting of small terms (indicated by superscripting $n*$ on c_P^{n*}). The coefficient-w width term in above (w^{n*}) is identically that of Eq. (117). The numerical scheme associated with the divergence term (right-hand-side) is upwinded on term $(\mathbf{m} \cdot (\mathbf{q}^{\mathrm{p}})^n)_e$. The proppant transport equation can be corrected for the identity of fracture-transverse concentrations, and by using nearly identical numerical methods used to establish continuity of pressure across the width (see appendix).

System residual

In general, the residual definitions used to assess convergence of field equations converged inside the bounding porous domain are inherited from the OpenFOAM variant foam-extend linear solvers [14, 44]. In general, the solution residual of fracturing pressures is assessed by perturbation of the pore pressure solution and hence by its residual. (Exceptional cases are explicit, forward-marching strategies.) But, the description of residuals is complex, because four types of residuals are employed in this work.

The first type of residual is associated with the (presumed iterative) linear solver. Generally the unknowns correspond to cell-center values, marked by subscript P. Let us suppose the pore pressure p is the unknown being converged. This field is considered as the vector $[p]$ containing the set of p_P. For the system $[A][p] = [r]$, the linear algebraic solution matrix is $[A]$. Matrix $[A]$ contains diagonal cell-centered implicit coefficients a_P

and off-diagonal coefficients a_N. The source vector is $[r]$, containing source terms r_P . For the linear system as below, the residual $(R^p)^{i_l}$ is defined as:

$$[A][p] = [r], \qquad (R^p)^{i_l} = [\frac{\sum_P \|[r] - [A][p]\|}{\sum_P (\|[A][p] - [A][\bar{p}]\| + \|[r] - [A][\bar{p}]\|)}]^{i_l}. \quad (143)$$

where $[\bar{p}]$ indicates averaging over the domain, and superscripting i_l indicates the linear solver iteration. In contrast, superscripting i_p marks the previous converged linear solver solution of the $[p]$ unknowns; superscripting n marks the current converged linear solver solution. In above equation, vector $[r]$ is a source term and unrelated to the position in the global coordinate system.

The second type of residual is the so-called "initial residual," which simply captures R^p as satisfies $[A][p] = [r]$, before beginning to converge the linear solver, such that:

$$R^p = (R^p)^{i_l=0}. \quad (144)$$

Thus R^p measures convergence of previously converged $[p]^{i_p} = [p]^{i_l=0}$, with respect to updates of matrix $[A]^{i_l}$ and source term $[r]^{i_l}$. $[A]^{i_l}$ and $[r]^{i_l}$ can vary from the values used in ip, e.g. because of inlet boundary conditions (or, within the fracture, because of width changes). Hence R^p measures converge of non-linear or coupling terms, and hence all terms not implicit in $[A]$. The third type of residual or "relative residual" test for slow change in the solution variable:

$$R^p_{rel} = \frac{\max|[p]^n - [p]^{i_p}|}{\max|[p]^n - [p]^o|}, \quad (145)$$

where superscripting n and o indicates current converged and previous time step values. The relative residual is therefore a test of small perturbations of current vs. previous time step solution, with respect to the currently converged unknown.

In the general sense, our systems of coupled partial differential equations (such as pore fluid and skeletal displacement) are simultaneously converged using fixed-point Picard iterations (with consecutively executed linear solver iterations). Hence, thus the coupled system converges as both R^p and $R^{\mathbf{u}}$ converge, or both R^p_{rel} and $R^{\mathbf{u}}_{rel}$ converge. But in the exceptional case, the fourth type of residual considers coupled systems that are not simultaneously converged. In this last case, a coupling loop must be defined in terms of the unknowns' compatibility relation. For hydromechanically coupled simulations – i.e. where using an iteratively-coupled, fixed-stress split – this last residual will be of type $R^{\phi*}$. Here the compatibility relation is expressed in terms of ϕ^*, for ϕ^* the density-normalized variation in fluid mass content [46]. Under this scenario, the coupling residual $R^{\phi*}$ is absolutely required: both R^p and $R^{\mathbf{u}}$ are ipso facto converged at the end of any field-coupling loop, and do not signify as to the mutual compatibility of the p and $\mathbf{u}$ field solutions.

Specifically in this work, the FA solution is converged as it effects the boundary values of pore pressure p, as follows [63]. Therefore the residual used for p^f in p-coupled models is R^p. For a fixed-strain formulation, the convergence criteria is simultaneous R^p and $R^{\mathbf{u}}$ below tolerances. For a fixed-stress formulation, the convergence criteria is $R^{\phi*}$ below the tolerance.

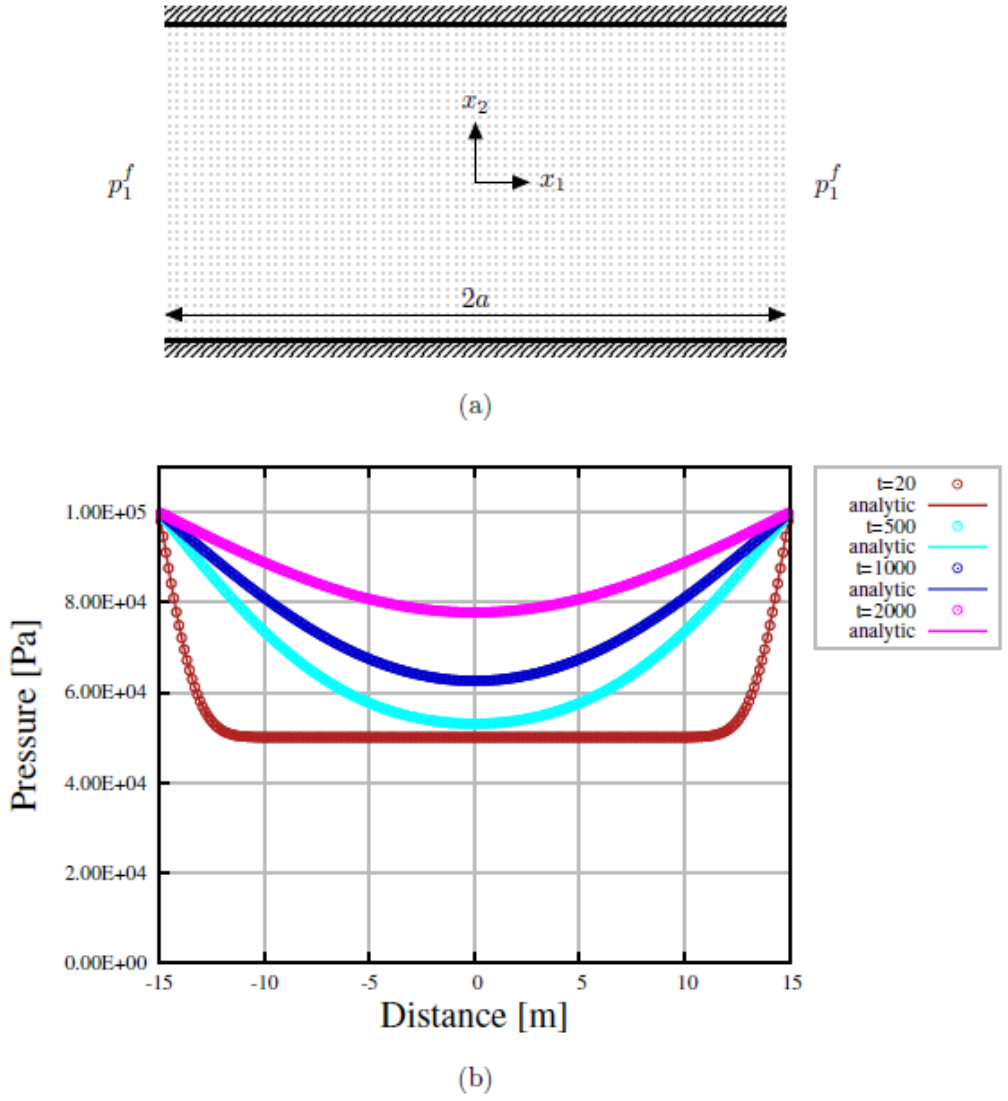

Figure 41: Finite slab fixed-value test case with (a) loading, and (b) pressure results.

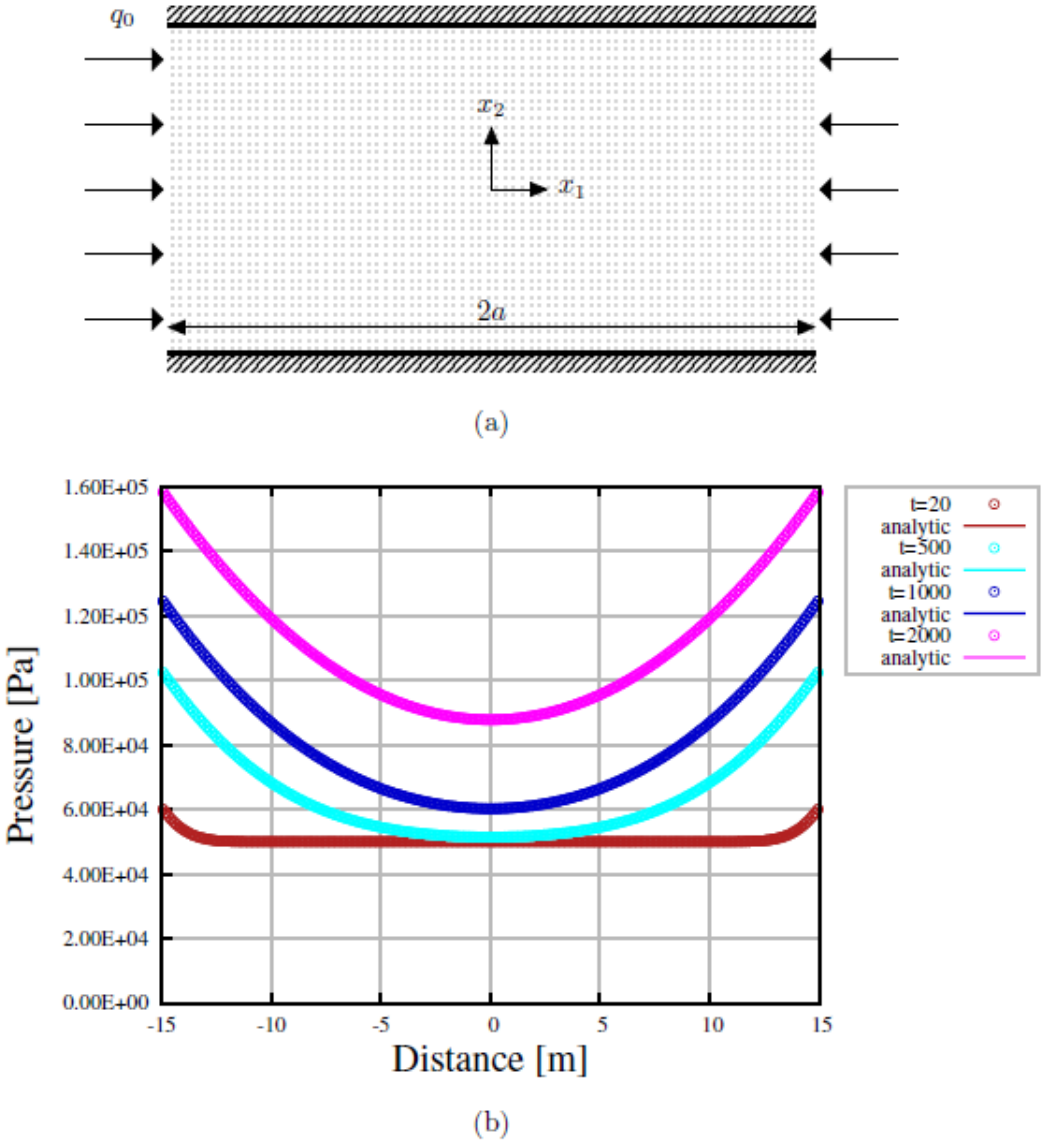

Figure 42: Finite slab fixed-rate test case with (a) loading, and (b) pressure results.

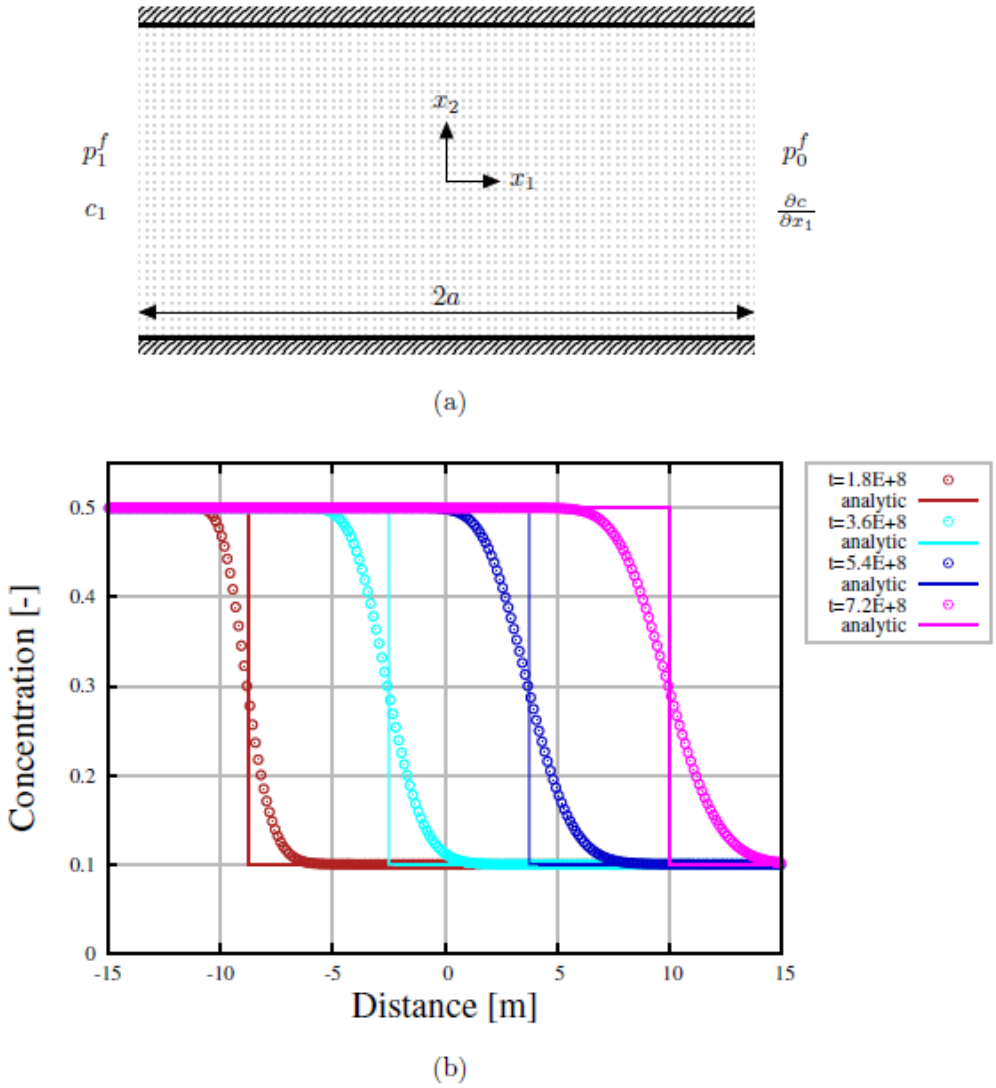

Figure 43: Finite slab advection test case with (a) loading, and (b) concentration results.

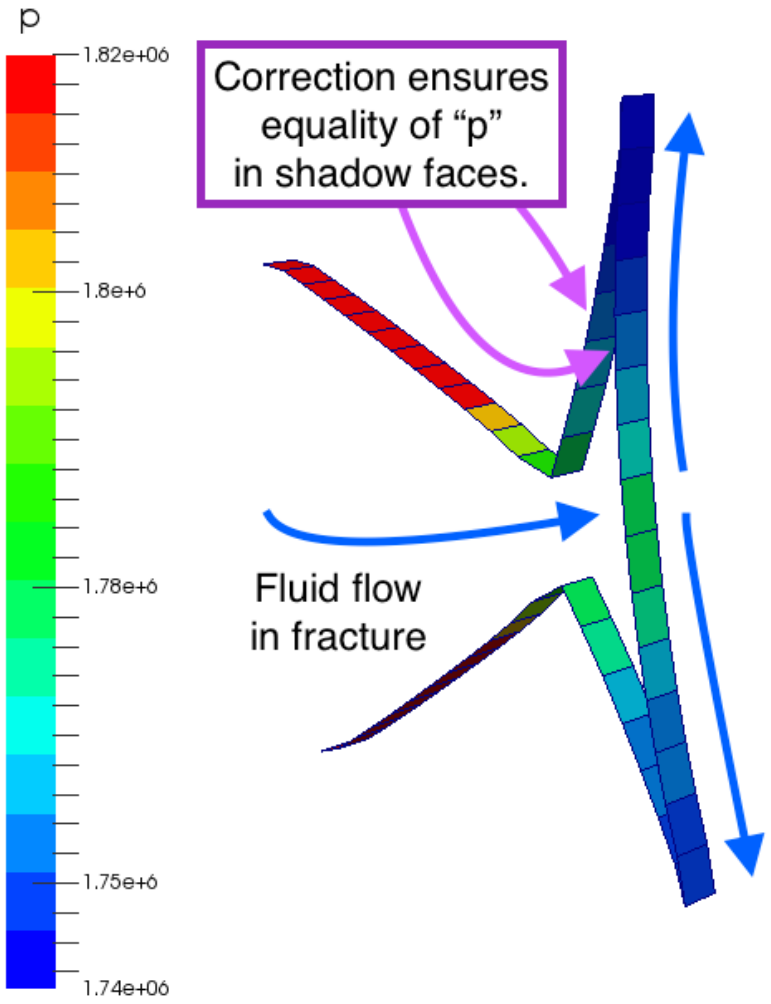

Figure 44: Application of corrective fluxes, to apply a gradient towards physical fracture tips.

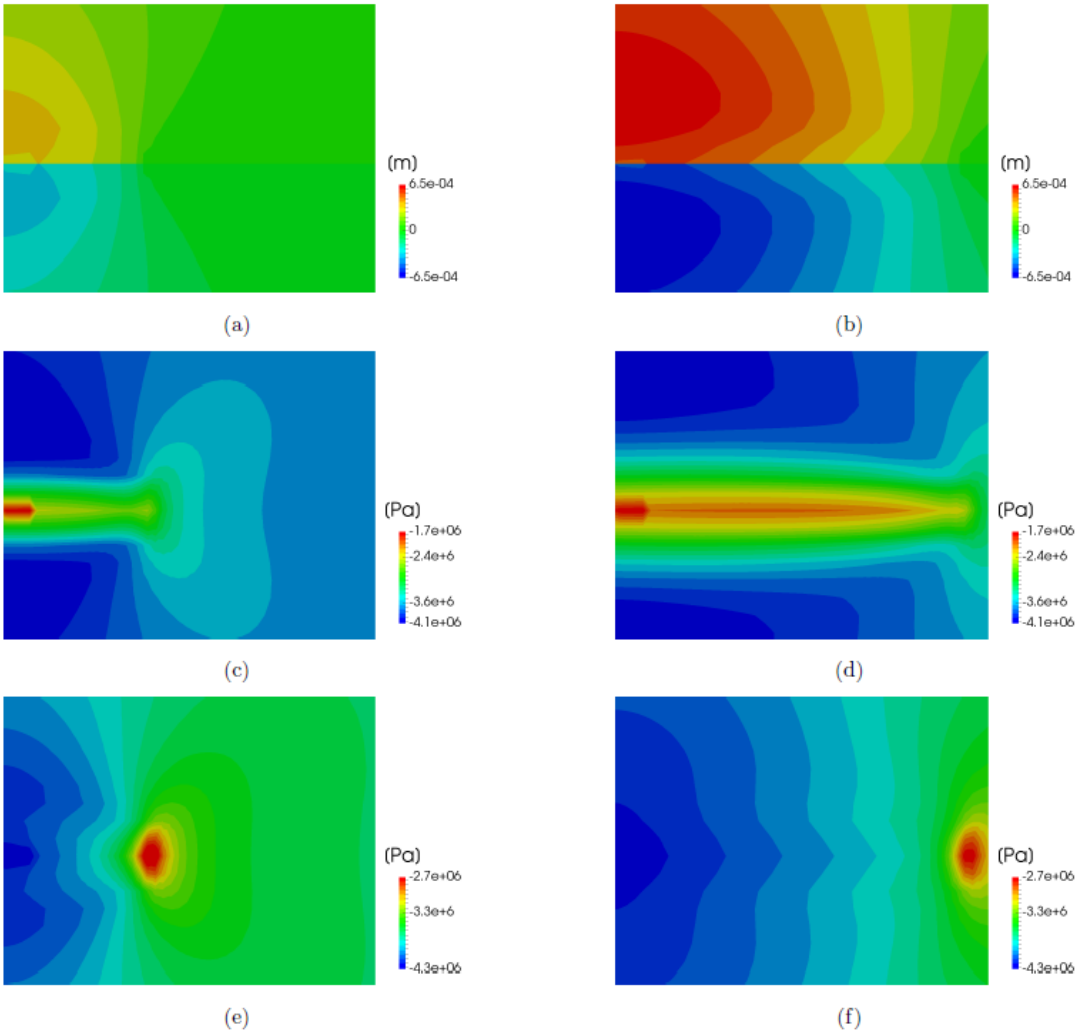

Figure 45: Meter-scale fracture case, showing at t = 3 s (left) and t = 12 s (right): (a) and (b) displacement; (c) and (d) effective stress; and, (e) and (f) stress.

NUMERICAL RESULTS

Verification cases are presented regarding fluid flow and proppant transport. Example cases show the fracture bifurcation result, as well as a meter-scale dynamically grown fracture. Material properties for fracture fluids are as listed in Table 9.

Slab fixed-value problem

Extraction of the boundary width, the conversion of width to a time-invariant fracture permeability, and solution of the surface differential equation are verified against the fixed-value finite slab problem [66]. This would be the discretized solution of Eq. (110). Material properties are as listed in Table 9. A slab of finite out-of-plane length with in-plane extent $2a$ of 30 m was initialized at a uniform fracture pressure p_0^f of 0.5 Pa. At zero-time along the far x_1-direction boundaries, the pressure is raised to pressure p_1^f of 1E+5 Pa. No displacement is allowed at the impermeable top and bottom confining plates. Loading conditions are presented in Fig. 41a. The numerical results overlay the analytic solution, Fig. 41b with curves labeled by time [s]. Error was greatest during early-time flow (t = 20 s curve), and error reduces with decreased time-step size.

Finite slab fixed-rate problem

Enforcement of fracturing pressure boundary gradients based upon a set inflow rate is verified against the fixed-rate finite slab problem [66]. The domain's out-of-plane height h is 1 m. Again, the domain was initialized at a uniform fracture pressure p_0^f of 0.5 Pa, and no transverse outflow is allowed. However the injection rate is fixed at Q_0 of 2.3E-9 m3/s. (A low injection rate is used to scale the presented t = 2000 s curve into the 0.1E+6 Pa range, with orders-of-magnitude higher inflow rates essayed successfully.) Loading conditions are presented in Fig. 42a. The numerical results overlay the analytic solution, Fig. 42b. Similarly error was greatest during early-time flow (t = 20 s curve),

and error reduces with decreased time-step size. Reductions with time step size (Δt) indicate error arising from the Euler, implicit differencing scheme employed. This scheme is used to approximate temporal derivative terms, and is first-order accurate.

Finite slab advection problem

A finite slab fixed-value problem is modeled as incompressible with coupled advection. At zero-time along the negative x_1-direction boundary, the pressure is set to pressure p_1^f of 1E+5 Pa. At the positive x_1-direction boundary, the pressure is p_0^f of 0.5E+5 Pa. For this problem, the flow velocity is a time- and spatially-invariant $\mathbf{q}$. Coefficients are set so that the empirical proppant $\mathbf{q}^{\mathrm{p}}$ reduces to the fracture $\mathbf{q}$: $\mathbf{A}^{\mathrm{p}}$ is the identity tensor and $\mathbf{b}^{\mathrm{p}}$ the zero vector. The boundary conditions for proppant concentration are c_1 of 0.5 [-] and zero-gradient, respectively (Fig. 43a). The initial conditions is c_0 of 0.1 [-]. The numerical results vary from the analytic solution as an artifact of numerical dispersion, Fig. 43b. Error was greatest during late-time flow (t = 7.2E+8 s curve), and the dispersion increases over simulation time.

Fracture bifurcation

The FA approach has been successfully utilized to solve fluid flow for a bifurcating fracture, Fig. 44. In a word, the proposed correction procedure results in an Picard-iteratively evolved field-wide source term, the ultimate values and distribution of which we remain always agnostic and ideally ignorant: in as much as this term applies no aggregate subtraction or addition of pressure-volumes to the system as a whole (such that fluid mass is conserved); nor, does the correction result in violations of the divergence operator discretized locally along either side of the fracture's surface. The method may be complimented by augmenting the implicit Laplacian with off-diagonal coefficients representing transverse discharge. Fig. 44 shows the consequent flow distribution during

end pressurization of the fracture tips, and is not geomechanically coupled. Also, we can readily speed the convergence of our coupled fracture fluid flow and correction system. The converged correction at the end of the prior "outer iteration" or coupling loop makes for a natural guess as to the correction field during the current iteration (for instance, immediately antecedent to topological changes consequent of enforced softening behavior). This observation holds true for models without sharp discontinuities in their fracture fluid injection time series.

Fracture bifurcation

Those test cases describing above analytical solutions were modified to include a geomechanical coupling with the bounding poroelastic solid. These cases represent hydromehanical couplings where the fracture geometry is fixed. These cases evidence a reduced level of stability with respect to homogeneous, single-phase flow coupled mechanical models, for the same time step. The explicit time marching of Eq. (120) provided for sufficient convergence in static fracture cases. However for modeling of propagating fractures on the meter-scale, iteration to the fixed-stress residual $R^{\phi*}$ was required with significant numerical relation of the computed mass-conserving width. Time steps used were in the order of microseconds.

Results are presented for a growing, planar, and bi-wing fracture with a KGD geometry. Half the geometry is modeled with central symmetry boundary conditions, such that the boundary condition at the central inlet is $Q_0/2$. The leak-off term is computed using an explicit Carter model, while other cases were run with implicit Carter and fixed-gradient models; all results presented exclude leak-off from the CZ tip for the fracture pressure solution (numerically) but include leak-off. To achieve numerical stability, it is important to end simulation prior to significant effects from the boundary in

the direction of fracture growth (here x_1). This accords with experience in matching the KGD solution for a purely elastic, inviscid fracture model. (Parenthetically, sensitivity to far-field location argues for development of implicit "infinite volume" boundary conditions along the poroelastic domain boundary. Being that, both FA and inviscid fracture growth evidence a similar instability with respect to boundary effects.)

For both models presented, initialization of the starter fracture length was at a pressure according to the far-field stress. A fixed-stress model is used inside the poroelastic solid as well as the fracture, however: no differentiation is made between real fracture vs. cohesive coefficients; the explicit fixed-stress formulation is used as a preconditioning step of both pore and fracturing pressures. The near-fracture mesh refinement is sufficient to capture a pressure profile away from the fracture, however are insufficient to capture a length-limiting CZ tip and energy depletion effects. Results in Fig. 45 show this effect, with respect to the recovered stress.

Parallelism considerations

The proposed method for fracture-transverse flow curtails concerns as pertains scalability for parallel, clustered modeling of fracture flow on the surface of spatially decomposed solid domains. In the event that so-called "zero-halo" domain-based decomposition is utilized – viz. a non-overlapping split of the volumetric mesh into subdomains solved on individual processors – the procedure co-locates the control areas which discretize fracture flow, alongside the surrounding volumetric mesh. The fundamentals of the zero-halo layer approach are by extension preserved. The current implementation has been successfully tested for fracture growth on multiple separate processors, and growth *across* inter-processor boundaries. However, the behavior when

fractures propagate *along* inter-processor boundaries does not exhibit independence of the domain decomposition, as present.

CONCLUSION

We have applied the FA method to the problem of fluid flow in fractures for the first time. A novel scheme has been proposed to enforce the continuity of pressure across the width of evolving fractures, whilst conserving mass, within complex fracture networks. Although we have described use of the FA method to solve along surfaces defined by FV-discretized solid boundaries, this procedure is clearly generally applicable to all solid domain discretization (e.g. FE) from which a discrete fracture surface can be derived by enforcement of softening/failure behaviors.

As the default behavior of a FA-based 2D surface discretization, the fracture fluid flow must inevitably proceed in halves and along the half-width of each half of the 3D softening domain. So, the focus of this work is to produce a FA-discretized solution of fracturing pressures written directly in terms of the boundary values of 3D linearized poroelastic unknowns. A numerical scheme is proposed. The scheme couples with the numerical solution of the FA-discretized fracture network. The scheme both ensures continuity of fluid pressure across the width of hydraulic fractures, and also enables solution of fracture fluid flow inside more complex networks. The scheme ensures that the converged solution is correct with respect to the mathematical model describing intra-fracture transverse fluid flow.

Chapter 4: Admissible stress analysis for loaded and decreasingly poroelastic cohesive zones

The CZ model is useful with respect to the modeling of hydraulic fractures used in oilfield completions. Unlike traditional linear elastic fracture mechanics (LEFM) tools, the CZ model offers the combined opportunity to intuitively discretize preexisting planes of weakness like oriented natural fractures, and to examine effects of rock layer heterogeneity, as well as plasticity. However, one feature of the model is commonly perceived as disadvantageous. Viz. the results of CZ-based modeling tend to vary based upon the absolute value of the imposed in situ stress state (as initialized at the beginning of a simulation, to capture far-field geological loading). Any variability based upon in situ stresses contradicts a large set of legacy modeling tools. The latter softwares discretize and solve fluid flow equations within the propagating fracture, then supply the net pressure – pumped fluid pressures minus resolved normal far-field stresses – in order to determine local fracture widths and extension.

This work examines the result of such assumptions as applied to CZ-based modeling, as relates to poroelastic domains. Previous efforts have shown the ability of CZ model-type numerics to model hydraulic fractures within poroelastic solids [61], however do not consider the full range of admissible stress analysis. Where the model implementation has been discussed as a continuity condition, the traction-separation law has been indicated as determining the Terzaghi's effective stress state across the CZ [31]; the validity of that assumption is discussed, using Rice's approach to the J-integral taken about the vanishing volume surrounding CZ boundary.

BACKGROUND

The CZ model distributes a mainly tensile load upon a proscribed surface at the fracture tip [67]. As the fracture extends, the CZ travels with the tip as surface energy depletes: a certain traction-separation law is utilized in order to discount cohesive tractions, or to remove cohesive tractions from surfaces where the fracture energy is fully depleted. Rice introduced and first analyzed cohesive zone tractions using the Mode I J-integral [68]. The scalar J-integral is a counterclockwise line integral which was shown to be path independent for linear elasticity by Rice, when taken around an unloaded straight crack:

$$J_1 = \int_{\Gamma} [U \mathrm{d}x_2 - \mathbf{t_S} \cdot \frac{\partial \mathbf{u}}{\partial x_1} \mathrm{d}\Gamma], \quad (146)$$

where U is the strain energy density, $\mathbf{t_S}$ the traction, $\mathbf{u}$ the displacement, and Γ the surface contour. To compute J_1, the contour must include the crack tip.

The above integral has several important properties. The Mode I J_1 can be shown to equal to the fracture energy G_{Ic}, for small CZ lengths relative to the overall fracture length immediately as the crack start to grow [68]. J-integral analysis is extensible to thermally loaded materials, and hence poroelastic materials. In this regard, the coupled thermo/poroelastic CZ boundary tractions are to be linearly superimposed during numerical analysis [70]. A similar idea is used here with respect to poroelastic stresses on both sides of the CZ/solid boundary, as well as to account for the residual stress state implied by adoption of the "net pressure" approach.

Unfortunately, the geomechanics literature is relatively scant as to in situ (residual) stress effects on fracture growth. The starting-off point for our investigation is prior discussion of confining-stress-related toughness variability [71]. Sato and Hashida

describe similar conclusions. Specifically, toughnesses are shown to increase with degree of far-field compressive stress; a CZ model is applied where the applied cohesive tractions are held constant, such that numerically recovered toughness increases as a linear function of the confining stresses. In contrast, we consider the toughness to be invariant (a downhole matching parameter), so as to recover the opening-mode analytic solution regardless of the in situ stress state. Following from that goal, it is requisite to introduce the incremental J-integral at the fracture tip. Therefore alternate decompositions of the resolved tractions are considered as the traction-separation initiation condition, our overarching aims being to maintain the effect of far-field stress anisotropy (on fracture growth) and to maintain the effect of shale stress barriers.

Fictitious tip J-integral

A domain is at a residual stress state $\mathbf{S}^0$ (where superscripting 0 marks a value in the reference configuration). The domain is loaded statically at far-field as well as crack boundaries by $\mathbf{t}_{\mathbf{S}^0} = \mathbf{n} \cdot \mathbf{S}^0$, for $\mathbf{n}$ the surface normal. We define an incremental form of the J-integral that remains invariant with respect to the residual stress state, under the loading described – i.e. as to reproduce the LEFM result. First define the strain energy density U as a partition of functionals:

$$U_{\mathbf{S}^0} = \int_0^{\boldsymbol{\varepsilon}} \mathbf{S}^0 : \mathrm{d}\boldsymbol{\varepsilon}, \qquad U = \int_0^{\boldsymbol{\varepsilon}} (\mathbf{S} - \mathbf{S}^0) : \mathrm{d}\boldsymbol{\varepsilon} + U_{\mathbf{S}^0}, \quad (147)$$

where strain $\boldsymbol{\varepsilon}$ is with respect to a reference configuration (displacement $\mathbf{u} = \mathbf{0}$ at $\mathbf{S}^0$). We then introduce an incremental J-integral independent of the far-field stress, under the described loading conditions. This would be:

$$J_1^* = \int_{\Gamma} [U_{\mathbf{S}-\mathbf{S}^0} \mathrm{d}x_2 - \mathbf{t}_{\mathbf{S}-\mathbf{S}^0} \cdot \frac{\partial \mathbf{u}}{\partial x_1} \mathrm{d}\Gamma], \quad (148)$$

where $U_{\mathbf{S}-\mathbf{S}^0}$ is the change in strain energy density associated with traction perturbation $\mathbf{t}_{\mathbf{S}-\mathbf{S}^0}$. Intuitively if the line integral is taken to include only the bounding solid directly adjacent to the CZ, the strain energy term vanishes – as there exists no x_2 increment (Fig. 46). When considering loaded or curved cracks, shrinking contour Γ to enclose the infinitesimal volume around the CZ tip recovers "path dependence" (a comprehensive reference is [69]). The summed traction integrand taken directly adjacent to the CZ is often referred to as J_{tip} in literature; subsequently, the utility of Rice's observation has been extended e.g. to the determination of traction-separation laws based upon J-integral analysis [72, 73]. Clearly the tip integral reduces as per Fig. 46, for no $\mathrm{d}x_2$ of integration, and latterly for any set of applied tractions $\mathbf{t}_{\mathbf{S}-\mathbf{S}^0} = \mathbf{t}_{\mathbf{S}} - \mathbf{n} \cdot \mathbf{S}^0$ above the resolved residual stresses:

$$J_{tip}^* = -\int_{\Gamma} \left[\mathbf{t}_{\mathbf{S}-\mathbf{S}^0} \cdot \frac{\partial \mathbf{u}}{\partial x_1} \right] \mathrm{d}\Gamma. \quad (149)$$

The additional effect of poroelastic boundary tractions are now superimposed. The consequence is to resolve the far-field effective stresses when describing tractions the CZ tip region. Combining these concepts, the integrand considered here is only the surface traction component:

$$J_{tip}^* = -\int_{\Gamma} [\mathbf{t}_{\boldsymbol{\sigma}-\boldsymbol{\sigma}^0} \cdot \frac{\partial \mathbf{u}}{\partial x_1}] \mathrm{d}\Gamma, \quad (150)$$

where $\boldsymbol{\sigma}$ is the Biot's effective stress, and thus $\mathbf{t}_{\boldsymbol{\sigma}-\boldsymbol{\sigma}^0}$ a decomposition of $\mathbf{t}_{\mathbf{S}}$ which relates applied boundary stresses directly to the displacement gradient. Displacement $\mathbf{u}$ is considered with respect to a reference configuration at the residual state of stress $\mathbf{S}^0$ and pressure p^0. So $\boldsymbol{\sigma}^0 = \mathbf{S}^0 + bp^0\mathbf{I}$, where b is the Biot's coefficient. We use the notation and poroelastic formulation of Hooke's law in incremental form [19].

Finally the following is noted. The point in stating Eq. (150) is not to recover additional poroelastic or stress-dependent physics. Instead we remove by parsing-out tip additional physics as deviations, in order to numerically recover the fracture energy associated with simulation of an unstressed elastic domain. The use of fictitious tip integral J^*_{tip} as an explanatory measure is considered important. This is in order to compare work integrated via the traction-separation law established per CZ strategy, vs. work actually performed by prescribed boundary tractions. The comparison is further expanded in the below section on error analysis.

COHESIVE CONTINUITY CONDITIONS

First, whereas effective stresses within the poroelastic domain are resolved to determine CZ initiation tractions, that consideration constitutes a continuity condition. Second, whereas cohesive traction-separation laws dictate the exact amount of effective stress applied across the softening discontinuity, this is also a continuity condition (as an absolute statement of the decreasingly tensile total stress state, i.e. during traction-separation, see [31]). Should the CZ model be idealized as a "spring": the former condition ensures continuity of the resolved total stress during initiation. The latter condition dictates exactly the total stress for any state of fracture energy depletion (per integrated surface traction-displacements).

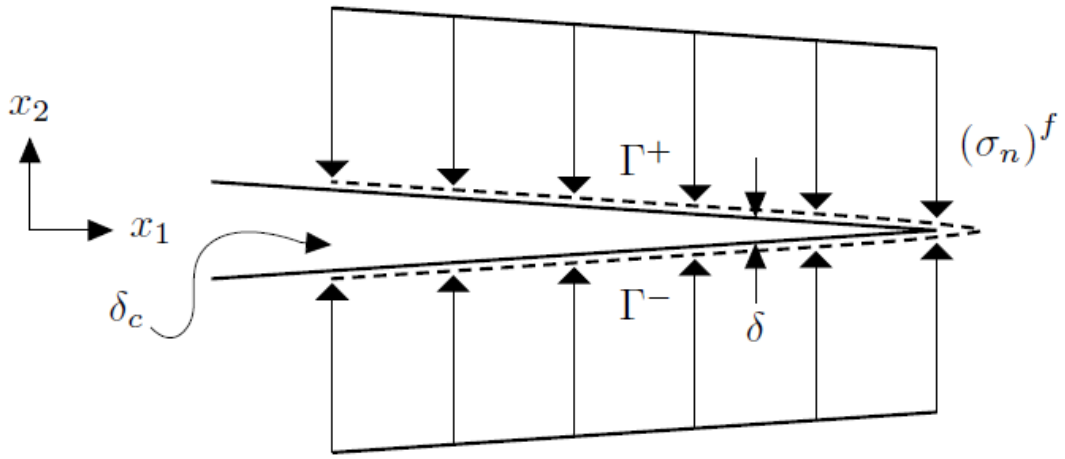

Figure 46: Integral contour (after [68, 69]).

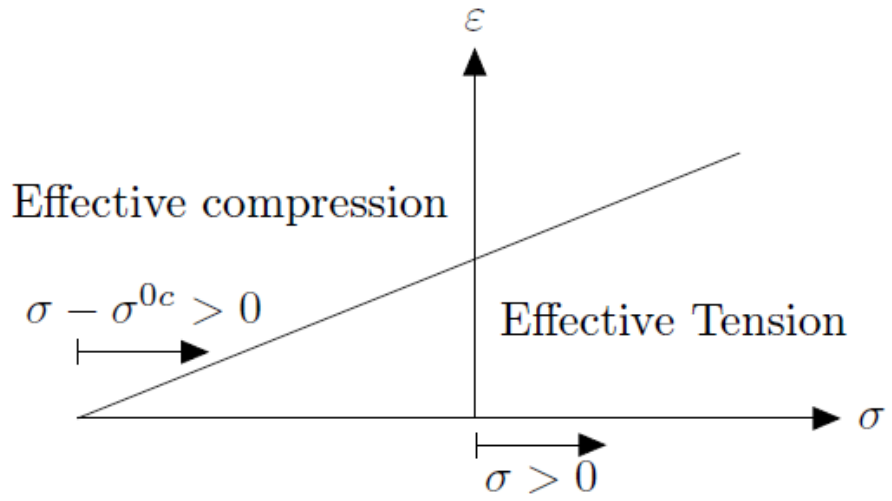

Figure 40: Reference configuration with linear strain-stress curve representing Hooke's law.

In this section, the continuity condition at initiation is expressed in simple terms. In the next section, these definitions of the cohesive tractions ($\mathbf{t}^f$) are substituted into the tip integral (J^*_{tip}). Hence in the way of warning, the equations presented in this section consecutively re-derive the approximately same result. The result is the effect of cohesive continuity conditions is dictated by a resolved effective stress decomposition. These statements appear as mere repetition – until the presentation of Eq. (167) as combines with Eq. (172) – which constitutes the nub of this work.

Initiation tractions

Let us suppose that the cohesive traction-separation processes initiates based upon achieving some critical effective stress state, within a poroelastic solid domain. Let this critical stress state be dictated by any combination of the components of the vector,

$$(\mathbf{t}^f)^{0c} = \mathbf{t_S} + b^f p\mathbf{n}, \quad (151)$$

which is an effective stress as resolved on a surface oriented by surface normal n; superscript f dually indicates cohesive tractions $\mathbf{t}^f$, and values inside the fracture; p is pressure and when not superscripted by f indicates a pore pressure, otherwise the fracturing pressure. Let the effective traction used for softening evaluation be some combination of the resolved total stress and the pore pressure acting on the surface, such that coefficient b^f has an arbitrary value. Further, superscript $0c$ is used to demarcate the value of a field instantaneously when the softening processes initiate. The total stress at this time is then a known value:

$$(\mathbf{t_S})^{0c} = (\mathbf{t}^f)^{0c} - b^f(p^f)^{0c}\mathbf{n}, \quad (152)$$

where the fracturing pressure acting inside the cohesive zone p^f is the pore pressure on that surface. This assumption maintains the continuity of pressure assumption for a cohesive zone evolving within a poroelastic medium. The initiation total stress may then be re-expressed as the function of the Biot's coefficient b acting within the adjacent poroelastic material, such that:

$$(\mathbf{t_S})^{0c} = (\mathbf{t}^f)^{0c} - b_b(p^f)^{0c}\mathbf{n}_b - (b^f - b_b)(p^f)^{0c}\mathbf{n}_b, \quad (153)$$

where subscript b indicates a "boundary" value of the poroelastic solid.

For generality, let us define a unit vector $\mathbf{f}$ by which to decompose the resolved effective tractions, and understood in relation to the surface normal $\mathbf{n}$. For example if resolving stresses relating to a purely Mode I-type CZ initiation criteria, then let $\mathbf{f} = \mathbf{n}$. In this instance softening processes would begin at the threshold resolved stress defined as:

$$\frac{\mathbf{f}\cdot\mathbf{t}^f}{(\sigma_f)_c} = \frac{\mathbf{n}\cdot\mathbf{t}^f}{(\sigma_n)_c} \geq 1 \quad \text{softening initiation,} \qquad \frac{\mathbf{f}\cdot\mathbf{t}^f}{(\sigma_f)_c} = \frac{\mathbf{n}\cdot\mathbf{t}^f}{(\sigma_n)_c} < 1 \quad \text{no softening,} \qquad (154)$$

where $(\sigma_n)_c$ represents the Mode I CZ model critical effective normal stress. In a similar manner, the critical effective stress for an arbitrarily oriented unit vector $\mathbf{f}$ can be defined as $(\sigma_f)_c$. That said however, it is straightforward that use of a $\mathbf{f}$-resolved cohesive traction-separation law (pure Mode I, e.g.) risks initiation of the cohesive traction-separation in dynamic disequilibrium. In the example, this would be where: (a) shear components of traction are resolved in the debonding region, prior to CZ process initiation; then (b) no shear traction component is re-supplied by the Mode I law (because otherwise requiring numeric traction-separation integration).

Softening tractions

Let us consider the definition of the mainly tensile cohesive tractions applied along the CZ inside a homogeneous and poroelastic material. For this analysis, we make a continuity assumption about pore pressure on the bounding solid p_b with respect to fracture pressure p^f. Further, we equate the cohesive tractions by definition. The tensile tractions applied as per the particular cohesive model will be $(\mathbf{t}^f)_b$. The effect that the applied cohesive tractions induces on the opposite side of the CZ boundary (i.e. within the softening solid) will be $\mathbf{t}^f$. Therefore, at anytime:

$$p^f = p_b, \qquad (\mathbf{t}^f)_b = \mathbf{t}^f, \quad (155)$$

where the above second equation holds only within the CZ (where applied cohesive tractions are non-zero). Additionally as aid to our analysis, let us define in a poroelastic solid three different decompositions of the resolved stress. These are:

$$\mathbf{t}_{\boldsymbol{\sigma}-\boldsymbol{\sigma}^0} = \mathbf{n}\cdot(\boldsymbol{\sigma}-\boldsymbol{\sigma}^0), \quad (156)$$

$$\mathbf{t}_{\boldsymbol{\sigma}} = \mathbf{t}_{\boldsymbol{\sigma}-\boldsymbol{\sigma}^0} + \mathbf{n}\cdot\boldsymbol{\sigma}^0, (\boldsymbol{\sigma}-\boldsymbol{\sigma}^0) \quad (157)$$

$$\mathbf{t}_{\mathbf{S}} = \mathbf{n}\cdot\mathbf{S} = \mathbf{t}_{\boldsymbol{\sigma}} - bp\mathbf{n} = \mathbf{t}_{\boldsymbol{\sigma}-\boldsymbol{\sigma}^0} + \mathbf{n}\cdot\boldsymbol{\sigma}^0 - bp\mathbf{n}, (\boldsymbol{\sigma}-\boldsymbol{\sigma}^0) \quad (158)$$

where $\boldsymbol{\sigma}^0$ is the residual effective stress tensor, e.g. as defined for an initial state of zero relative strain ($\mathbf{u}=\mathbf{0}$). Further once subtracting poroelastic and residual effects, the resolved stresses $\mathbf{t}_{\boldsymbol{\sigma}-\boldsymbol{\sigma}^0}$ are only a function of: displacement gradient; material (Lamé's) parameters; and, orientation of the resolving plane as dictated by its normal $\mathbf{n}$.

Biot's effective stress

Initially, let us suppose that the cohesive traction-separation law relates only the effective stresses acting alongside the boundary of the solid to the opening displacement. Thus we assume that within the CZ at any moment the applied cohesive traction is $\mathbf{t}^f$ – a

function of the Biot's effective stress. Therefore the resolved stress $\mathbf{t_S}$ acting along the CZ boundary is defined:

$$\mathbf{t}^f = \mathbf{t_\sigma}, \qquad \mathbf{t_S} = \mathbf{t}^f - b_b p_b \mathbf{n}_b. \quad (159)$$

This is true at any time, including instantaneously when the softening processes begins. Therefore and by substitution of Eq. (153),

$$\begin{aligned} (\mathbf{t_S})^{0c} &= (\mathbf{t}^f)^{0c} - b_b p_b^{0c} \mathbf{n}_b, \\ &= (\mathbf{t}^f)_b^{0c} - b_b (p^f)^{0c} \mathbf{n}_b - (b^f - b_b)(p^f)^{0c} \mathbf{n}_b. \quad (160) \end{aligned}$$

As above by continuity, and with equality of cohesive tractions by definition:

$$\begin{aligned} (\mathbf{t_S})^{0c} &= (\mathbf{t}^f)^{0c} - b_b p_b^{0c} \mathbf{n}_b, \\ &= (\mathbf{t}^f)_b^{0c} - b_b (p^f)^{0c} \mathbf{n}_b - (b^f - b_b)(p^f)^{0c} \mathbf{n}_b. \quad (161) \end{aligned}$$

After canceling, the result of substitution is that $b^f = b_b$.

For completeness, consider a simpler model which evaluates stresses as act on a plane with a specific orientation to the normal (resolved by $\mathbf{f} \cdot \mathbf{t}^f$, for $\mathbf{f}$ also a unit vector). As at the moment of softening initiation point it is known that the stress is $(\sigma_f)_c$. Hence for a known stress state:

$$\begin{aligned} (\sigma_f)_c &= \mathbf{f} \cdot [(\mathbf{t_S})^{0c} + b_b p_b^{0c} \mathbf{n}] \leftrightarrow \\ \mathbf{f} \cdot [(\mathbf{t}^f)^{0c} - b_b p_b^{0c} \mathbf{n}_b] &= \mathbf{f} \cdot [(\mathbf{t}^f)^{0c} - b_b (p^f)^{0c} \mathbf{n}_b - (b^f - b_b)(p^f)^{0c} \mathbf{n}_b]. \quad (162) \end{aligned}$$

Using pressure continuity and assuming $\mathbf{f} \cdot \mathbf{n} \neq 0$, again the result is:

$$b^f = b_b. \quad (163)$$

The consequence of this analysis is quite limiting. In essence, the definition of the effective stress state for softening evaluation is dictated by the choice of Biot's

coefficient within the poroelastic solid. (We note that b_b need not be the small-strain, thus invariant coefficient. Only simultaneous variation of the effecting coefficient b_b on either side of the CZ boundary is required.) However, shear terms where $\mathbf{f} \cdot \mathbf{n} = 0$ are unaffected by the choice of b^f. The last result is logical given that poroelastic like thermoelastic boundary tractions act in the boundary-normal direction.

Effective stress

Now let us suppose we desire to design a system such that by choice $b^f \neq b_b$. Unfortunately, Eq. (151) cannot be changed. Instead let us define an additional resolved effective stress $\mathbf{t}_{\boldsymbol{\sigma}^f}$,

$$\mathbf{t}_{\boldsymbol{\sigma}^f} = \mathbf{n} \cdot \mathbf{S} + b^f p \mathbf{n} = \mathbf{t}_{\boldsymbol{\sigma}-\boldsymbol{\sigma}^0} + \mathbf{n} \cdot \boldsymbol{\sigma}^0 + (b^f - b) p \mathbf{n}. \quad (164)$$

It is worth noting that the definition of $\mathbf{t}_{\boldsymbol{\sigma}^f}$ holds at any boundary within a cohesive zone, because of the presumption of pressure continuity $p^f = p_b$. Changing the assumption of Eq. (159), we re-write the cohesive definition and the total stress at the boundary:

$$\mathbf{t}^f = \mathbf{t}_{\boldsymbol{\sigma}^f}, \qquad \mathbf{t}_{\mathbf{S}} = \mathbf{t}^f - b_b^f p_b \mathbf{n}_b. \quad (165)$$

Once again this is true at any time, including instantaneously when the softening processes begins. Therefore and by substitution of Eq. (152),

$$\begin{aligned} (\mathbf{t}_{\mathbf{S}})^{0c} &= (\mathbf{t}^f)^{0c} - b_b^f p_b^{0c} \mathbf{n}_b, \\ &= (\mathbf{t}^f)_b^{0c} - b^f (p^f)^{0c} \mathbf{n}_b, \quad (166) \end{aligned}$$

where the result is $b^f = b_b^f$. As a consequential effect, the definition of the effective stress state for softening evaluation can be decided by any choice of b^f. However, an

open question is: whether assumption $\mathbf{t}^f = \mathbf{t}_{\boldsymbol{\sigma}^f}$ reproduces a computational fracture mechanics that exhibits convergence numerically to a LEFM-comparable solution.

Generalized net pressure approach

Finally, let us suppose the result Eq. (163). However, we will instead consider a system where initiation tractions anticipate the application of the residual stress state everywhere in the solid, and particular within the CZ. The system is then:

$$(\mathbf{t}^f)^{0c} = \mathbf{t}_{\mathbf{S}} + b^f p\mathbf{n} - \mathbf{n}\cdot\boldsymbol{\sigma}^{0c}, \qquad \mathbf{t}^f = \mathbf{t}_{\boldsymbol{\sigma}-\boldsymbol{\sigma}^{0c}}, \quad (167)$$

where $\boldsymbol{\sigma}^{0c}$ is a arbitrary tensor representing the net pressure discount. Using the net pressure approach, a dilatational $\boldsymbol{\sigma}^{0c}$ may be selected so that $\boldsymbol{\sigma}^0 - \boldsymbol{\sigma}^{0c}$ resolves shear components of traction, and hence direct CZ initiation towards the in situ minimum (tension positive)/maximum principal (compression positive) stress direction. The same analysis as in above section can be used to show continuity, as above. The option $\boldsymbol{\sigma}^{0c} = \boldsymbol{\sigma}^0$ also maintains dynamic compatibility during initiation, with the effect of encouraging CZ development in shearing zones; in that event shear CZ initiation will occur without any prohibitory effect of the far-field stress.

TIP J-INTEGRAL

The J-integral can be used to evolve the relationship between loading applied (numerically) within the CZ, and the fracture toughness of the material. However, we only consider that component of traction applied in computation of J^*_{tip} that contributes to a change in gradient of displacement (strain and hence stress). The contour hence encompasses poroelastic tractions applied along the interior of the boundary. For purposes of exposition, let us define the cohesive tractions to be acting in Mode I, such that there exists only a normal cohesive stress,

$$(\sigma_n)^f = \mathbf{n} \cdot \mathbf{t}^f, \qquad \sigma^0 = \mathbf{n} \cdot (\mathbf{n} \cdot \boldsymbol{\sigma}^0), \quad (168)$$

which stress $(\sigma_n)^f$ is a (step) function of separation distance δ. For this analysis, the J-integral will be taken with respect to all tractions along the CZ boundary, as per Eq. (150).

Biot's effective stress

Initially, let us suppose the result of Eq. (163). Now, let us integrate all tractions applied at the boundary of the CZ. Then we have

$$J_{tip}^* = -\int_{\Gamma} [(\sigma_n)^f - \sigma^0 + b_b p_b - b^f p^f] \frac{\mathrm{d}}{\mathrm{d}x_1} [\Gamma^+ - \Gamma^-] \, \mathrm{d}x_1. \quad (169)$$

Since Eq. (163) holds, and by continuity the pressures equate. Further $\delta(x_1) = \Gamma^+(x_1) - \Gamma^-(x_1)$, so then the above reduces to:

$$\begin{aligned} J_{tip}^* &= -\int_{\Gamma} [(\sigma_n)^f - \sigma^0] \frac{\mathrm{d}}{\mathrm{d}x_1} [\Gamma^+ - \Gamma^-] \mathrm{d}x_1 \,, \\ &= \int_0^{\delta_c} [(\sigma_n)^f - \sigma^0] \mathrm{d}\delta \,, \end{aligned} \quad (170)$$

where J_{tip}^* depends on $(\sigma_n)^f$, a function of separation distance δ; Jtip also depends on σ^0 which may vary with x_1. The selection of $\mathbf{t}^f = \mathbf{t}_{\boldsymbol{\sigma}}$ produces an integrated J_{tip}^* that relates to the material's fracture energy (G_{Ic}), without dependence on the pressure of the fracturing fluid.

Effective stress

Now suppose b^f is arbitrarily chosen, yet continuity of fracture and boundary pressure holds. J^*_{tip} does not reduce as before, but instead,

$$\begin{aligned} J^*_{tip} &= -\int_{\Gamma} [(\sigma_n)^f - \sigma^0 + (b_b - b^f)p^f] \frac{\mathrm{d}}{\mathrm{d}x_1} [\Gamma^+ - \Gamma^-] \mathrm{d}x_1 \,, \\ &= \int_0^{\delta_c} [(\sigma_n)^f - \sigma^0 + (b_b - b^f)p^f] \mathrm{d}\delta. \end{aligned} \tag{171}$$

The crack faces are in fact OVERLOADED by stress perturbations from term $(b_b - b^f)p^f$. Resultantly, J^*_{tip} is dependent on varying fracturing pressure p^f. It is shown therefore that selecting cohesive tractions $\mathbf{t}^f = \mathbf{t}_{\boldsymbol{\sigma}^f}$ for arbitrary b^f engenders overloading at the CZ tip – at least, with respect to the desired LEFM analogue (and with static b_b). Notably however, the stress state maintains dynamic admissibility during initiation.

Generalized net pressure approach

When writing the J-integral still Eq. (163) holds; and by continuity $p^f = p_b$. We will assume that $\boldsymbol{\sigma}^{0c}$ has been initialized to the local maximum principal (tension positive) residual stress, so $\sigma^{0c} = \sigma^0$. For Mode I opening we have,

$$\begin{aligned} J^*_{tip} &= -\int_{\Gamma} [(\sigma_n)^f - \sigma^0 + b_b p_b + \sigma^{0c} - b^f p^f] \frac{\mathrm{d}}{\mathrm{d}x_1} [\Gamma^+ - \Gamma^-] \mathrm{d}x_1 \,, \\ &= \int_0^{\delta_c} [(\sigma_n)^f] \mathrm{d}\delta \,, \end{aligned} \tag{172}$$

where J^*_{tip} depends only on $(\sigma_n)^f$, a function of separation distance δ. Being $\sigma^{0c} = \sigma^0$, the residual stress terms cancel as applied equally and oppositely – as if the contour

integrates entirely within the bounds of the softening solid. Hence, the CZ-boundary deformation produced is insensitive to both: (a) fracturing fluid pressure inside the CZ; and, (b) the initial stress state. As and if $\sigma^{0c}(x_1)$ varies with $\sigma^{0c}(x_1)$, the result is general along the entirety of the CZ; the contribution of residual stresses is therefore removed regardless of encountering stress barriers such as shale layers. In effect, Eq. (172) is a statement that the net pressure approach most mimetically re-capitulates the results of LEFM-based fracture modeling – mimicking an unstressed domain.

However, the effect of stress barriers may be re-incorporated into the net pressure approach by choice of a spatially invariant $\boldsymbol{\sigma}^{0c}$, e.g. as the spherical tensor with diagonal entries the maximum principal effective stress within the domain. That choice would be most consistent with the basic theme of this analysis: to remove the effect of residual stresses by linear superpositioning – with respect to both fracture loading and applied cohesive tractions. Finally, dynamic compatibility is still maintained during softening, under the net pressure approach.

MATHEMATICAL MODEL

The deforming poroelastic solid is solved using the "over-relaxed" approach for linear elasticity [15] as extended to poroelasticity [20], with softening behavior evaluated as in [16] and extended to multi-material elasticity with softening in [11, 30]. The approach to enforcing boundary gradients of displacement is the same as in [18].

Fracture continuity

Flow into and out of a unit volume can be considered as an integral of fluid volume change in response to change in pressure, change in the volume, and volumetric fluxes in and out. The isothermal K bulk modulus (inverse compressibility) defines:

$$\frac{1}{K} = \frac{1}{\rho}\frac{\mathrm{d}\rho}{\mathrm{d}p}|_T = -\frac{1}{V}\frac{\mathrm{d}V}{\mathrm{d}p}|_T, \quad (173)$$

where ρ is the density, p the pressure, and V the volume. With the assumption of small changes in fluid density, the isothermal strong integral form of the conservation equation is:

$$\int_V [\frac{1}{K^f}\frac{\partial p^f}{\partial t} + \frac{1}{V}\frac{\partial V}{\partial t}]\mathrm{d}V = -\oint_S \mathbf{n}\cdot\mathbf{q}\mathrm{d}S + Q, \quad (174)$$

where t is time, S the surface, $\mathbf{n}$ the surface normal vector, $\mathbf{q}$ the flux, and Q the volumetric rate of production. Frequently, for cubic law flow e.g., the Reynolds constitutive relation is substituted to adduce gradient from flux. However the constitutive relation for conductivity is not consequential of traction continuity across the fracture, and the fluid is modeled as inviscid.

Tip continuity

The constitutive relation for flux into, within, or from the CZ is not demanded by continuity of traction. It is feasible that a zero-gradient boundary condition could be imposed on fluid flux entering the CZ from the fracture, or from the CZ with respect to boundary internal pressures. I.e. this analysis provides no insight on the appropriate relation for flux in the tip, $\mathbf{q}$. From that perspective, any method for computing CZ boundary pore pressures is admissible.

Net pressure coupling

In order to maintain continuity of pore fluid flow and displacement, the fracturing pressures are applied as:

$$p_b^n = (p^f)^n, \quad (175)$$

$$(\mathbf{t_S})_b^n = (\mathbf{t}^f)^n - p_b^n[H_s^n + b^f(1 - H_s^n)]\mathbf{n}_b + \mathbf{n}_b \cdot \boldsymbol{\sigma}^{0c}(1 - H_s^n), \quad (176)$$

where H_s is a unit step function of fracture surface (s) that is 1 in the fracture and 0 in the CZ. Cancellation of the resolved stress state ($\mathbf{n} \cdot \boldsymbol{\sigma}^{0c}$) can often be assumed, as operating against residual stresses within the CZ ($-\mathbf{n} \cdot \boldsymbol{\sigma}^{0}$).

Leak-off

Consider the leak-off sink Q_{leak} term as applied to boundary S_b. Specifically leak-off is a function of the gradient between the center of the fracture-boundary volume V_{bP}, and its boundary surface S_b. The normal flux across S_b is then $q_{bn} = \mathbf{n} \cdot \mathbf{q}_b$. By Darcy's law, the normal flux of fluid entering the porous boundary is a function of the gradient of pressure along the fracture boundary,

$$q_{bn} = -(\mathbf{n} \cdot \frac{k_p}{\mu_p} \nabla p)_b, \quad (177)$$

where subscripting p refers to pore fluid values.

NUMERICAL RESULTS

The limit case of a poroelastic case for which $b_b = 0$ is presented (however continuity of pressures is maintained, such that $p_b = p^f$). The formation intrinsic permeability is set such that $k_p \approx 0$, in order to induce no leak-off. Following the generalized net pressure approach, then inside the cohesive zone $b^f = b_b = 0$. Hence, hydraulic pressures are applied inside the CZ as $-b^f p^f \mathbf{n}_b = \mathbf{0}$. Indeed, the recovered fracture energy is recovered EXACTLY as per Eq. (172). Because the incremental J-integral effectively eliminates in situ stress effects, two LEFM-mimetic results are recovered. On the one hand, the fracturing pressures increase by the same increment as

the decrease in far-field minimum stress (TENSION POSITIVE, Fig. 48). On the other, the fracture lengths for a given inflow rate are identical (Fig. 49) – invariant of the in situ stress state.

In both Fig. 48 and Fig. 49, comparison is made to the analytic solution for a KGD-geometry, inviscid fracturing fluid [38]. Following Mokryakov's notation, L is the total fracture length, and includes the CZ. In contrast, length R is the length of the fully depleted fracture – and hence R excludes the CZ. The analytic L curve is based upon LEFM, and compares favorably to the numerically recovered L. However, care should be taken when comparing the analytic against numerical R curves as: (a) the analytic R curve's closed form expression neglects terms; and (b) the analytic curve is based on a Barenblatt CZ model. That being noted, the Barenblatt curve provides a lower bound for the numerical R.

ERROR ANALYSIS

The net pressure CZ strategy proposed implies significant limitations and contradiction. To be specific, the approach's re-application e.g. of the resolved spherical residual stress tensor along the debonding CZ represents unaccounted-for work. That is to say: the applied residual tractions enter into no traction-separation law by which a surface energy is summed. Thus these applied stresses are ignored as contributing to the total energy of the system. Given the tremendous in situ stress magnitude anticipated in everyday oilfield practice, this term is likely to exceed the recovered surface energy. To estimate, simply reduce Eq. (172) to elasticity for $b_b = b^f = 0$. For Mode I Dugdale-type models, then we have:

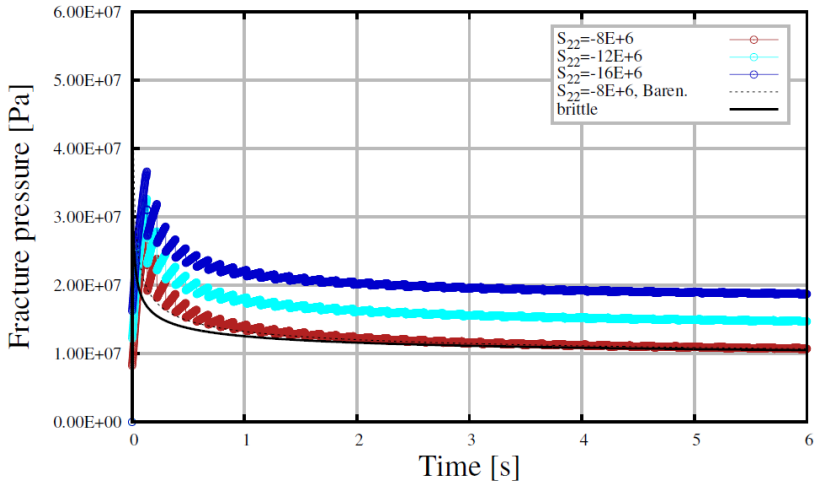

Figure 48: KGD geometry case, recovered fracturing pressures vary with far-field stress.

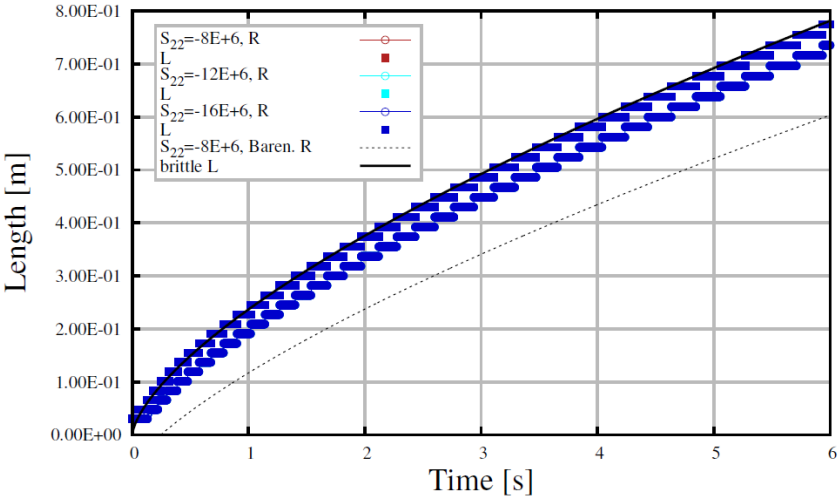

Figure 49: KGD geometry case, recovered length invariant with far-field stress (same initial net pressure).

$$J^*_{tip} = \int_0^{\delta_c} [(S_n)^f] \mathrm{d}\delta = (S_n)^f \delta_c \,, \qquad E_{J^*_{tip}} = -\int_0^{\delta_c} [S^{0c}] \mathrm{d}\delta = -S^{0c}\delta_c, \quad (1)$$

for $(S_n)^f$ the applied normal tractions, S^{0c} the resolved discounting tensor, and E the energy error term per unit area. The error thus increases linearly with far-field stresses, were rock properties are assumed to be fixed. For example for far-field stresses of -1E+7 Pa and cohesive traction of 1E+6 Pa, the ratio of error over fracture energy is $E_{J^*_{tip}}/J^*_{tip} = 10$ [-].

Nevertheless at minimum, the net pressure framework: (a) admits by clear statement its source of associated error; and, (b) provides for quantification of the error. The error is inherent in any numerical fracture mechanics which is possessed of the following characteristic. Specifically, that the boundary displacements in the near-tip zone are used to calculate a fracture energy or toughness, i.e. in order to assess propagation. Thus ratios of errors over fracture energy are in compliance with legacy softwares. On the other hand, the fracture energy may be physically understood as a downhole matching parameter not relatable to the rock's unconfined toughness; such a presumption would disagree with e.g. [71]. However in this case, the recovery of the specified fracture energy is exact under the net pressure approach.

CONCLUSION

This coupling strategy will retain the responsiveness of the cohesive implementation to the fracture energy. In short, our claims are: by removal of the resolved residual stresses and re-addition during cohesive softening, the generalized net pressure approach most mimetically recapitulates LEFM analysis; the Biot's effective stress is the most acceptable tensor for softening evaluation in a poroelastic material,

given a small-strain constitutive relation; no conclusion as to flux constitutive relation or as to a uniquely correct fluid modulus in the CZ (either Biot's modulus or fracture fluid compressibility) is allowable from the limited investigation.

It is further noted that this CZ strategy captures the idea of Camacho and Ortiz-type formulations [34], in that sensibly no boundary deformation is permissible at the initiation of the softening regime. In this regard, kinematic compatibility with the opening mode is maintained by dint of using the same numerical width; dynamic compatibility by the instantaneous identity of the stress state. Finally, the most interesting (and unexplored) component of the analysis pertains to the Biot's coefficient for failure evaluation. The suggestion is that the Biot's coefficient used for failure evaluation may indeed vary from the in situ coefficient in the bounding solid. But in this scenario, some additional constitutive relation is required to determine the failure coefficient – jointly coordinated with its simultaneous application within the CZ (to the fracturing pressures).

Appendix

Initialization steps

Special initialization conditions are contemplated regarding loading at the interface of reservoir layers. Firstly in the way of a warning, a discontinuity in normal component of resolved initial EFFECTIVE stress tensor along the interface will be produced inevitably by numerous, realistic multi-material initialization scenarios. For instance, with a variable Biot's coefficient, such a discontinuity will be produced by use of an initialized continuous total stress tensor and initialized uniform pore pressure field. In these cases, additional analysis to enforce the continuity of interface tractions must be applied. However, if the Biot's coefficient is homogeneous within the domain, we expect the normal component of the residual effective stress tensor to be continuous over multi-material interfaces. (For a simulation initialized at equilibrium we expect the tangential component of residual stress/effective stresses tensor resolved over the interface, to be continuous.)

In the case of a homogeneous Biot's coefficient, the assertion of continuity of resolved total stress in Eqs. (24) by (26) reduces to the assertion of the continuity of resolved effective tractions over each bimaterial interface. In these instances, the simplified (and quasi-static) numerics do apply. Nevertheless: the initial VERTICAL (total) stresses are to be specified as a CONSTANT VALUE; variable horizontal total stresses may be initialized arbitrarily in different layers, given that the multi-material interface layers are modeled to coincide with the horizontal axis. Specification of an initial stress tensor enables use of fixed-displacement boundary conditions along far-field reservoir boundaries. Geological multi-material interfaces may often be considered to be horizontal and to coincide with locally flat bedding planes. Further vertical stress is supposed to be a continuous principal stress with depth. Hence no shear tractions are to

develop along these interfaces prior to the stress-state's initialization, as they would be acting in a plane described by a principal stress direction. In particular, for each interface unit normal vector $\mathbf{n}_i$:

$$(\mathbf{I} - \mathbf{n}_i\mathbf{n}_i) \cdot (\mathbf{n}_i \cdot \boldsymbol{\sigma}^0) = \mathbf{0}. \quad (179)$$

The assumption is that geological multi-material interfaces are layered to correspond to the horizontal plane. This assumption may make initialization of the stress state (i.e. the residual effective stress state $\boldsymbol{\sigma}^0$) more straightforward.

Mandel's problem

For an applied load S_0, fluid pressures and stresses are then:

$$p(x_1, t=0) = p_0 = \frac{1}{3}B(1+\nu_u)S_0 \quad (180)$$

$$p(x_1, t) = 2p_0 \sum_{m=1}^{\infty} \{[(\cos(\frac{\alpha_m x_1}{a}) - \cos\alpha_m)], \quad (181)$$
$$\times (\frac{\sin\alpha_m}{\alpha_m - \sin\alpha_m\cos\alpha_m})\exp(-\frac{\alpha_m^2 ct}{a^2})\},$$

$$S_{22}(x_1, t) = S_0A_0 + S_0(\frac{\nu_u - \nu}{1-\nu_u})$$
$$\times \sum_{m=1}^{\infty} A_m[(\frac{1-\nu}{\nu_u - \nu})\cos\alpha_m - \cos(\frac{\alpha_m x_1}{a})]\exp(-\frac{\alpha_m^2 ct}{a^2}). \quad (182)$$

The equation coefficients are:

$$\frac{\tan\alpha_m}{\alpha_m} = \frac{1-\nu}{\nu_u - \nu}, \quad (183)$$

$$A_m = 2(\frac{1-\nu_u}{1-\nu})(\frac{\sin\alpha_m}{\alpha_m - \sin\alpha_m\cos\alpha_m}), \quad (184)$$

and $A_m = -1$.

Eshelby's inclusion

The plane-strain method of Eshelby's inclusion for an elliptical inhomogeneity within a poroelastic domain produces a closed form solution for stresses within the inclusion, and a semi-analytic expression for stresses within the matrix. The solution is predicated on the concept of computed eigenstrains within the inclusion. The eigenstrain is the fictitious strain experienced by the inclusion if unbounded by the surrounding matrix. For a uniform poroelastic loading or dilational residual stress state, these strains are easy to compute using Hooke's Law and uniform throughout the inhomogeneity. Further details are omitted here for brevity, however are covered in micromechanics literature [74].

With regard to the plane-strain solution at hand, as indicated previously the solution is sensitive to aspect ratio of the ellipse e, ratio of inclusion over matrix shear modulus R_μ, and Poisson's ratio in the inclusion ν^* versus in the matrix ν. Inclusion properties are superscripted by $*$. For the system, the normalized eigenstrains are:

$$(\boldsymbol{\varepsilon}_N^{**})_{11} = \frac{A}{C}, \qquad (\boldsymbol{\varepsilon}_N^{**})_{22} = \frac{B}{C}, \quad (185)$$

where:

$$A = [R_\mu[(1+e)^2(1-\nu) - e^2] + e^2](1-2\nu^*)(1-\nu), \quad (186)$$

$$B = [R_\mu[(1+e)^2(1-\nu) - 1] + 1](1-2\nu^*)(1-\nu), \quad (187)$$

$$C = R_\mu[2(1+e^2)(1-\nu)(1-\nu^*) - 2e\nu^*(1-2\nu) + R_\mu e(3-4\nu^*)] + e(1-2\nu^*). \quad (188)$$

The normalized stress arching ratios are defined as:

$$\boldsymbol{\gamma}_{\alpha}^{*} = \frac{\Delta\mathbf{S} + \Delta\sigma^{0}\mathbf{I}}{\Delta\sigma^{0} - b\Delta p}, \qquad \boldsymbol{\gamma}_{\alpha} = \frac{\Delta\mathbf{S} - b\Delta p\mathbf{I}}{\Delta\sigma^{0} - b\Delta p}, \quad (189)$$

where Δp is a change in pore pressures and $\Delta\sigma^{0}$ a change in the residual stress tensor. Therefore Δp is a pressure change with respect to in-situ pressure such that $\Delta p = p^{*}$; and, it is assumed that pore pressures within the matrix remain at the initial pressure p. Here the residual effective stress state within the inclusion is diagonal tensor $\sigma^{0*}\mathbf{I}$ for scalar $\sigma^{0*} = S^{0*} + bp^{0*}$, where is assumed that residual stress state in the matrix remains unperturbed and valued at $\sigma^{0}\mathbf{I}$. So, the change in imposed residual stresses is $\Delta\sigma^{0} = \sigma^{0*} - \sigma^{0}$.

Within the inclusion, the components of normalized stress arching ratio $\$↤↲$ are simply,

$$(\boldsymbol{\gamma}_{\alpha}^{*})_{11} = \frac{D}{C}, \qquad (\boldsymbol{\gamma}_{\alpha}^{*})_{22} = \frac{E}{C}, \quad (190)$$

where:

$$D = (1 - 2\nu^{*})[R_{\mu}[e(1 - 2\nu) + 2(1 - \nu)] + e], \quad (191)$$
$$E = (1 - 2\nu^{*})[R_{\mu}[2\mathrm{e}(1 - \nu) + 1 - 2\nu] + 1]e. \quad (192)$$

Within the matrix, the components of normalized stress arching ratio $\boldsymbol{\gamma}_{\alpha}$ are:

$$(\boldsymbol{\gamma}_{\alpha})_{11} = N_{1111}(\boldsymbol{\varepsilon}_{N}^{**})_{11} + N_{1122}(\boldsymbol{\varepsilon}_{N}^{**})_{22}, \quad (193)$$
$$(\boldsymbol{\gamma}_{\alpha})_{22} = N_{2211}(\boldsymbol{\varepsilon}_{N}^{**})_{11} + N_{2222}(\boldsymbol{\varepsilon}_{N}^{**})_{22}, \quad (194)$$

where:

$$N_{1111} = \int_{-1}^{1}\int_{-e\sqrt{1-(x_1')^2}}^{e\sqrt{1-(x_1')^2}} [8\frac{(x_1-x_1')^4}{R^6} - 4\frac{(x_1-x_1')^2}{R^4} - \frac{1}{R^2}]\mathrm{d}x_2'\mathrm{d}x_1', \quad (195)$$

$$N_{2222} = \int_{-1}^{1}\int_{-e\sqrt{1-(x_1')^2}}^{e\sqrt{1-(x_1')^2}} [8\frac{(x_2-x_2')^4}{R^6} - 4\frac{(x_2-x_2')^2}{R^4} - \frac{1}{R^2}]\mathrm{d}x_2'\mathrm{d}x_1', \quad (196)$$

$$N_{1122} = \int_{-1}^{1}\int_{-e\sqrt{1-(x_1')^2}}^{e\sqrt{1-(x_1')^2}} [8\frac{(x_1-x_1')^2(x_2-x_2')^2}{R^6} - \frac{1}{R^2}]\mathrm{d}x_2'\,\mathrm{d}x_1', \quad (197)$$

$$N_{2211} = N_{1122}. \quad (198)$$

and denominator R is a function of evaluated coordinate (x_1, x_2) and dummy coordinate (x_1', x_2'),

$$R = \sqrt{(x_1-x_1')^2 + (x_2-x_2')^2}. \quad (199)$$

The associated change in effective stress state can be recovered by substation into Eq. (189) of the tension-positive total stress definition Eq. (58). The change in effective stress in the inclusion ($\Delta\boldsymbol{\sigma}^*$) and in the matrix ($\Delta\boldsymbol{\sigma}$) are,

$$\Delta\boldsymbol{\sigma}^* = [\Delta\sigma^0 - b\Delta p]\boldsymbol{\gamma}_\alpha^* - [\Delta\sigma^0 - b\Delta p]\mathbf{I}, \quad (200)$$

$$\Delta\boldsymbol{\sigma} = [\Delta\sigma^0 - b\Delta p]\boldsymbol{\gamma}_\alpha, \quad (201)$$

for $\Delta\boldsymbol{\sigma} = \Delta\mathbf{S} + b\Delta p\mathbf{I}$.

Finite slab fixed-value problem

Coefficient α^f is useful in the solution of compressible finite slab problems,

$$k^f = w^2, \qquad \alpha^f = \frac{K^f}{(k^f/12\mu_f)}. \quad (2002)$$

For an applied fixed-value boundary pressure p_1^f and initial pressure $p^f(x_1, t = 0) = p_0^f$, fluid pressures are then:

$$p^f(x_1, t) = p_1^f + 4(p_0^f - p_1^f) \times \sum_{m=0}^{\infty} [(\frac{\sin\lambda_m}{2\lambda_m - \sin 2\lambda_m})\cos(\frac{\lambda_m x_1}{a})\exp(-\frac{\lambda_m^2 \alpha^f t}{a^2})]. \quad (203)$$

The equation eigenvalues are:

$$\lambda_m = \pi(m + \frac{1}{2}). \quad (204)$$

Finite slab fixed-rate problem

For an applied volumetric inflow rate Q_0, the boundary-normal velocity is:

$$q_0 = \frac{Q_0}{wh}. \quad (205)$$

For initial pressure $p^f(x_1, t = 0) = p_0^f$, the time-varying fluid pressures are then:

$$p^f(x_1, t) = p_0^f + \frac{q_0 a}{k^f}(\frac{\alpha^f t}{a^2}) + \sum_{m=1}^{\infty} [A_m \cos(\frac{\lambda_m (x_1 - a)}{a})]. \quad (206)$$

The equation coefficients are:

$$A_m = \frac{2}{\lambda_m^2}[1 - \exp(-\frac{\lambda_m^2 \alpha^f t}{a^2})], \qquad \lambda_m = \pi m. \quad (207)$$

Finite slab advection problem

The negative-x_1 and positive-x_1 boundaries have fixed value conditions p_0^f and p_1^f, respectively. For incompressible flow in a finite slab, with fixed pressure conditions at the boundaries, the fluid velocity is constant across the domain. The concentration transport problem reduces to a first-order hyperbolic partial differential equation, with constant coefficient q_0^{p}:

$$0 = \frac{\partial c}{\partial t} + q_0^{\mathrm{p}} \frac{\partial c}{\partial x_1}, \qquad q_0^{\mathrm{p}} = \frac{k^f (p_1^f - p_0^f)}{24 \mu_f a}. \quad (208)$$

The negative-x_1 and positive-x_1 boundaries have fixed value conditions p_0^f and p_1^f, respectively. For incompressible flow in a finite slab, with fixed pressure conditions at the boundaries, the fluid velocity is constant across the domain. The concentration transport problem reduces to a first-order hyperbolic partial differential equation, with constant coefficient q_0^{p}:

For initial pressure $c(x_1, t = 0) = c_0$ and boundary condition $c(x_1 = -a, t) = c_1$, the concentration unknown is advected through the domain until $\partial c(x_1 = a, t)/\partial x_1 = 0$. The position of the traveling front is $q_0^{\mathrm{p}} t - a$, and solution:

$$c(x_1, t) = (c_0 - c_1) H(x_1 - q_0^{\mathrm{p}} t + a) + c_1, \quad (209)$$

for H the Heaviside step function.

Area-transverse fluxes

The requirement for use of the transverse-flux scheme results from a simple cause. Thus far FA methods have never previously been applied to discretize fluid flow along branched or branching surfaces. Resultantly any vanilla FA implementation used in order to solve the flow equations, would fail for network topologies containing fractures

that intersect, bifurcate or evidence asymmetric patterns of leak-off. Consequently the "vanilla" FA surface discretization would restrict modeling to non-intersecting, non-branching surfaces – and moreover, without asymmetric variation of fracture leak-off: in a word, the Laplacian term of Eq. (117) acts only along each side of the fracture. To address this issue, we moot a correction that allows for fluid flow across complex fracture networks, by providing for flow between control and so-called "shadow" control surfaces using an strongly iteratively coupled explicit correction term. In line with the penalty method, any discrepancy in the pressure evolved at control and shadow control surfaces is minimized during convergence of the fracture fluid flow. In this system, the fundamental quantum of the correction is the competition with other Darcy-type fluxes resolved on the control surfaces' regularly FA-discretized edges: hence, the penalty volumetric fluxes are scaled by that quantum – and for no other reason than to ensure that penalty fluxes accumulate in increments of baseline the same order as the implicitly discretized fluxes occurring between adjacent control surfaces. Hence for any current time step n, an appropriately normalized volumetric rate correction term hence links current and shadow face with the penalty represented as:

$$Q_{cor} = \alpha_{cor} \sum_{i_n} [w_P^{n*} \frac{(k^f)_P^\theta}{12\mu^f} (\frac{(p^f)_{sP}^{i_{pf}} - (p^f)_P^{i_{pf}}}{\bar{L}_{PN}})] \bar{L}_e \,, \quad (210)$$

for 1 to i_n the series of converged iterations for fracture fluid flow solution, α_{cor} a penalty factor of order less than unity, and $\bar{L}_{PN}$ and $\bar{L}_e$ approximations of terms used in the discretization of gradient and divergence operators, respectively. Their ratio was approximated here as:

$$\frac{\bar{L}_e}{\bar{L}_{PN}} \approx \frac{[\frac{1}{2}(S_P + S_{sP})]^{\frac{1}{2}}}{[\frac{1}{2}(S_P + S_{sP})]^{\frac{1}{2}}} = 1. \quad (211)$$

Substitution considerably cleans the correction:

$$Q_{cor} = \alpha_{cor} \sum_{i_{pf}} [w_P^{n*} \frac{(k^f)_P^{\theta}}{12\mu^f} ((p^f)_{sP}^{i_{pf}} - (p^f)_P^{i_{pf}})]. \quad (212)$$

The convergence of the fracture fluid flow equation implies convergence of the penalty term, and so being the penalty difference $(p^f)_{sP}^{i_{pf}} - (p^f)_P^{i_{pf}}$ reduces to $(p^f)_{sP}^n - (p^f)_P^n = 0$. Hence, clearly as the pressure equation converges, our correction accepts a zero discrepancy between converged values of face and shadow face. Thus the continuity of fracture pressure across the width of the fracture is imposed. The generalized argument for the specific form of the correction used in Eq. (212) is that, for an elliptic problem, the correction should emerge over convergence relative to the flux associated with the implicit spatial discretization. Such that, for the general equation, the implicit discretization and penalty term would be evolved as:

$$0 = \sum_e (\mathbf{m} \cdot \nabla_s \Phi^f)_e^n L_e + \alpha_{cor} \sum_{i_{\Phi f}} [((\Phi^f)_{sP}^{i_{\Phi f}} - (\Phi^f)_P^{i_{\Phi f}})], \quad (213)$$

where Φ^f is a potential normalized by the coefficient of the Laplacian, and w has been canceled. This coupling (whilst implemented as a source term) essentially permits direct volumetric fluxes between disparate control surfaces, which are otherwise not immediately attached along a manifold. Therefore, this term is defined and discretized as contributing to flow. Lastly the correction Q_{cor} implies no net fluid loss from the system.

Conservation is imposed by the symmetry of the scheme. Each fracture face is the shadow face of its twin face, and as such fluid lost by any of twin faces is only gained by its shadow:

$$(Q_{cor})_P = -(Q_{cor})_{sP}. \quad (214)$$

Thus, in as much as the FA method provides for flow in the longitudinal direction of the fractures, a correction allows for fluid to pass transversely between each side of the fractures' surface.

Glossary

$b =$ Biot's coefficient, -, -

$c =$ concentration (of proppant), -, -

$C_{leak} =$ Carter leak-off coefficient, L/$t^{1/2}$, m/s$^{1/2}$

$C^{\mathrm{p}} =$ volmetric concentration source, L^3/t, m^3/s

$G =$ surface energy release rate, m/t^2, J/m^2

$k =$ permeability, L^2, m^2

$K =$ bulk modulus, m/(L - t^2), Pa

$\mathbf{K} =$ permeability tensor, L^2, m^2

$M =$ Biot's modulus, m/(L - t^2), Pa

$\mathbf{n} =$ normal vector, -, -

$p =$ pore pressure, m/(L - t^2), Pa

$\mathbf{q} =$ flux, L/t, m/s

$Q =$ volmetric source, L^3/t, m^3/s

$R =$ residual, -, -

$\mathbf{S} =$ total stress tensor, m/(L - t^2), Pa

$t =$ time, t, s

$\mathbf{t} =$ traction vector, m/(L - t^2), Pa

$\mathbf{u} =$ displacement vector, L, m

$\boldsymbol{\varepsilon} =$ strain tensor, -, -

$\lambda =$ Lamé's first parameter, m/(L - t^2), Pa

$\mu =$ shear modulus, m/(L - t^2), Pa

$\mu_p =$ pore fluid viscosity, m/(L - t), Pa-s

$\rho =$ density, m/L^3, kg/m^3

$\delta =$ separation distance, L, m

$\boldsymbol{\sigma} =$ effective stress tensor, m/(L - t^2), Pa

$\phi =$ porosity, -, -

Superscripts

Subscripts

$a =$ material a

$b =$ material b, or boundary

$c =$ cohesive, or critical

$d =$ drained/dry

$i =$ interface

$n =$ normal

$N =$ nieghbor cell

$p =$ pore fluid

$P =$ current cell

$t =$ tangential

$u =$ undrained

$v =$ volumetric

$I =$ Mode I

$II =$ Mode II

References

[1] H. Gu and E. Siebrits. Effect of Formation Modulus Contrast on Hydraulic Fracture Height Containment. *SPE Production & Operations*, 23(02):170–176, 2008.

[2] X. Weng. Incorporation of 2D Fluid Flow into a Pseudo-3D Hydraulic Fracturing Simulator. *SPE Production Engineering*, 7(04):331–337, 1992.

[3] Y. Yao, S.V. Gosavi, K.H. Searles, and T.K. Ellison. Cohesive Fracture Mechanics Based Analysis to Model Ductile Rock Fracture. In *44th US Rock Mechanics Symposium, Salt Lake City*, Utah, 2010.

[4] D.H. Shin and M.M. Sharma. Factors Controlling the Simultaneous Propagation of Multiple Competing Fractures in a Horizontal Well. In *SPE Hydraulic Fracturing Technology Conference*, The Woodlands, Texas, 2014.

[5] H. Wang, M. Marongiu-Porcu, and M.J. Economides. Poroelastic versus Poroplastic Modeling of Hydraulic Fracturing. In *SPE Hydraulic Fracturing Technology Conference*, The Woodlands, Texas, 2014.

[6] P.W. Harper and S.R. Hallett. Cohesive zone length in numerical simulations of composite delamination. *Engineering Fracture Mechanics*, 75(16):4774–4792, 2008.

[7] S. E. Leon, D. W. Spring, and G. H. Paulino. Reduction in mesh bias for dynamic fracture using adaptive splitting of polygonal finite elements. *International Journal for Numerical Methods in Engineering*, 100(8):555–576, 2014.

[8] J.E. Bishop, M.J. Martinez, and P. Newell. A Finite-Element Method for Modeling Fluid-Pressure Induced Discrete- Fracture Propagation using Random Meshes. In *46th US Rock Mechanics / Geomechanics Symposium*, Chicago, Illinois, 2012.

[9] P. Fu, S.M. Johnson, and C.R. Carrigan. An explicitly coupled hydro-geomechanical model for simulating hydraulic fracturing in arbitrary discrete fracture networks. *International Journal for Numerical and Analytical Methods in Geomechanics*, 37(14):2278–2300, 2013.

[10] L. Jing. A review of techniques, advances and outstanding issues in numerical modelling for rock mechanics and rock engineering. *International Journal of Rock Mechanics and Mining Sciences*, 40(3):283–353, 2003.

[11] Ž. Tuković, A. Ivanković, and A. Karač. Finite-volume stress analysis in multi-material linear elastic body. *International Journal for Numerical Methods in Engineering*, 93(4):400–419, 2013.

[12] J.M. Nordbotten. Finite volume hydromechanical simulation in porous media. *Water Resources Research*, 50(5):4379–4394, 2014.

[13] A. Dahi-Taleghani and J.E. Olson. Numerical Modeling of Multistranded-Hydraulic-Fracture Propagation: Accounting for the Interaction Between Induced and Natural Fractures. *SPE Journal*, 16(03):575–581, 2011.

[14] H.G. Weller and G. Tabor. A tensorial approach to computational continuum mechanics using object-oriented techniques. *Computers in Physics*, 12(1998):620–631, 1998.

[15] H. Jasak and H.G. Weller. Application of the finite volume method and unstructured meshes to linear elasticity. *International Journal for Numerical Methods in Engineering*, 48(2):267–287, 2000.

[16] Ž. Tuković. Arbitrary crack propagation model in OpenFOAM. Technical report, *Internal Report University of Zagreb in association with University College Dublin*, Zagreb, 2010.

[17] P. Cardiff, A. Karač, and A. Ivanković. Development of a finite volume contact solver based on the penalty method. *Computational Materials Science*, 64:283–284, 2012.

[18] P. Cardiff, A. Karač, and A. Ivanković. A large strain finite volume method for orthotropic bodies with general material orientations. *Computer Methods in Applied Mechanics and Engineering*, 268:318–335, 2014.

[19] O. Coussy. *Poromechanics*. John Wiley & Sons, 2004.

[20] T. Tang, O. Hededal, and P. Cardiff. On finite volume method implementation of poro-elasto-plasticity soil model. *International Journal for Numerical and Analytical Methods in Geomechanics*, 39(13):1410–1430, 2015.

[21] M. Mainguy and P. Longuemare. Coupling Fluid Flow and Rock Mechanics: Formulations of the Partial Coupling Between Reservoir and Geomechanical Simulators. *Oil & Gas Science and Technology*, 57(4):355–367, 2002.

[22] J. Kim. *Sequential Methods for Coupled Geomechanics and Multiphase Flow*. PhD thesis, Stanford University, Stanford, California, 2010.

[23] A. Mikelić and M.F. Wheeler. Convergence of iterative coupling for coupled flow and geomechanics. *Computational Geosciences*, 17(3):455–461, 2013.

[24] J. Hwang, E.C. Bryant, and M.M. Sharma. Stress Reorientation in Waterflooded Reservoirs. In *SPE Reservoir Simulation Symposium*, Houston, Texas, 2015.

[25] J.C. Jaeger, N.G. W Cook, and R. Zimmerman. *Fundamentals of Rock Mechanics*. John Wiley & Sons, 2009.

[26] H. Wang. *Theory of linear poroelasticity with applications to geomechanics and hydrogeology*. Princeton University Press, 2000.

[27] H. Deresiewicz and R. Skalak. On uniqueness in dynamic poroelasticity. *Bulletin of the Seismological Society of America*, 53(4):783–788, 1963.

[28] Ž. Tuković, P. Cardiff, H. Jasak, and A. Ivankovic. OpenFOAM Library for Fluid Structure Interaction. In *9th OpenFOAM Workshop*, Zagreb, Croatia, 2014.

[29] Ž. Tuković, A. Karač, P. Cardiff, and H. Jasak. Parallel unstructured finite-volume method for fluid-structure interaction. *Computer Methods in Applied Mechanics and Engineering*, (to appear), 2016.

[30] D. Carolan, Ž. Tuković, N. Murphy, and A. Ivanković. Arbitrary crack propagation in multi-phase materials using the finite volume method. *Computational Materials Science*, 69:153–159, 2013.

[31] B. Carrier and S. Granet. Numerical modeling of hydraulic fracture problem in permeable medium using cohesive zone model. *Engineering Fracture Mechanics*, 79:312–328, 2012.

[32] L. Ji, A. Settari, and R.B. Sullivan. A Novel Hydraulic Fracturing Model Fully Coupled with Geomechanics and Reservoir Simulator. *SPE Journal*, 14(3):423–430, 2009.

[33] E. Gordeliy and A. Peirce. Coupling schemes for modeling hydraulic fracture propagation using the XFEM. *Computer Methods in Applied Mechanics and Engineering*, 253:305–322, 2013.

[34] G.T. Camacho and M. Ortiz. Computational modelling of impact damage in brittle materials. *International Journal of Solids and Structures*, 33(20-22):2899–2938, aug 1996.

[35] C. Geuzaine and J.F. Remacle. Gmsh: A 3-D finite element mesh generator with built-in pre- and post-processing facilities. *International Journal for Numerical Methods in Engineering*, 79(11):1309–1331, 2009.

[36] A. Turon, C.G. Dávila, P.P. Camanho, and J. Costa. An engineering solution for mesh size effects in the simulation of delamination using cohesive zone models. *Engineering Fracture Mechanics*, 74(10):1665–1682, 2007.

[37] F. Zhang, N. Nagel, and F. Sheibani. Evaluation of Hydraulic Fractures Crossing Natural Fractures at High Angles Using a Hybrid Discrete-Continuum Model. In *48th US Rock Mechanics / Geomechanics Symposium*, Minneapolis, Minnesota, 2014.

[38] V. Mokryakov. Analytical solution for propagation of hydraulic fracture with Barenblatt's cohesive tip zone. International Journal of Fracture, 169(2):159–168, 2011.

[39] R. Manchanda. *A General Poro-Elastic Model for Pad-Scale Fracturing of Horizontal Wells*. PhD thesis, The University of Texas at Austin, Austin, Texas, 2015.

[40] H. Ouchi. *Development of a Peridynamics-based Hydraulic Fracturing Model for Fracture Growth in Heterogeneous Reservoirs*. PhD thesis, University of Texas at Austin, Austin, Texas, 2016.

[41] J. Kim, H.A. Tchelepi, and R. Juanes. Stability and convergence of sequential methods for coupled flow and geomechanics: Fixed-stress and fixed-strain splits. *Computer Methods in Applied Mechanics and Engineering*, 200(13-16):1591–1606, 2011.

[42] H. Soltanzadeh, Christopher D Hawkes, and Jitendra S Sharma. Poroelastic Model for Production- and Injection-Induced Stresses in Reservoirs with Elastic Properties Different from the Surrounding Rock. *International Journal of Geomechanics*, 7(5):353–361, 2007.

[43] H. Soltanzadeh and C.D. Hawkes. Semi-analytical models for stress change and fault reactivation induced by reservoir production and injection. *Journal of Petroleum Science and Engineering*, 60(2):71–85, 2008.

[44] H. Jasak. *Error Analysis and Estimation for the Finite Volume Method with Applications to Fluid Flows*. PhD thesis, Imperial College, London, England, 1996.

[45] V. Girault, K. Kumar, and M.F. Wheeler. Convergence of iterative coupling of geomechanics with flow in a fractured poroelastic medium. In I*CES REPORT 15-05*, February, 2015.

[46] A. Mikelić, B. Wang, and M.F. Wheeler. Numerical convergence study of iterative coupling for coupled flow and geomechanics. *Computational Geosciences*, 18(3-4):325–341, aug 2014.

[47] Boris Gurevich and Michael Schoenberg. Interface conditions for Biot's equations of poroelasticity. *The Journal of the Acoustical Society of America*, 105(5):2585, 1999.

[48] P. Cardiff, Ž. Tuković, H. Jasak, and A. Ivanković. A Block-Coupled Finite Volume Methodology for Linear Elasticity and Unstructured Meshes. *Computers and Structures*, (to appear), 2016.

[49] A.E. Kolesov, P.N. Vabishchevich, and M.V. Vasilyeva. Splitting schemes for poroelasticity and thermoelasticity problems. *Computers & Mathematics with Applications*, 67(12):2185–2198, 2014.

[50] Ž. Tuković. *Finite volume method on domains of varying shape*. PhD thesis, 2005.

[51] Ž. Tuković and H. Jasak. Simulation of free-rising bubble with soluble surfactant using moving mesh finite volume/area method. In *Proceedings of the 6th International Conference on CFD in Oil & Gas*, Metallurgical and Process Industries, Trondheim, Norway, 2008.

[52] Ž. Tuković and H. Jasak. A moving mesh finite volume interface tracking method for surface tension dominated interfacial fluid flow. *Computers & Fluids*, 55:70–84, 2012.

[53] Z. Tuković and H. Jasak. Simulation of thin liquid film flow using OpenFOAM finite area method. In *4th OpenFOAM Workshop*, Montreal, Canada, 2009.

[54] V. Škurić, P. De Jaeger, and H. Jasak. Lubricated contact model for cold metal rolling processes. In *Sedmi susret Hrvatskog društva za mehaniku*, Split, Croatia, 2016.

[55] M.G. Zielonka, K.H. Searles, J. Ning, and S.R. Buechler. Development and validation of fully-coupled hydraulic fracturing simulation capabilities. In *Proceedings of 2014 Simulia Community Conference*, Providence, Rhode Island, 2014.

[56] J. Réthoré, R. de Borst, and M.A. Abellan. A two-scale model for fluid flow in an unsaturated porous medium with cohesive cracks. *Computational Mechanics*, 42(2):227–238, 2008.

[57] G. Howard and C.R. Fast. Optimum Fluid Characteristics for Fracture Extension. *Drilling Production Practice*, 24:261–270, 1957.

[58] C.A.J. Blyton, D.P. Gala, and M.M. Sharma. A Comprehensive Study of Proppant Transport in a Hydraulic Fracture. In *SPE Annual Technical Conference and Exhibition*, Houston, Texas, 2015.

[59] E. V. Dontsov and A.P. Peirce. Slurry flow, gravitational settling and a proppant transport model for hydraulic fractures. *Journal of Fluid Mechanics*, 760:567–590, 2014.

[60] E. V. Dontsov and A.P. Peirce. Proppant transport in hydraulic fracturing: Crack tip screen-out in KGD and P3D models. *International Journal of Solids and Structures*, 63:206–218, 2015.

[61] T.J. Boone and A.R. Ingraffea. A numerical procedure for simulation of hydraulically-driven fracture propagation in poroelastic media. *International Journal for Numerical and Analytical Methods in Geomechanics*, 14(1):27–47, 1990.

[62] M.K. Fisher, C.A. Wright, B.M. Davidson, A.K. Goodwin, E.O. Fielder, W.S. Buckler, and N.P. Steinsberger. Integrating Fracture Mapping Technologies to Optimize Stimulations in the Barnett Shale. In *SPE Annual Technical Conference and Exhibition*, San Antonio, Texas, 2002.

[63] B. Ganis, V. Girault, M. Mear, G. Singh, and M. Wheeler. Modeling Fractures in a Poro-Elastic Medium. *Oil & Gas Science and Technology - Revue d'IFP Energies nouvelles*, 69(4):515–528, 2014.

[64] R.S Schechter. *Oil Well Stimulation*. Society of Petroleum Engineers, 1992.

[65] E. Detournay, A.H.D. Cheng, and J.D. McLennan. A Poroelastic PKN Hydraulic Fracture Model Based on an Explicit Moving Mesh Algorithm. *Journal of Energy Resources Technology*, 112(4):224, 1990.

[66] T.L. Bergman, F.P. Incropera, D.P. DeWitt, and A.S. Lavine. *Fundamentals of heat and mass transfer*. John Wiley & Sons, 2011.

[67] D.S. Dugdale. Yielding of steel sheets containing slits. *Journal of the Mechanics and Physics of Solids*, 8(2):100– 104, 1960.

[68] J.R. Rice. A Path Independent Integral and the Approximate Analysis of Strain Concentration by Notches and Cracks. *Journal of Applied Mechanics*, 35(2):379, 1968.

[69] D. Gross and T. Seelig. *Fracture mechanics: with an introduction to micromechanics*. Springer, 2011.

[70] W.K. Wilson and I. W. Yu. *The use of the J-integral in thermal stress crack problems. International Journal of Fracture*, 15(4):377–387, 1979.

[71] K. Sato and T. Hashida. Cohesive Crack Analysis of Toughness Increase Due to Confining Pressure. *Pure and Applied Geophysics*, 163(5-6):1059–1072, 2006. 90

[72] H. Yuan, G. Lin, and A. Cornec. Verification of a Cohesive Zone Model for Ductile *Fracture. Journal of Engineering Materials and* Technology, 118(2):192–200, 1996.

[73] B.F. Sørensen and T.K. Jacobsen. Determination of cohesive laws by the J integral approach. *Engineering Fracture Mechanics*, 70(14):1841–1858, 2003.

[74] T. Mura. *Micromechanics of defects in solids*. Springer Science & Business Media, 2013.